Compressive behaviors of modular steel shear-keyed grouped tubular columns

Kashan Khan[a,b,c,*], Zhihua Chen[a,b,c], Jiadi Liu[a,b,c], Khadija Javed[d,e], Konstantinos Daniel Tsavdaridis[f], Keerthan Poologanathan[g]

[a] *Department of Civil Engineering, Tianjin University, Tianjin, China*

[b] *State Key Laboratory of Hydraulic Engineering Simulation and Safety, Tianjin, China*

[c] *Key Laboratory of Coast Civil Structure and Safety, Tianjin University, Tianjin, China*

[d] *Guizhou University, Guiyang, China*

[e] *Kohsar University, Murree, Pakistan*

[f] *School of Science & Technology, Department of Engineering, City, University of London (UK)*

[g] *Department of Mechanical and Construction Engineering, Northumbria University (UK)*

Abstract: Modular steel structures (MSS) are distinguished from traditional steel structures (TSS) by the grouping and discontinuous features of columns, inter-modular connections (IMC), and other structural components. Vertical assembly requires shear-keyed grouped IMC to support modules' tubular columns, resulting in columns and IMC clusters that complicate force transfer. This study reported experimental, numerical, and analytical investigations on the compressive behaviors of steel shear-keyed grouped tubular columns. Four large-scale tubes with varied shear-key heights (L_t) and thicknesses (t_t) were subjected to axial compression testing. The test results demonstrated that raising L_t and t_t increased the buckling resistance of the tubes but lowered the ductility. The failure was caused by S-shaped local inward and outward buckling by neighboring columns located at shear keys, mid-height, or between 1/4 and 1/2 the tube's height. The finite element model (FEM) was generated to study the effects of 9 parameters using 147 models. The impact of tube spacing and numbers, varying shear-key length (d), width (b), L_t and t_t, tubes length (D), width (B), thickness (t_c), and height (L_c) on compression behaviors were observed. The results show that the nominal strength of neighboring tubes was reduced to achieve compression yielding and underwent local elastic buckling, making the EC3:1-1 Class 3 slenderness limit non-conservative. Prediction equations in EC3:1-1, CSA S16, AISC360-16, and GB50017 were used to evaluate the ultimate compressive resistance (P_u) of shear-keyed grouped tubes, but they overestimated results, proving non-conservative. To assess compressive behavior conservatively, modified prediction equations were proposed. Reliability analysis on 133 models showed that they accurately predicted the axial compression behavior of steel shear-keyed grouped tubular columns and can be used for MSS design.

Keywords: Axial compression tests; Steel shear-keyed grouped tubular columns; S-shaped local buckling; Finite element analysis; Modified code equations

***Corresponding author**:
Kashan Khan, E-mail address: Kashan@tju.edu.cn

Abbreviations

MSS/TSS, modular/traditional steel structures; IMC, inter-modular connections; SHS, steel-hollow sections; D, B, L_c, t_c, tubes' length, width, height, thickness; d, b, t_t, L_t, shear-key length, width, thickness, height; FEM/FEA, finite element model/analysis; E_s, elastic modulus; f_y, yield strength; f_u, ultimate strength; P_u, $P_{u,\ Test}$, $P_{u,\ FE}$, ultimate resistance via test, FEA; $P_{u,\ EC3}$, $P_{u,\ CSA}$, $P_{u,\ AISC}$, $P_{u,\ GB}$, ultimate resistance via EC3:1-1, CSA S16, AISC360-16, GB50017; K_e, $K_{e,\ FE}$, initial stiffness at 45% of axial load via experiment, FEA; Δ_u, $\Delta_{u,\ T}$, $\Delta_{u,\ FE}$, ultimate axial shortening via test, FEA; DI, DI_{FE}, ductility index via test, FE; Cov, coefficient of variation; LB, IB, OB, local, inward, outward buckling

Nomenclature

$\frac{\sigma_T}{\sigma_E}$= True/Engineering stress; $\frac{\varepsilon_T}{\varepsilon_E}$= True/Engineering strain; $\psi = \frac{\sigma_{min}}{\sigma_{max}}$, stress ratio; ρ_f/ρ_w, $Q/Q_s/Q_a$, and $\varepsilon = \sqrt{235/f_y}$, flange & web reduction, slender and non-slender columns reduction, and classification factor; L_{eff}, A_{eff}, d_e, and b_e, effective height, area, length, and width; χ, k_σ, K, and φ, capacity reduction, effective length, buckling, and partial safety factor GB50017; r, radius of gyration; f_e, elastic buckling stress; C_r, φ, λ, and L, ultimate resistance, resistance factor, strength ratio, unbraced length in CSA S16

1 Introduction

Modular steel structure (MSS) depends on the fabrication of fully-finished modular units in factories and their assembly on-site [1,2]. It is a globally recognized game-changing construction technology [3]. It has gained popularity due to its time and cost efficiency [3], superior quality [4], increased safety [5], and lower ecological effects [6]. The grouping, clustering, and discontinuous characteristics of structural members differentiate it from traditional steel structures (TSS), as seen in **Fig. 1** [7]. Compared to other materials, steel modules are renowned for their superior strength, ductility, lightweight, and ease of operation [8]. They are classified as continuous- or corner-supported based on the load-bearing components. Continuous-supported modules contain light steel supports at 300-600 mm designed primarily to resist gravity loads up to three stories in height [9]. Columns at corners of corner-supported modules withstand loads, inheriting a clear load transfer path and space flexibility, as shown in **Fig. 2(a)** [10–12]. Because they can extend to high-rise structures with an effective lateral stabilization system, they are often used in engineering projects, as depicted in **Fig. 2(b,c)** [3,13]. Corners use steel-hollow section (SHS) columns with superior compression, torsion, and bending resistance [14–16]. Therefore, the comprehensive study of SHS columns in corner-supported MSS will provide a reliable foundation for future MSS development.

As depicted in **Figs. 1 and 2**, MSS integrate discrete modules; thus, their mechanical behavior is determined by module structure and mutual damage behavior [17]. In contrast to TSS, MSS's integrity depends on a reliable inter-modular connection (IMC), which joins modules horizontally and vertically at corner columns, resulting in grouping and discontinuities [18]. Consequently, welded [19], bolted [18], and prestressed or post-tensioned [20,21] IMC are used to ensure structural integrity between SHS tubes. Robustness, instability, and IMC's difficulties in internal module connectivity are critical for MSS safety and quality [22,23]. Since weak IMC results in isolated columns, recent review studies detail a range of IMC, especially between SHS columns, that overcome technical obstacles [2,18,24,25–30].

Shear-key IMC, such as threaded-shaped, solid or hollow box-shaped, cruciform-shaped, and socket-shaped, are extensively used to connect columns, as shown in **Fig. 3(a-c)** [24]. **Figure 2(c)** displays the authors' 5-story Haoshi office MSS project using corner-supported modules assembled by shear-keyed grouped tubular columns, validating their application in engineering projects. Several studies on shear-keyed tubes and IMC has been recently carried out, such as Chen et al. [31,32] revealed their excellent seismic capacity, while the columns showed tearing. Exclusive studies on shear-key IMC by Hajimohammadi et al. [33] discovered that increasing the loading angle reduces shear-key ultimate capacity, rendering ISO/TR-16224, ASME-B1.1, and BS-3580 standards inapplicable. Besides, Khan et al. [34–36], Bowron [37], and Pang et al. [38] noticed their semi-rigid response while providing horizontal connectivity and shear resistance. However, they also witnessed the generation of high stresses on columns near shear-key zones. Dai et al. [39,40] found grouted shear-keyed IMC to be a rigid contributor to load resistance. Zhang et al. [41] and Deng et al. [42] proposed welded, and Ma et al. [43] developed bolted shear-key IMC. They observed shear key enables horizontal connectivity and shear resistance, but the lack of IMC welding caused rotations. Nadeem et al. [44] devised a self-locking IMC. They noticed excellent slipping and lateral force resistance [33]. However, they neglected the effects of initial geometric imperfections, rendering the design technique impractical. Additionally, Chen et al. [45] revealed that the shear key transmits shear force until yielding or substantial deformation. Moreover, stiffness and capacity rise with modest increases in the shear-key length and thickness, highlighting shear-keyed tubular columns' role in influencing MSS's structural behavior.

Modular steel structures have recently introduced pre- and post-tensioned shear-keyed grouped tube columns IMC. Chen et al. [20] and Liew et al. [46,47] discovered that they transfer lateral forces adequately. Sanches et al. [48,49] found that their lateral force resistance depends on mutual friction, and shear-key thickness is the governing factor. Lacey et al. [50,51] witnessed that sandblasting or expanding the tube-key contact area improves shear-slip resistance. Most IMC used shear keys without welding in tubes; however, research concentrated on the lateral behavior of shear-keyed columns. Tube and shear-key thickness were studied for shear and lateral force resistance; shear-keyed grouped tubular columns' axial compression behavior is undetermined. It is presumed that shear keys are firmly welded to tubes, which is impossible to accomplish due to inaccessibility inside grouped tubes. This results in an imprecise and insufficiently conservative design. Besides, these researches did not address geometrical imperfections affecting assembly and force transmission. As shown in **Figs. 2 and 3**, compression testing on non-welded shear-keyed grouped tubes is essential since they are used in MSS engineering projects.

MSS supported by shear-keyed SHS columns boosts structural performance [2,52]. Noticeably, the compression behavior of various SHS columns has been extensively researched in TSS. For example, Theofanous and Gardner [53] found that the EC3 effective width equation and Class 3 slenderness limit for stub and long stainless steel SHS columns are conservative. Kamran and Min [54] witnessed AISC360-16, CSA S16-19, and AISI S100-16 to be safe for SHS/RHS cold-formed stub columns. Liu et al. [55] discovered that Class 1~4 slenderness limits in EC-3 and ANSI/ AISC 360-16 for Q355 and Q460 mild steel columns are non-conservative. Rahnavard et al. [56]

noticed the non-conservativeness of the direct strength method in cold-formed boxes. Liu and Young [57] and Yan et al. [58,59] researched stainless steel columns' axial response at varying temperatures. Huang et al. [60] reported EC3, AISC360, and GB50017 as conservative for stainless steel. Contrary, Li et al. [61] and Wang et al. [62] discovered unsafe capacity and conservative classification outcomes for high-strength steel (HSS) tubes. Liu et al. [63] observed that reducing *D/t* increased capacity. Guo et al. [64] and key et al. [65] detected local buckling in stubs and long tubes. Deng et al. [66] explored an MSS tubular column with liftable IMC, finding that increasing column strength and thickness improves, but increasing height impairs ultimate resistance. Studies on tubular columns in TSS or MSS primarily focused on individual columns with or without IMC; group columns and neighboring column effects were lacking. Moreover, the outcomes were limited to hollow columns; shear-keyed tubes were not explored. Furthermore, the boundary conditions were assumed to be conventionally fixed, or welded tube ends with IMC, necessitating grouped column investigations to examine non-welded shear-keyed grouped tubes in MSS. Additionally, Khan et al.[14–16] found that existing standards overestimate the compressive strength of the tubular wall because MSS characteristics are disregarded. Long or stub mild, stainless, cold-formed, hot-rolled, and HSS tubes were investigated in TSS at ambient, low, or elevated temperatures. Their predictions and findings were limited to a single TSS tube, as resistance estimation assumed tube continuity at both ends. MSS's integrated modules group columns in the IMC zone, causing discontinuity and rotation on each floor [67]. Limited information on non-welded shear-keyed grouped tubular columns of different effective lengths, critical loads, and ultimate resistances leads to imprecise design. Conventional design criteria for shear-keyed grouped tubular columns become questionable if special features and connections are not incorporated. Besides, tube designs that disregard shear keys are unsuited for shear-keyed column design. This emphasizes the necessity for axial compression tests and an analysis of the conservatism of existing steel standards on shear-keyed grouped tubular columns. Corner-supported modules connected at interior IMC have distinctive aspects; therefore, it is vital to investigate the axial compression behavior of shear-keyed grouped tubular columns considering their utilization in high-rise MSS globally [3,13].

This study investigated the compressive behaviors of steel shear-keyed grouped tubular columns by testing four large-scale tubes with varied L_t and t_t. The results of load displacement, deflection, and strain were presented. The accuracy of FEM was then verified using test data to explore the impact of 9 varying parameters. Finally, modified prediction equations for EC3:1-1, CSA S16, AISC360-16, and GB50017 were proposed to asses shear-keyed grouped columns P_u.

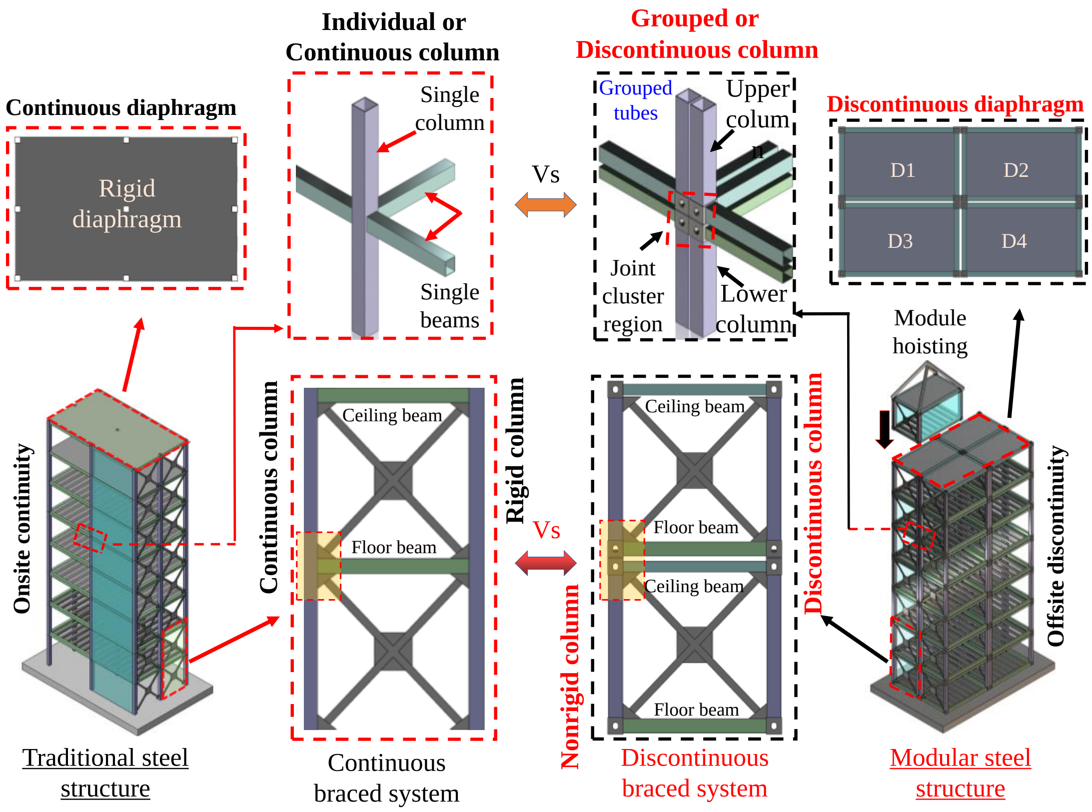

Fig. 1 Uniquenesses of MSS relative to TSS

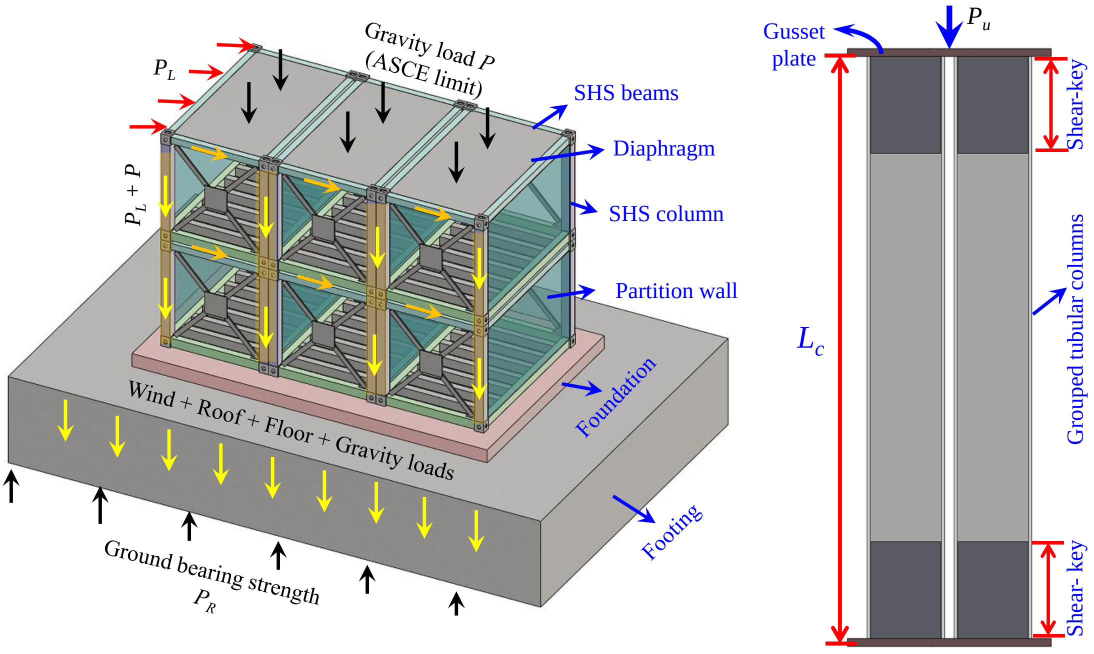

Force transmission of multi-story MSS Shear-keyed grouped tubes

(a) Shear-keyed grouped tubes force transfer

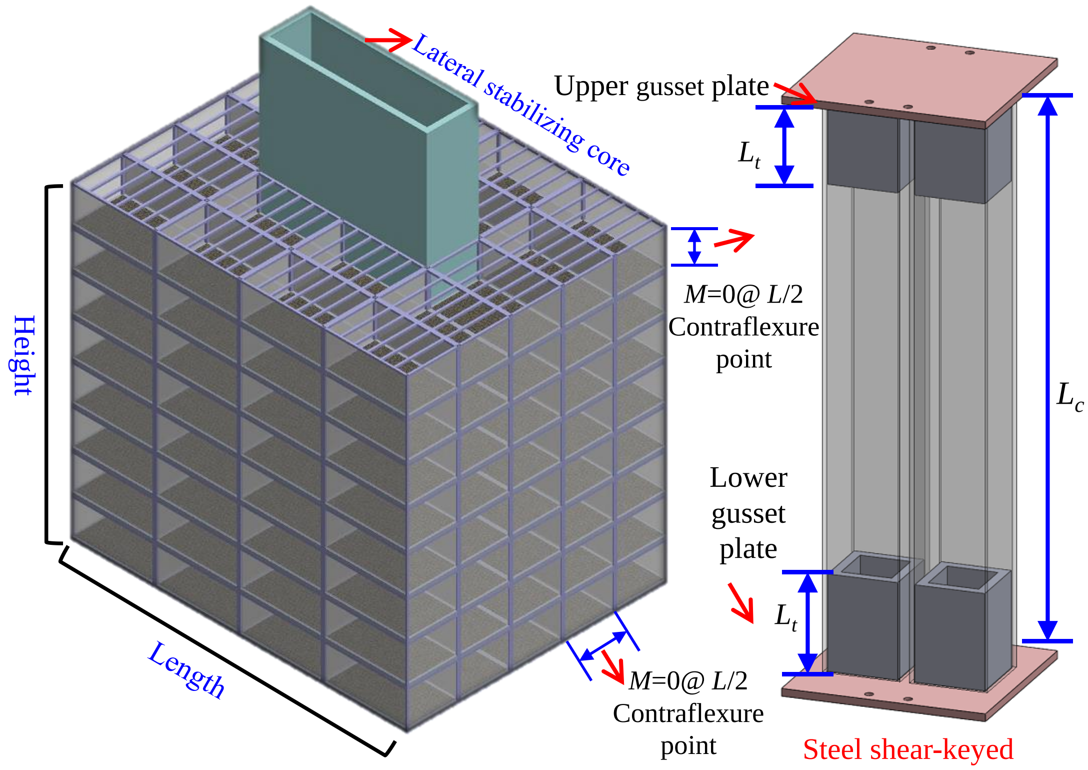

High-rise corner-supported MSS with concrete core Steel shear-keyed grouped tubular columns

(b) Multi-story MSS with steel shear-key IMC supporting grouped tubular columns

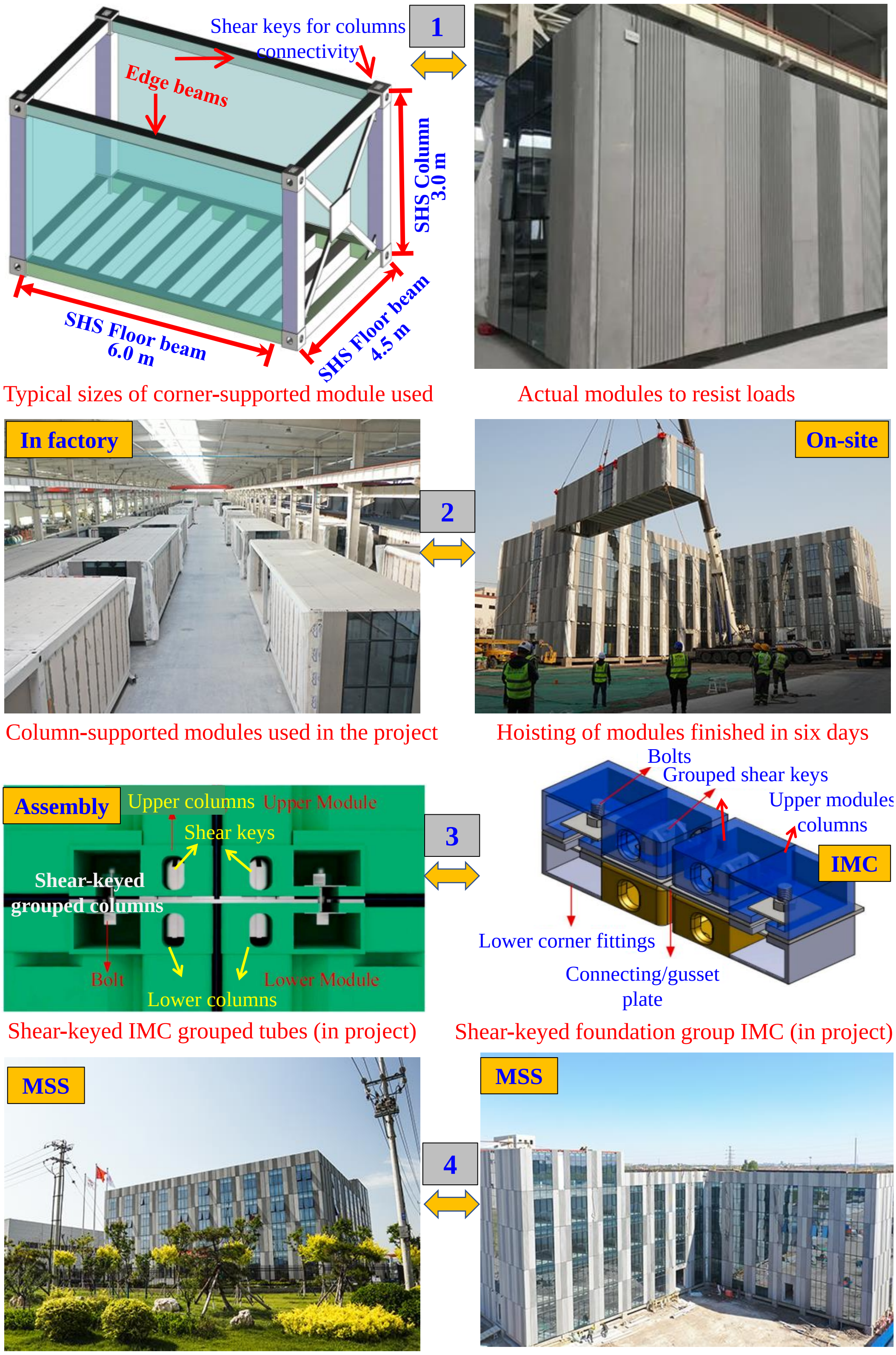

Haoshi office building, Tangshan Lutai Economic Development Zone completed in six days

(c) Corner-supported modules with shear-keyed grouped tubes in the MSS project in China (Designed by the research team) [68]

Fig. 2 Engineering background of shear-keyed grouped tubular columns and IMC in corner-supported MSS

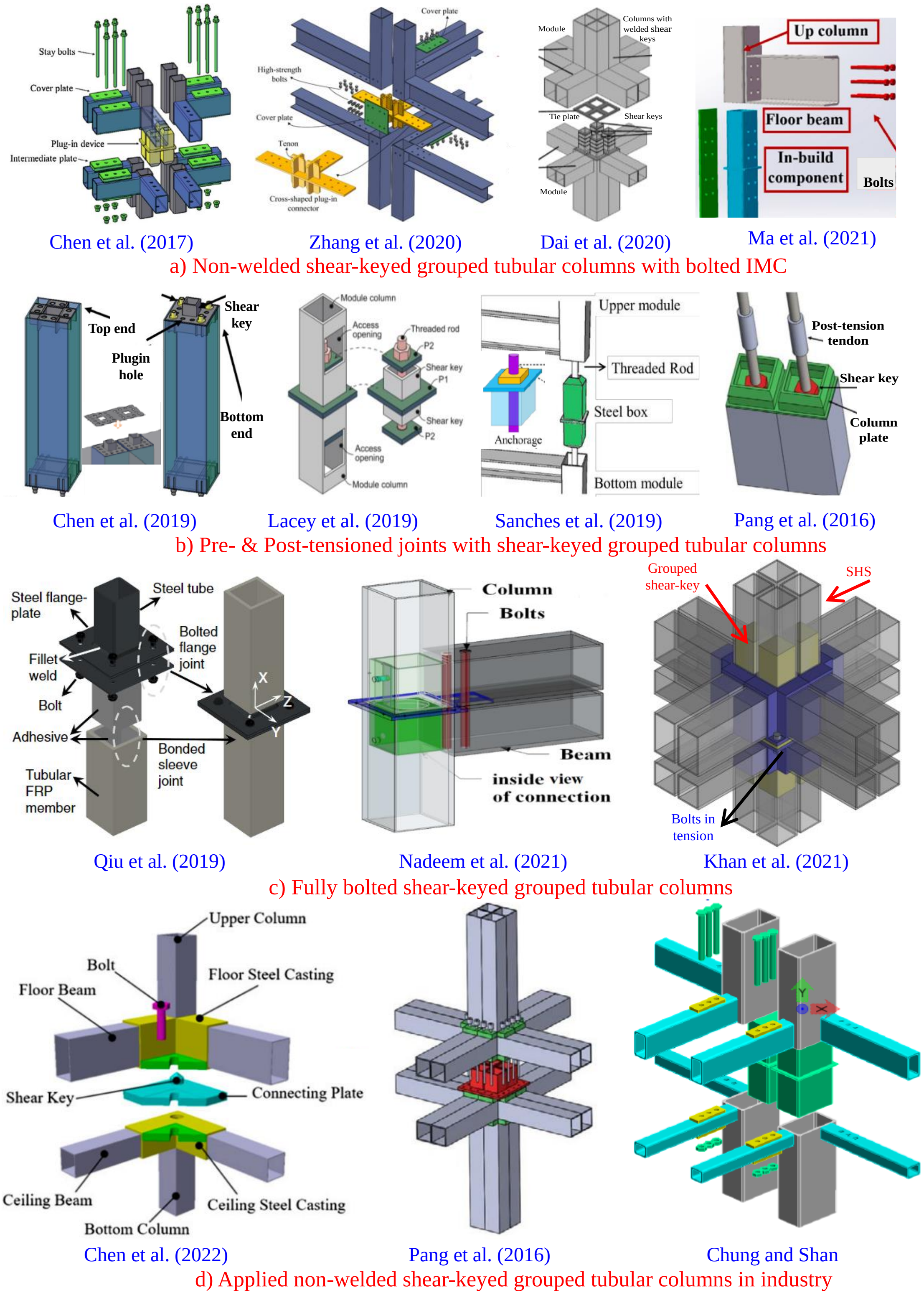

Fig. 3 Shear-keyed grouped columns and IMC in MSS

2 Axial compression tests of steel shear-keyed grouped tubular columns

2.1 Specimens design

The study used an engineering background of a five-story corner-supported MSS named Haoshi office building China, designed by the authors' research team in compliance with Chinese steel design code GB50017-2017 [69]. As indicated in **Fig. 2**, specimen cross-sections were formed based on the prototype project to maintain consistency. The primary purpose of the testing was to acquire experimental data and associated failure modes for initial geometric imperfection to validate FEM, followed by extensive parametric and analytical research. The average height of modules in an actual engineering project was 3 m. Following limitations of test facilities and studies on modular joint literature, the column subassembly method was used to design member length and height based on zero-moment inflection points. Thus, the current research adopted column height as half the actual height, as displayed in **Fig. 2(b)** [25]. This research employed a hollow, box-shaped, grouped shear-key welded to upper and lower connecting plates [24]. Following the actual project scenario, most IMC criteria and safer design, shear keys, and connecting plates were not welded to tubes to allow for rotation. Studies on non-welded shear-keyed tubes, IMCs, and frames indicated that shear keys must have shrunken or sloped ends with a 3 mm [31,70] to 6 mm [48,49] gap between the column and inserted shear keys in the initial state to facilitate alignment and allow installation error. Thus, the current study allows a 1 to 2 mm gap between the tube and shear key to account for the insertion of keys on both ends; otherwise, construction tolerances could hinder installation. Additionally, considering MEP's crossing and working accessibility in realistic situations, a 24 mm gap was allowed between neighboring columns, making the distance between grouped shear keys 44 mm.

2.2 Specimens geometry

One 1/2 large-scale welded and three shear-keyed grouped tubular column specimens are included in the testing program to evaluate compression and the interaction behavior between neighboring tubes and tubes and the shear keys, respectively. Specimens were designed per the MSS's prototype project, and the geometrical details used in testing are depicted in **Fig. 4**. Welded IMC is the most common type with satisfactory performance [19,71–73]; however, it is costly, and complete welding is impossible [74]. Shear-keyed IMCs perform well, fulfilling their role as a superior alternative to welded IMC [48,49]. Moreover, welded IMC connects tubes without any component inserted, making the tubes homogenous with flexural stiffnesses on ends and mid-height identical. However, shear-keyed tubes are non-homogeneous, with a hollow central part and two ends supported by shear keys of varying rigidities [75]. Thus, shear-keyed grouped tubes' were compared to welded ones to evaluate the difference in performance and failure caused by the employment of shear keys. The specimen FD1 was used as the standard to investigate the effect of shear-key and tube-plate welding on the compression behavior of grouped tubes. Therefore, shear keys were lacking on FD1, and the connection plate was partially welded directly to the ends of the SHS columns on three sides (top and bottom). Because the working space between adjacent tubes in grouped columns was insufficient for full welding, the fourth side of the tubes was not welded. Other specimens, namely FD2, FD3, and FD4, were designed to examine shear-key effectiveness; thus, different lengths (L_t) and thicknesses (t_t) of shear-key were considered. All specimens were prepared with 1.5 m column heights (L_c). The dimensions of the connecting plate for them matched those of the actual project connection gusset plate, which was 524 mm long, 490 mm wide, and 20 mm thick. Similarly, the identical SHS tube cross-section was used for all grouped column specimens with cross-sections of 200×200×8 mm. The goal of examining similar column sizes was to keep the design consistent while focusing on the influence of grouped shear-key contribution. Each column measured 200 mm long (D), 200 mm wide (B), and 8 mm thick (t_c). Furthermore, each shear-keyed grouped tubular column specimen (FD2, FD3, and FD4) had the same cross-section length (*d*) and breadth (*b*) of 180 mm, but they differed in terms of shear-key thickness (t_t) and height (L_t). To assess the presence and insertion height of shear-keys, specimen FD3 grouped shear-key t_t was set to 10 mm and L_t to 150 mm, and the findings were compared to those of FD1. Conversely, FD2 and FD4 were designed to observe the contribution of grouped shear-key height. Hence, the shear-key thickness was kept constant, such as t_t of 25 mm, with L_t ranging from 100 to 250 mm. **Figure 4** and **Table 1** contain more information on each specimen.

Table 1 Details of shear-keyed grouped tubes for axial compression

Sp. #	D (mm)	B (mm)	t_c (mm)	t_t (mm)	d (mm)	b (mm)	L_t (mm)	E_S (GPa)	f_y (MPa)	f_u (MPa)	Grade	P_u (kN)	K_e (kN/mm)	Δ_u (mm)	DI Ratio
FD1	200	200	8	-	-	-	-	206	380	434	235	4214	1174	10.2	1.6
FD2	200	200	8	25	180	180	250	206	380	434	235	4169	1025	9.4	1.9
FD3	200	200	8	10	180	180	150	206	380	434	235	4119	1358	8.7	2.2
FD4	200	200	8	25	180	180	100	206	380	434	235	4176	1084	7.7	1.8

Sp. #	D (mm)	B (mm)	t_c (mm)	t_t (mm)	d (mm)	b (mm)	L_t (mm)	$P_{u,FE}$ (kN)	$\frac{P_u}{P_{u,FE}}$	$K_{e,FE}$ (kN/mm)	$\frac{K_e}{K_{e,FE}}$	$\Delta_{u,FE}$ (mm)	$\frac{\Delta_u}{\Delta_{u,FE}}$	DI_{FE} (Ratio)	$\frac{DI}{DI_{FE}}$
FD1	200	200	8	-	-	-	-	4102	1.03	1429	0.82	8.2	1.25	2.6	0.64
FD2	200	200	8	25	180	180	250	4135	1.01	1290	0.79	7.3	1.28	2.1	0.88
FD3	200	200	8	10	180	180	150	4071	1.01	1528	0.89	7.2	1.20	2.2	1.01
FD4	200	200	8	25	180	180	100	4071	1.03	1340	0.81	9.6	0.80	2.1	0.83
Mean									1.02		0.83		1.13		0.84
Cov									0.01		0.05		0.17		0.16

Sp. #	D (mm)	B (mm)	t_c (mm)	L_c (m)	EC3 Class	$P_{u,EC3}$ (kN)	CSA Class	$P_{u,CSA}$ (kN)	AISC Class	$P_{u,AISC}$ (kN)	GB Class	$P_{u,GB}$ (kN)	Grade	P_u (kN)	Δ_u (mm)
FD33	200	200	8	1.0	C1	4669	C2	4174	NS	4610	B	4577	235	3759	12.2
FD114-1	200	200	8	1.5	C1	2303	C2	2059	NS	2269	B	2231	235	1804	7.6
FD115-2	200	200	8	1.5	C1	4606	C2	4118	NS	4538	B	4462	235	3849	11.0
FD116-3	200	200	8	1.5	C1	6908	C2	6178	NS	6807	B	6693	235	6057	7.2
FD117-4	200	200	8	1.5	C1	9211	C2	8237	NS	9075	B	8924	235	7978	7.9
FD35	200	200	8	2.0	C1	4510	C2	4025	NS	4438	B	4330	235	3733	13.2
FD36	200	200	8	3.6	C1	4105	C2	3481	NS	3960	B	3810	235	3922	12.5
FD52	200	200	9	1.5	C1	5153	C2	4118	NS	5077	B	4992	235	4252	14.4
FD49	200	200	5	1.5	C4	1506	C4	1345	S	2268	B	2836	235	1377	19.3
FD50	200	200	7	1.5	C2	4052	C3	3624	NS	3992	B	3926	235	2969	11.6
FD61	150	150	8	1.5	C1	3331	C1	2973	NS	3278	C	3055	235	3630	9.2
FD62	180	180	8	1.5	C1	4097	C2	7329	NS	4037	B	3957	235	3782	10.0
FD63	250	250	8	1.5	C3	5876	C3	5239	NS	5780	B	5721	235	3994	11.0

D, *B*, L_c, and t_c define the columns' length, width, height, and thickness; *d*, *b*, t_t, and L_t denote shear keys' length, width, thickness, and height; E_s, f_y, f_u, P_u, $P_{u,FE}$, $P_{u,EC3}$, $P_{u,CSA}$, $P_{u,AISC}$, $P_{u,GB}$, K_e, $K_{e,FE}$, Δ_u, $\Delta_{u,FE}$, DI, DI_{FE}, and Cov define elastic modulus, yield strength, ultimate strengths, ultimate resistance via experiment, FE, EC3:1-1, CSA S16, AISC360-16, and GB50017, initial stiffness via experiment, FE, axial shortening via experiment, FE, ductility index via test, FE, and coefficient of variation, respectively.

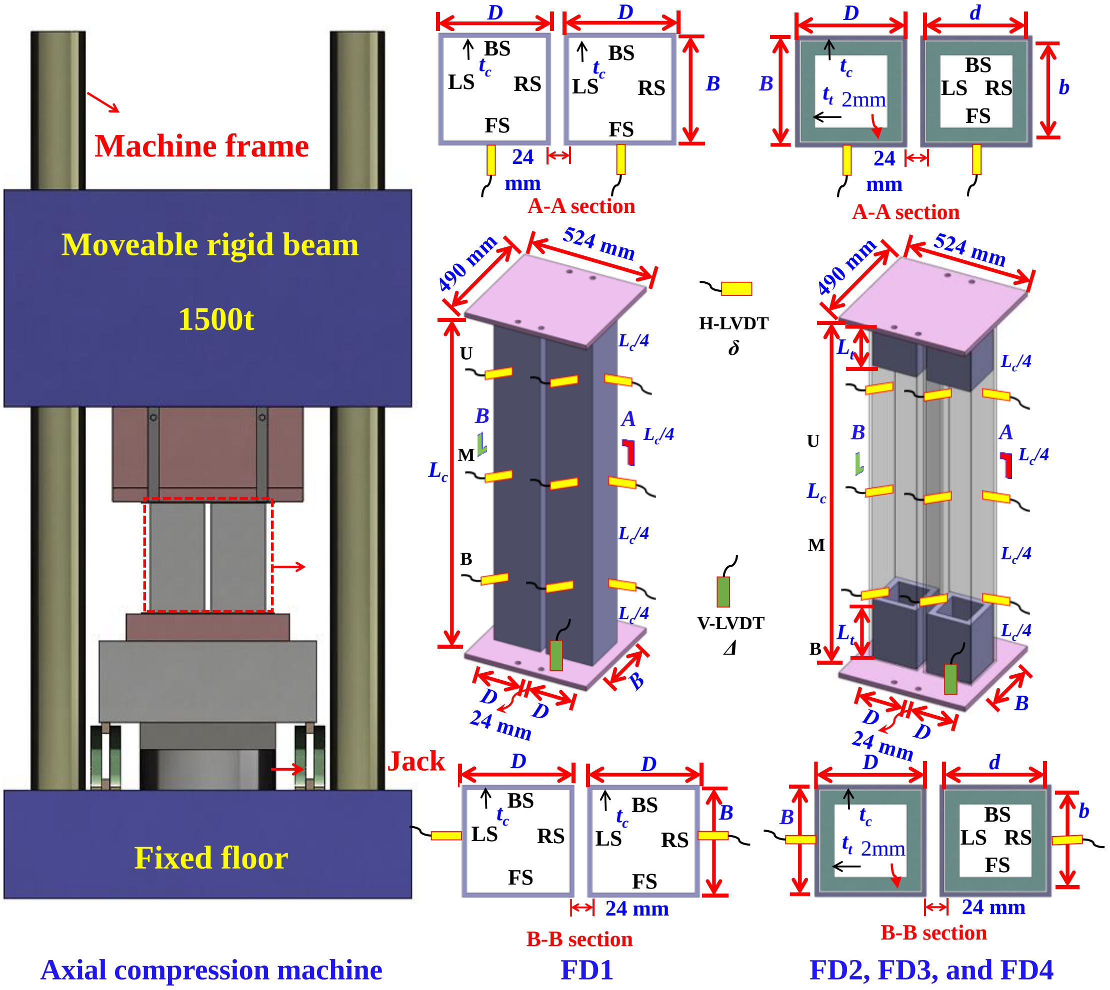

(a) Test and LVDTs details of shear-keyed grouped tube columns

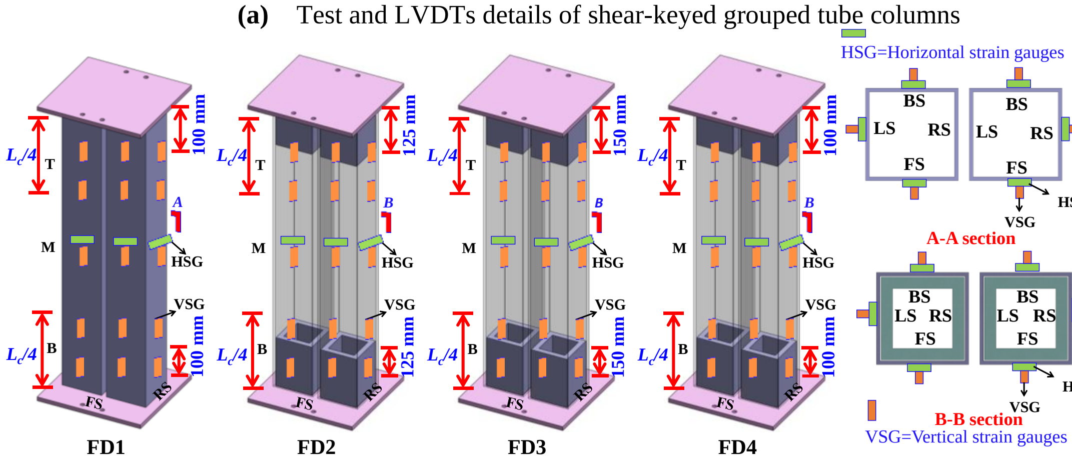

(b) Positions of vertical & horizontal strain gauges

Fig. 4 Axial compression tests design of shear-keyed grouped tubular columns

2.3 Material properties

Because the specimens were made of mild steel, their mechanical properties may impact their performance. Therefore, the steel coupons were designed following the GB/T228.1-2010 specification [76]. **Figure 5(a)** depicts their dimensions. Steel coupons fabricated from the same material as the shear-keyed grouped tubular column were used to assess test findings and generate FEM. Although the cross-section and thickness of the test columns were similar, three coupons were made due to the constructional tolerance effect. **Table 1** shows the average of the obtained parameters. The test setup for steel coupons is shown in **Fig. 5(a)**. Furthermore, **Fig. 5(b,c)** depicts steel coupon failure modes and tensile stress-strain curves. This shows that geometric imperfection considerably affects the strength and ductility of mild steel, whereas failure modes and initial stiffness are unaffected.

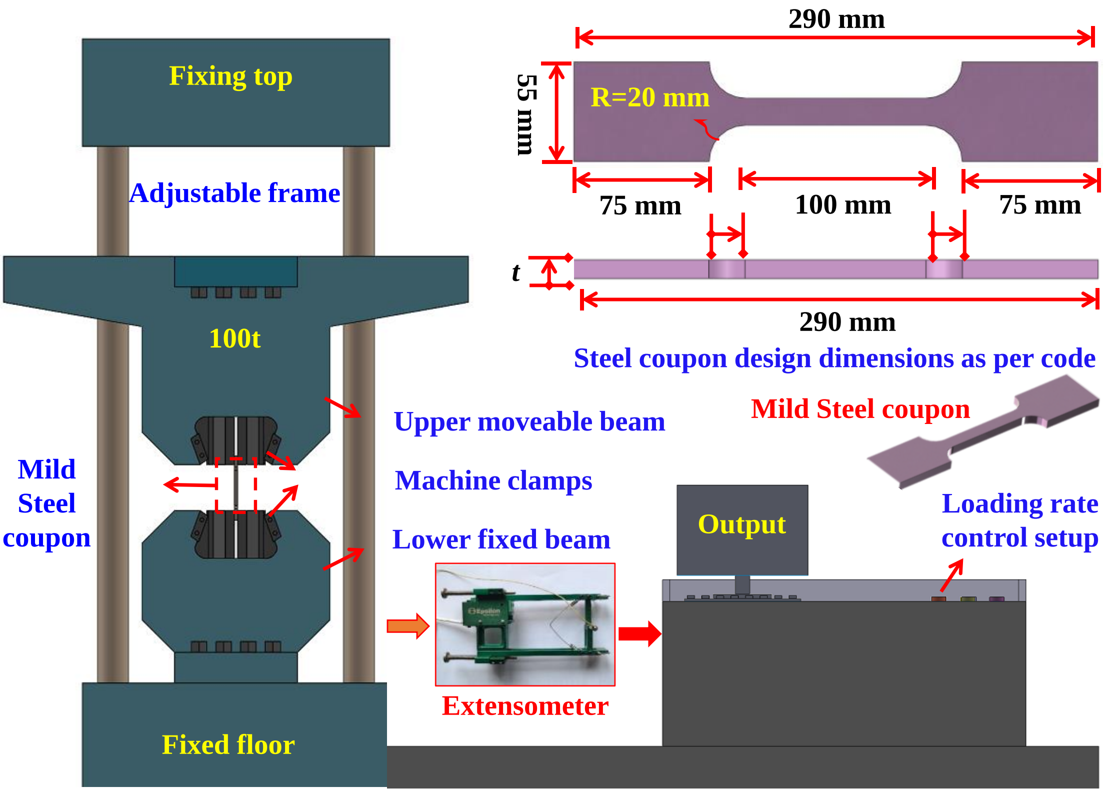

Material testing machine at Tianjin University, China

(a) Details of steel coupons test setup

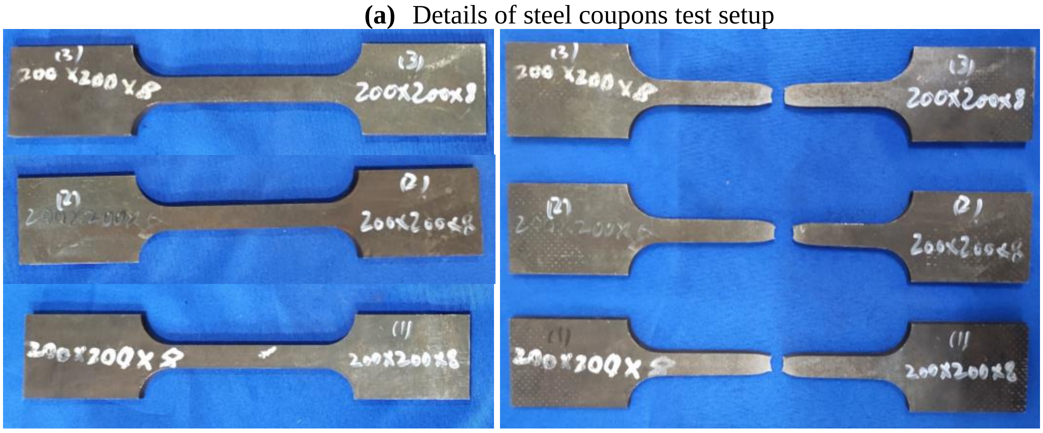

Steel coupon before test initiation

Steel coupon after failure

(b) Steel coupons behavior

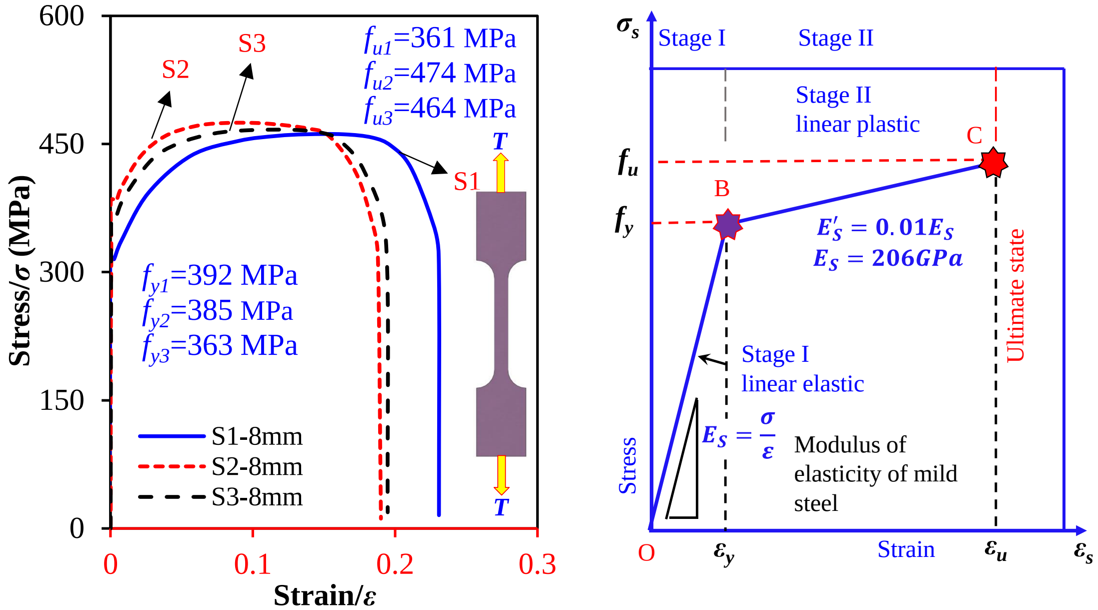

Engineering stress-strain curves **True stress-strain curve**

(c) Test stress-strain curves and FE material model

Fig. 5 Material testing and representative stress-strain curves

2.4 Test setup of shear-keyed tubes

Figures 4(a) and 6(a,b) depict a schematic and real-time view of compression tests conducted on a 1500t axial compression testing machine (CTM) at Tianjin University's structural engineering laboratory. Specimens manufactured in the yard were transported by truck and installed on the testing machine using a crane in their allotted locations between tightly supported machine beams. The CTM's upper beam could be adjusted, while the lower beam could only be used to exert pressure via the jack. Steel bolts were inserted and screwed into the connecting plates after the specimens were installed. Bolts were employed to avoid any out-of-plane instability produced by specimen movement when the grouped tubes rotate about shear-key, and the specimen lacks restraints. According to GB/T50344-2019 [77], loading was divided into preloading and formal loading, with unloading occurring in both. The load-end shortening curves were generated automatically since the 1500t CTM used a hydraulic jack to apply pressure to the shear-keyed grouped columns' bottom. However, because CTM records end-shortening with the movement of the rigid bottom beam, the accuracy of curves can be affected as specimen location on the machine is adjusted. The connection mechanism and measuring instrument precision was validated by applying a preload of $0.2P_u$. Specimens were held for two minutes after reaching preload before being completely unloaded for two minutes. Following a monotonic vertical force loading until yielding, a 0.5 mm/min progressive displacement loading was applied until peak strength (fall to 85% of P_u) was attained. The yield point and criteria for managing displacement loading were considered at the end of the linear elastic area of load-end shortening curves and the beginning of the nonlinear portion. The load cell installed in the machine was used to measure reaction forces, which were then shown as an output data file.

Strain gauges on specimens examine structural deformation and stress fluctuation over time, as seen in **Fig. 6(a,b)** [78]. The stress rise measured by strain gauges revealed the force transfer mechanisms during the load application. After altering the shear-key parameters, several strain gauges were installed to measure stress development during the test. Strain gauges were positioned in areas with the most significant deformation compared to other sites using pre-test FEM stress prediction. During the testing, strain gauge data was collected to assess local buckling and yielding strain [79]. Local buckling can be outward or inward; a strain gauge reveals whether it occurred before or after yielding to investigate elastic or plastic buckling. Each specimen was fitted with a significant number of strain gauges to ensure that at least one strain gauge was situated in possible buckling zones. If not, the strain history of other strain gauges must be monitored regularly for irregularities or nonlinear reactions. Strain gauges were mounted circumferentially on column portions with and without shear keys to examine relative stress and deformation patterns. Because the columns were susceptible to in- and out-of-plane local buckling, strain gauges were attached to the front, right, and back of the right and the front, left, and back of the adjacent left column. Due to a lack of available workspace, the inner sidewalls, right side of left column, and left side of right column lacked strain gauges. In the vertical direction, strain gauges were evenly distributed on tubes about a quarter of the distance from the upper, central, and lower positions. In the horizontal direction, strain gauges were attached at mid-height. For FD1, which lacked a shear key, strain gauges were mounted at 100-150 mm similar to those on the edges of FD3 since it was expected that the stresses would be compared when investigating the shear-key effect. For FD2 and FD4, strain gauges were circumferentially positioned to the tube's edges based on shear-key height, such as 125 mm for FD2 and 100 mm for FD4, to analyze stress fluctuation between regions with and without shear keys. There were thirty-two strain gauges installed on the FD1, FD2, FD3 and FD4. **Figure 4(b)** depicts the location and distances of these strain gauges.

To measure the amount of deflection or the global buckling of both tubes, horizontal linear variable differential transducers (LVDT) were positioned vertically on the neighboring tubes on both adjacent sides at the tubes' mid, top, and bottom quarter heights. Additionally, it was intended to measure the length shortening of grouped tube specimens; therefore, a vertical LVDT was installed on the machine, as shown in **Figs. 4(a) and 6**. The load offered by CTM and the vertical displacement provided by LVDT were used to create the end-shortening curves. A data recorder was employed to capture the deflections, reaction forces, shortening, and strains.

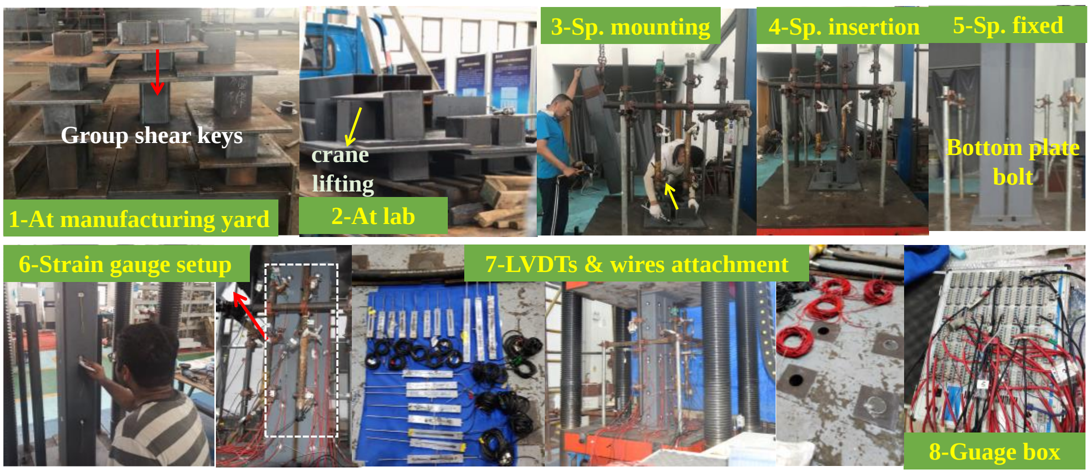

a) Test arrangements and setup

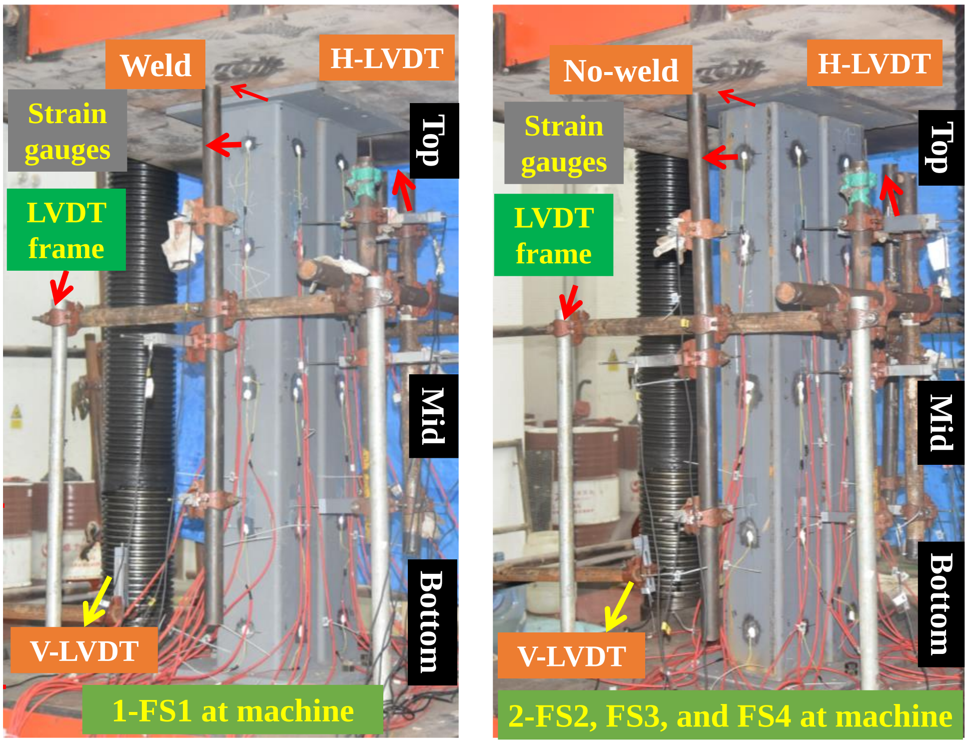

b) Test setup of shear-keyed tube specimens

Fig. 6 Axial compression test setup of shear-keyed grouped tubes in MSS

3 Experiment outcomes

3.1 Specimens failure modes

Figure 7(a) shows FD1 welded grouped column failures. It shows that both neighboring tubes displayed outstanding buckling resistance and rigid connection that prevented global buckling. After severe local buckling, a tube at mid-height showed in-plane buckling, possibly due to the adjacent column effect. Both tubes' main failure modes were symmetrical in shape and position, such as local inward and outward buckling at 100 mm at the opposite loading side, as validated by higher strain values at the quarter length. Each side exhibited only one form of local buckling, and the opposing sides showed the same failure pattern. Contrary, neighboring faces showed the reverse trend. Both tubes' front and back sides bulged out, followed by the neighboring tubes' interior and exterior sides' inward buckling, preventing adjacent columns from colliding. No other locations showed buckling, and all yielded before ultimate strength, indicating local plastic buckling.

Figure 7(b) depicts failure modes of FD2 shear-keyed grouped tubes, revealing that the tubes exhibited slight in-plane bending after substantial local buckling caused by rotation around shear keys due to nonrigid constraints. The tubes' principal failure modes were symmetrical but positioned differently. They displayed local-inward and outward S-shaped buckling on each side from shear-key mid-height, 125 mm, to 1/4 of the tube's height, 375 mm, on the opposite loading end. Failure on opposite sides was identical; however, dissimilar on the tubes' neighboring faces but more apparent on one side than the other. This was consistent with the different strains on opposing faces. Both columns buckled symmetrically; thus, bulged regions on the interior sides showed contact. However, the buckling of one column adjusts the other column's location, avoiding collision and resulting in double S-shaped buckling. Columns capacity is unaffected because severe local buckling does not contribute to load resistance. Some shear key sections did not yield, demonstrating a stress concentration that caused elastic buckling. On average, shear keys reported higher stress values, implying tube shearing.
Figure 7(c) shows the FD3 shear-keyed grouped tube failure scenario, demonstrating that one tube experienced in-plane global buckling while the other did not. In both tubes, no out-of-plane global buckling was noticed. The tubes' principal failure was caused by inward and outward buckling at upper and lower shear-key sites. One tube displayed two opposing trends of local bucklings, such as bulging out of the front at 150 mm with bulging in at 500 mm and bulging in of the side at 150 mm, followed by bulging out at 500 mm. Another tube showed local inward and outward S-shaped buckling, identical on opposing sides and opposite on adjoining sides. A tube's global and asymmetric local buckling prevented adjacent columns from colliding. The behavior was non-uniform, resulting in failure modes near shear-key edges and between 1/4 and 1/2 of the tube height. Load-strain curves revealed most regions yielding or elastic buckling.

The failure modes of FD4 shear-keyed grouped tubes are depicted in **Fig. 7(d)**, which shows no evidence of in- or out-of-plane global buckling. A modest increase in shear-key thickness and length displayed uniform force transfer and shear-key yielding, as reflected by comparable strain. The primary failure modes were symmetrical but slightly differed in position, which was consistent with FD2. They generally displayed a pair of local-inward and outward S-shaped buckling on each side starting from the shear-key edge, i.e., 150-200 mm. Failure was identical on opposite sides yet opposite on adjacent faces. Besides, both columns bulged out on the interior sides, preventing collisions, and resulting in double S-shaped buckling. Shear key regions resulted in larger stress, indicating the shearing effect or elastic buckling. Furthermore, decreasing the shear-key length reduced tube capacity, confirming the shear-key significance.

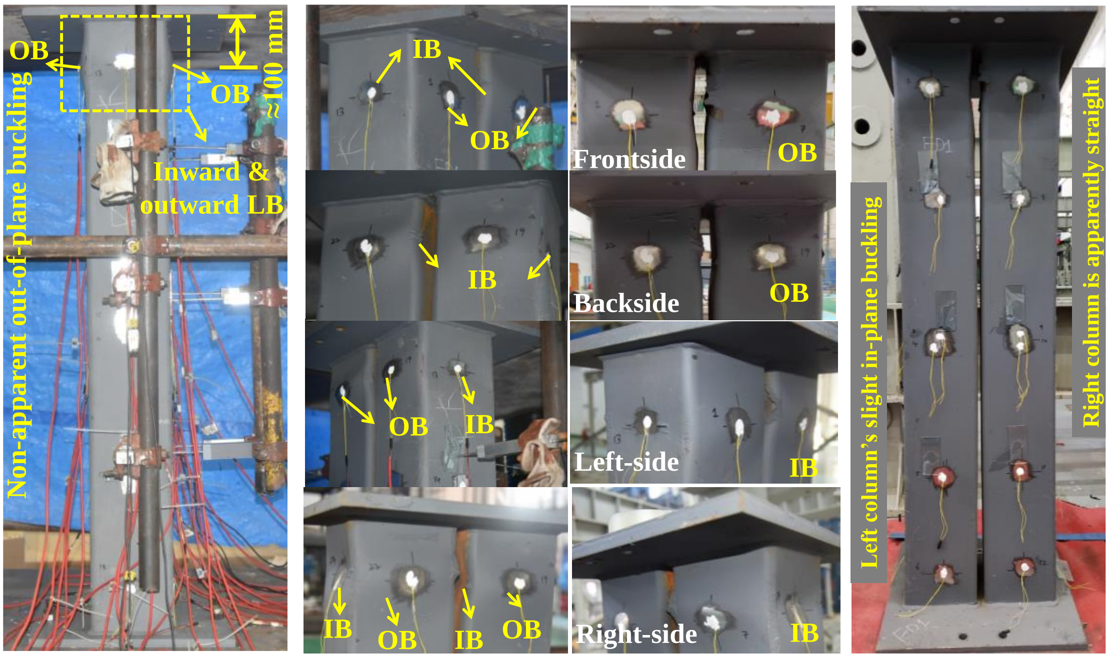

a) FD1 specimen

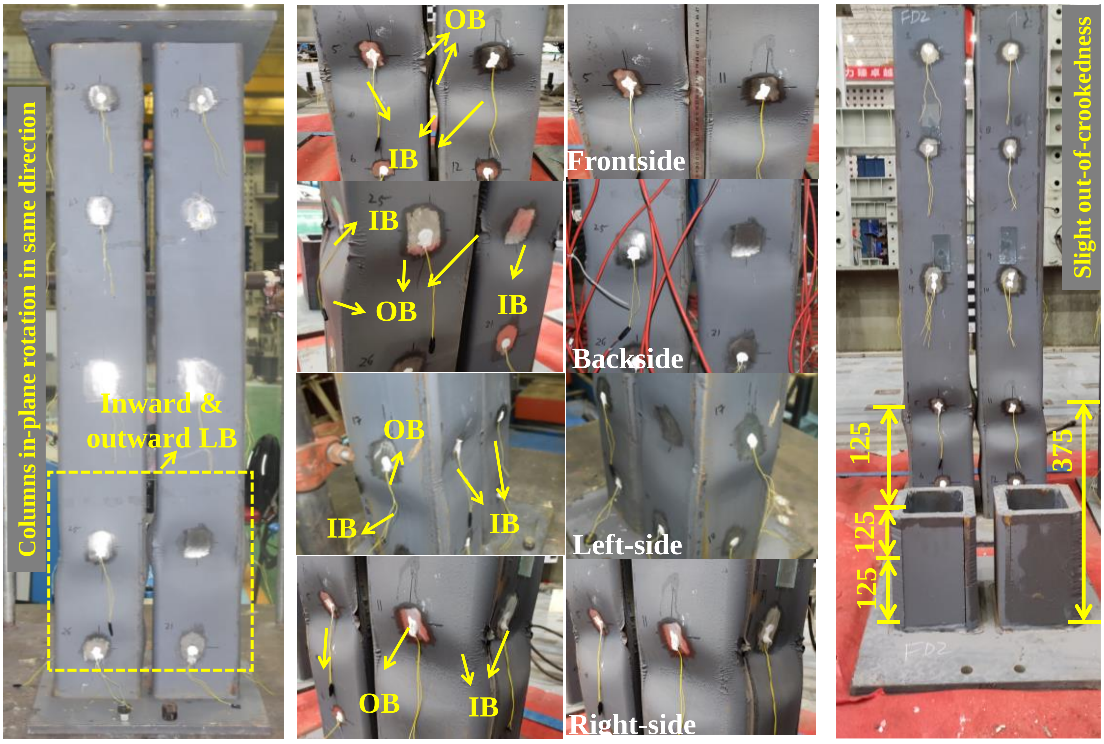

b) FD2 specimen

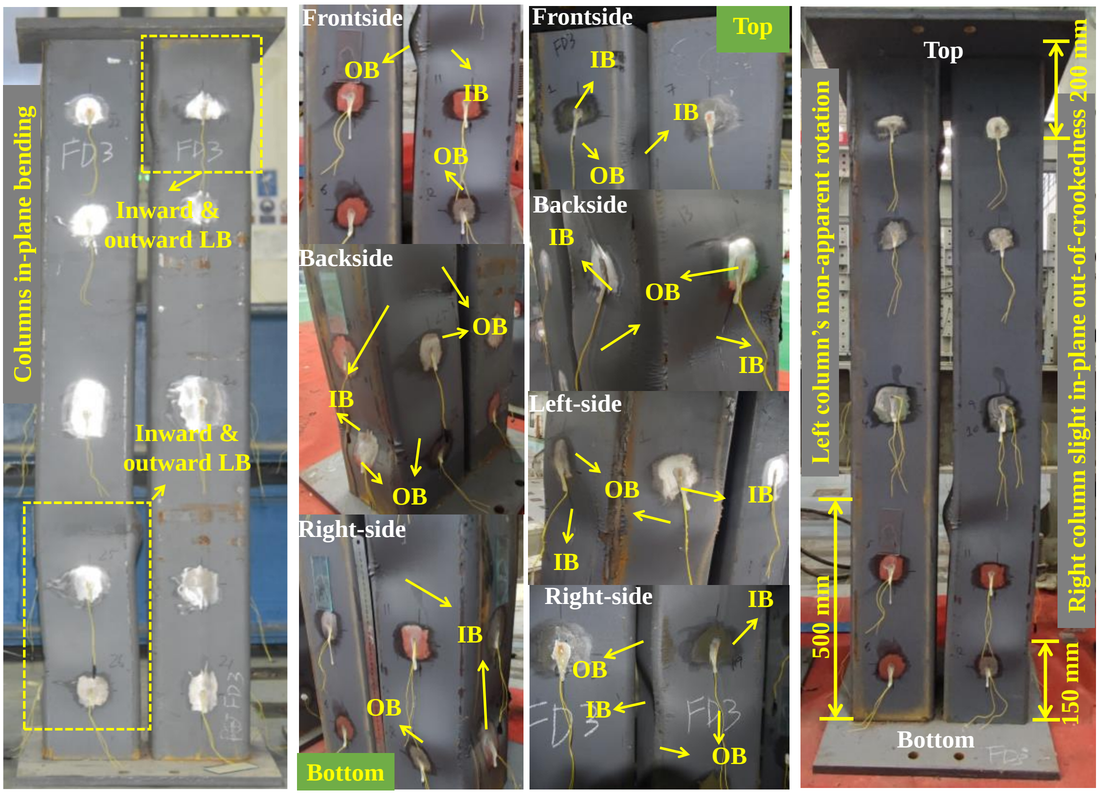

c) FD3 specimen

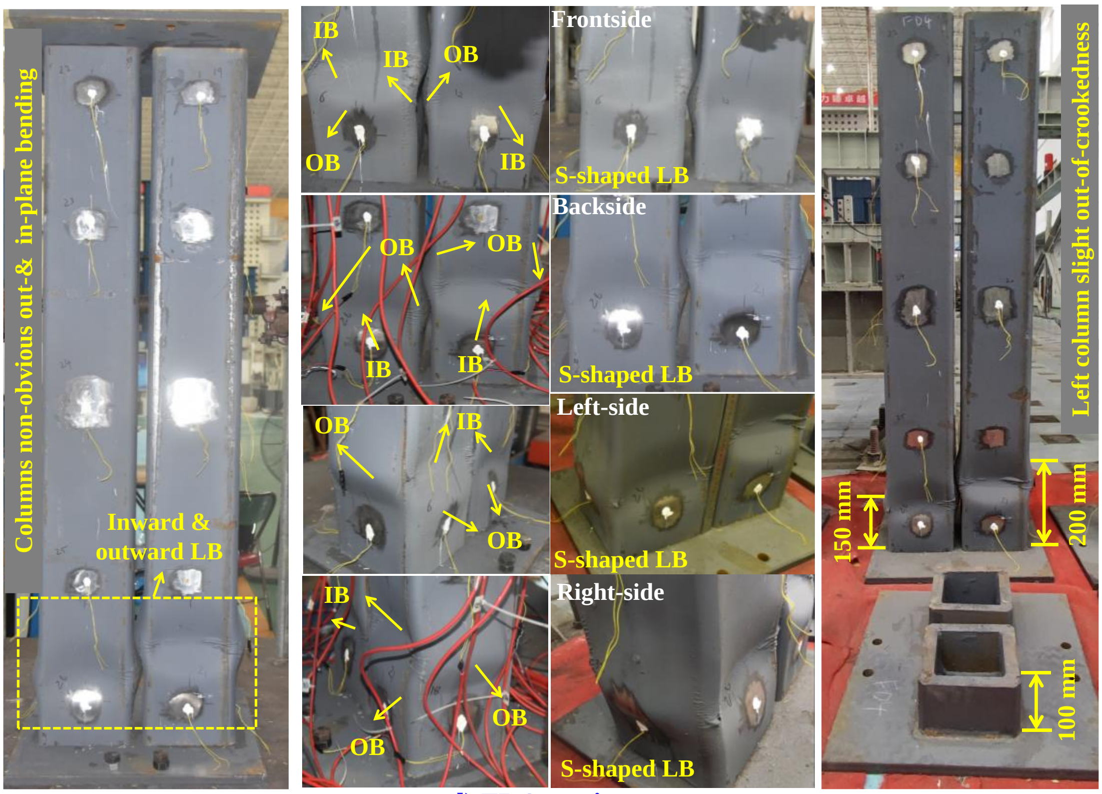

d) FD4 specimen

Fig. 7 Failure modes of shear-keyed grouped columns under axial compression (LB, local buckling; IB, inward buckling; OB, outward buckling; S-shaped, sinusoidal-shaped)

3.2 Load-shortening curves of shear-keyed grouped tubes

Figure 8(a-d) illustrates the shortening behavior of the specimens. **Figure 8(e)** depicts the generalized curves indicating that both type A and type B curves possess a linear elastic (I), a nonlinear (II), and a recession (III) zone. To group specimens, the starting point of the nonlinear branch (elastic) and the length of the second (nonlinear) and third (recession) stages of the *P*-*Δ* curves are considered. FD1, FD2, and FD3 are categorized as type A, whereas FD4 is classified as type B. The term *P* indicates the load, and the *Δ* defines shortening. These figures demonstrate that *P* grows linearly during the linear elastic stage until the yield stage P_y is achieved. It reveals that the length of the elastic state was shorter in specimens of type B, resulting in earlier yielding than in type A. This may be due to the shear-keyed tubes' decreased buckling strength because of the shortest height, which limits the specimen's elastic zone and causes it to yield early due to the weak combined action of the tubes and shear keys. After P_y, the *P*-*Δ* curves reveal a parabolic shape until they reach their ultimate loads P_u; concurrently, local buckling commences when the specimen achieves its compression capacity. After the nonlinear phase (stage II) for both curves, columns at various locations exhibit local elastic or plastic buckling. Local buckling begins in one tube, followed by symmetrical or asymmetrical initiation in neighboring tubes. However, neighboring tube buckling and surface contact do not affect the ultimate strength development. Contrary to their elastic state, type B curves have greater ultimate strength than type A curves. This favorable result may be attributable to the shear keys' moderate cross-section, which increased its strength by postponed buckling until complete yielding to fully utilize the tube's capacity. In contrast to the final stage, the nonlinear stage of type A specimens is longer than that of type B, indicating higher ductility. This is demonstrated by the specimens' ductility index (Δ_u) in the pre-ultimate regime, which accompanies the transition from a linear to a nonlinear state. **Table 1** indicates that increasing the rigidity of tubes with a thicker shear-key increases compression strength but decreases ductility due to substantial shear stresses on the tubes once buckling begins. After the second nonlinear stage, the tube's local inward or outward bowing has occurred, and the specimen has reached P_u. During the third recession stage, a decrease in P_u is accompanied by intense local buckling. As noted in the generalized curves and Table 1, the ductility index (*DI*) of type A and type B specimens differ significantly in the post-ultimate capacity stage. In contrast to type A curves, which have a longer and smoother recession zone, type B specimens have a pronounced, rapid fall in capacity once they reach their ultimate stage. This may result from the reduced shear key and tube working effect reported in FD4 due to the shorter shear key, indicating that tubes cannot provide resistance after buckling.

3.3 Load-strain curves of shear-keyed grouped tubes

The vertical and horizontal axial load versus strain curves are summarized in **Fig. 9(a-d)**. It highlights information about the strain values and areas with prominent inward and outward buckling. Strain curves offer the same information as failure modes. When measured with strain gauges, it is also possible to gain information regarding the yielding or buckling of the location that is not readily apparent. It can be seen that all curves exhibit three distinct working phases: linear, nonlinear, and recession. As the load grew, the stresses rose linearly until they neared the nonlinear phase for achieving the ultimate resistances. The inversion, overturning, or abrupt decline of the strain curve indicates the existence of local buckling. Curves that turn behind or close to the yield strain imply elastic buckling. In contrast, plastic buckling occurs when the overturning curves surpass the yield strain. Moreover, overturning curves during the recession shows the onset of severe local plastic buckling. The S-shaped buckling exhibited by curves supported failure modes guided by grouped tubes, validating that inward and outward local buckling failures occurred sequentially in most shear-keyed tubes. BRBV-1 and BRBV-2 in FD2; BRBV-1 and BRBV-2 in FD3; and FLBV-1 and FLBV-2, FRBV-1 and FRBV-2, and SLTV-1 and SLTV-2 in FD4 validated the presence of S-shaped buckling. According to FD4, this pair of inward and outward buckling, such as FLBV-2, FRBV-1, and SLTV-1 (FLBV-1, FRBV-2, and SLTV-2), demonstrate local elastic (plastic) buckling.

In EC3, elastic buckling is permitted for Class 4; yielding and plastic buckling is allowed for Class 3 members. Since the grouped tubes are not Class 4 members, elastic buckling and no yielding would contradict EC3 slenderness limits. Numerous sections of FD2 exhibited elastic buckling and failed to attain yield, including FLTV-2, SRTV-2, and SRMV. FRTV-2 in FD3 and FLMH, FLMV, FRTV-1, FRMV, SLTV-1, and

SRML in FD4 also exhibited local elastic buckling. It demonstrates that shear-keyed grouped tubes failed to meet the EC3 criterion due to elastic buckling, which can be prevented by having no shear-key or adjusting shear-key t_t and L_t to moderate values, as indicated by FD3 and FD2 vs. FD4. Most FD1 welded grouped tube regions yielded and exhibited local plastic buckling. However, due to the influence of neighboring columns, the tube on the backside (BLBV) showed elastic buckling, demonstrating traditional column behavior variation attributable to neighboring or cluster column characteristics. This supports the non-conservatism of conventional codes, even for non-welded and welded grouped tubes supported with or without shear keys, and necessitates updating classification limits and proposing new sets of equations for the conservative design of shear-keyed grouped tubular columns in MSS.

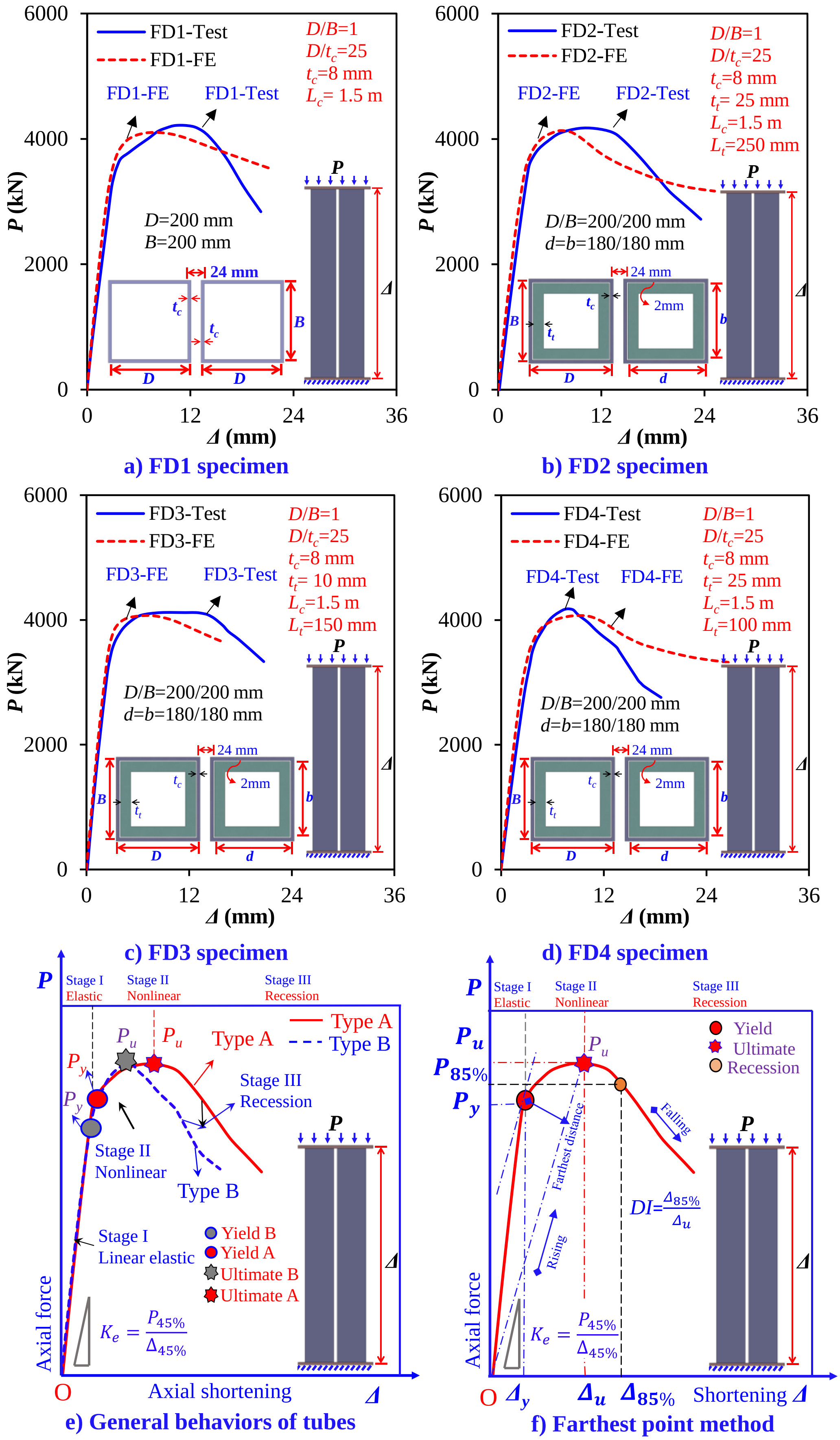

Fig. 8 Axial shortening curves of shear-keyed grouped tubes

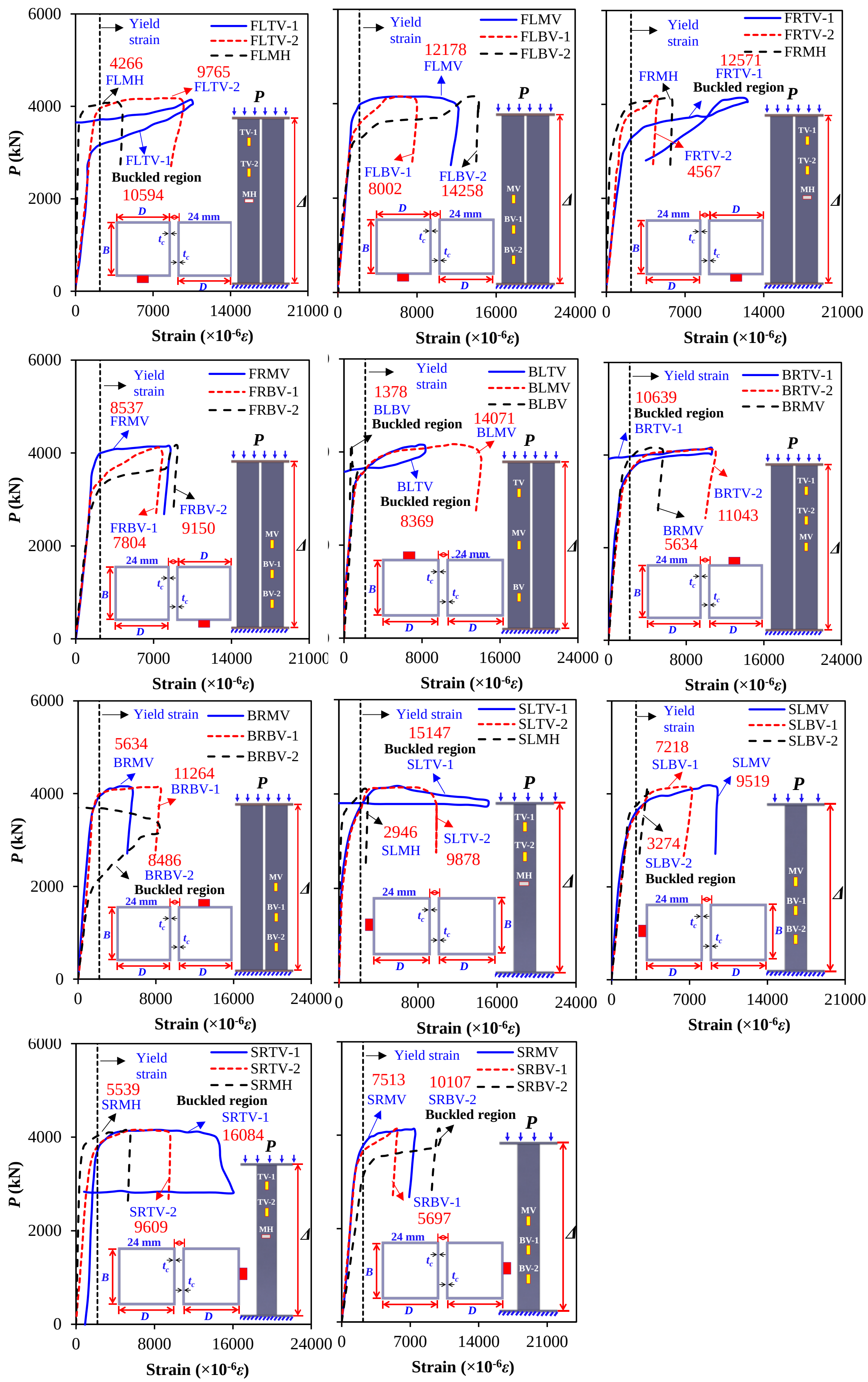

467 **a) FD1 specimen**

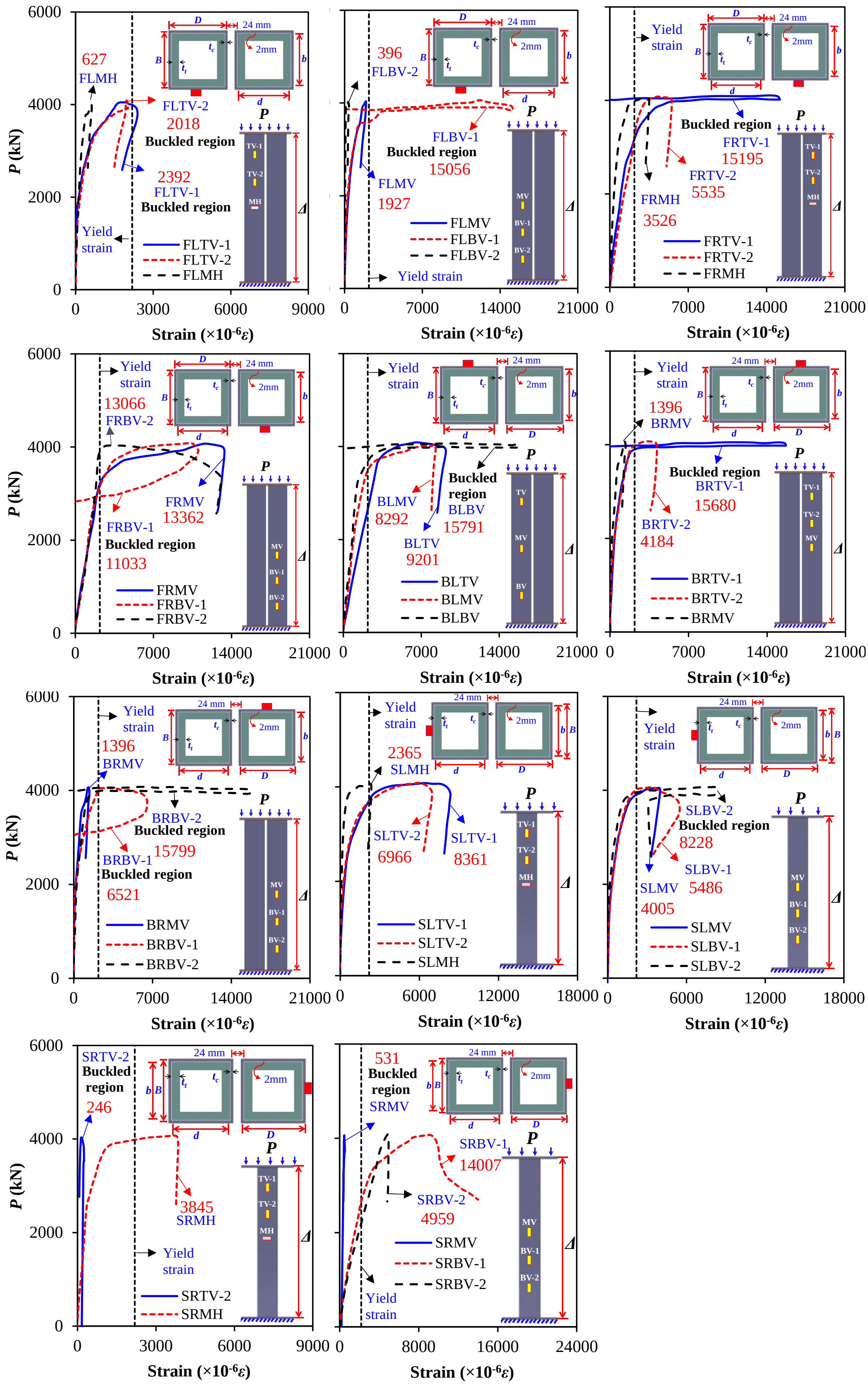

468 b) FD2 specimen

469

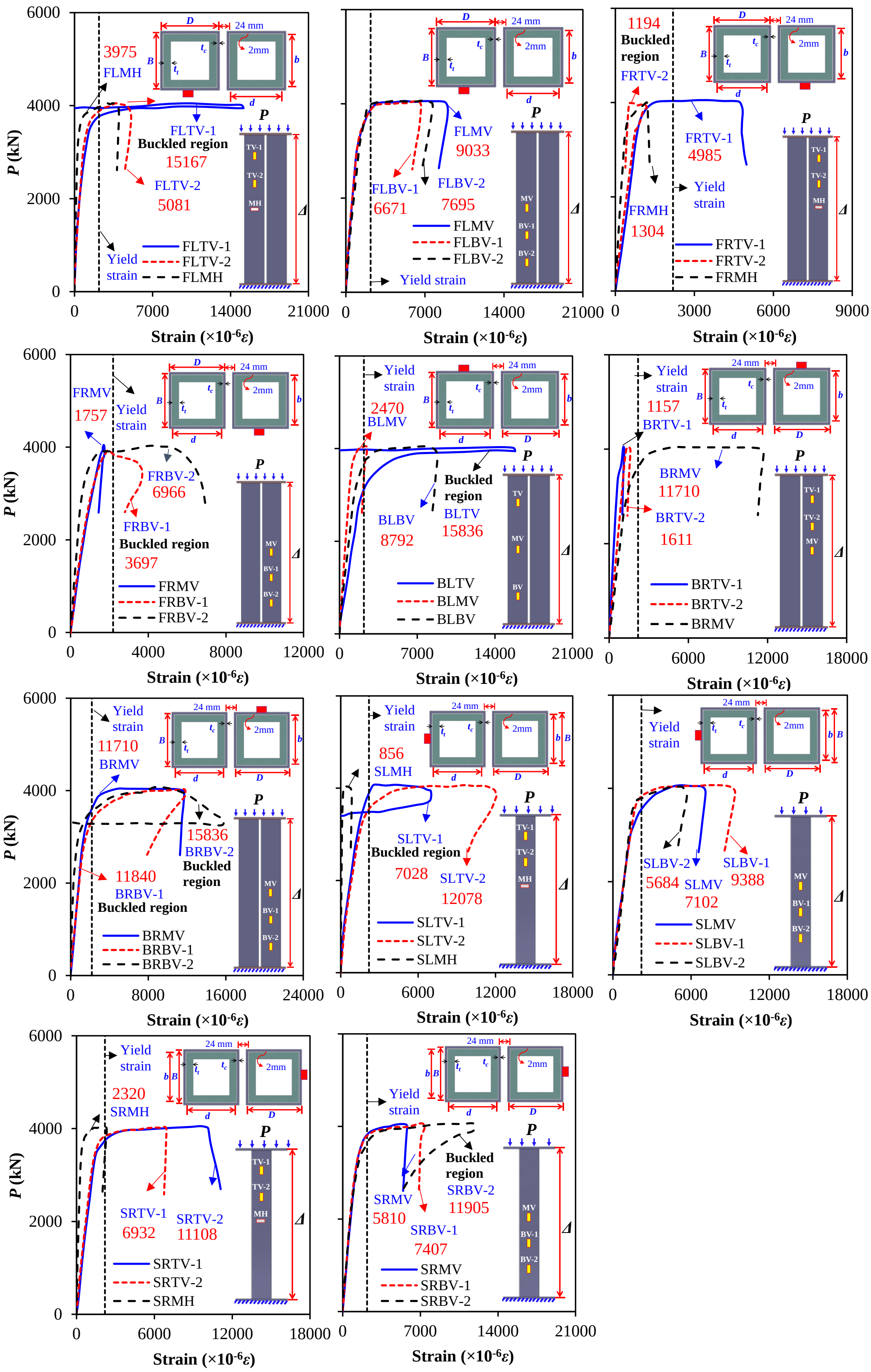

c) FD3 specimen

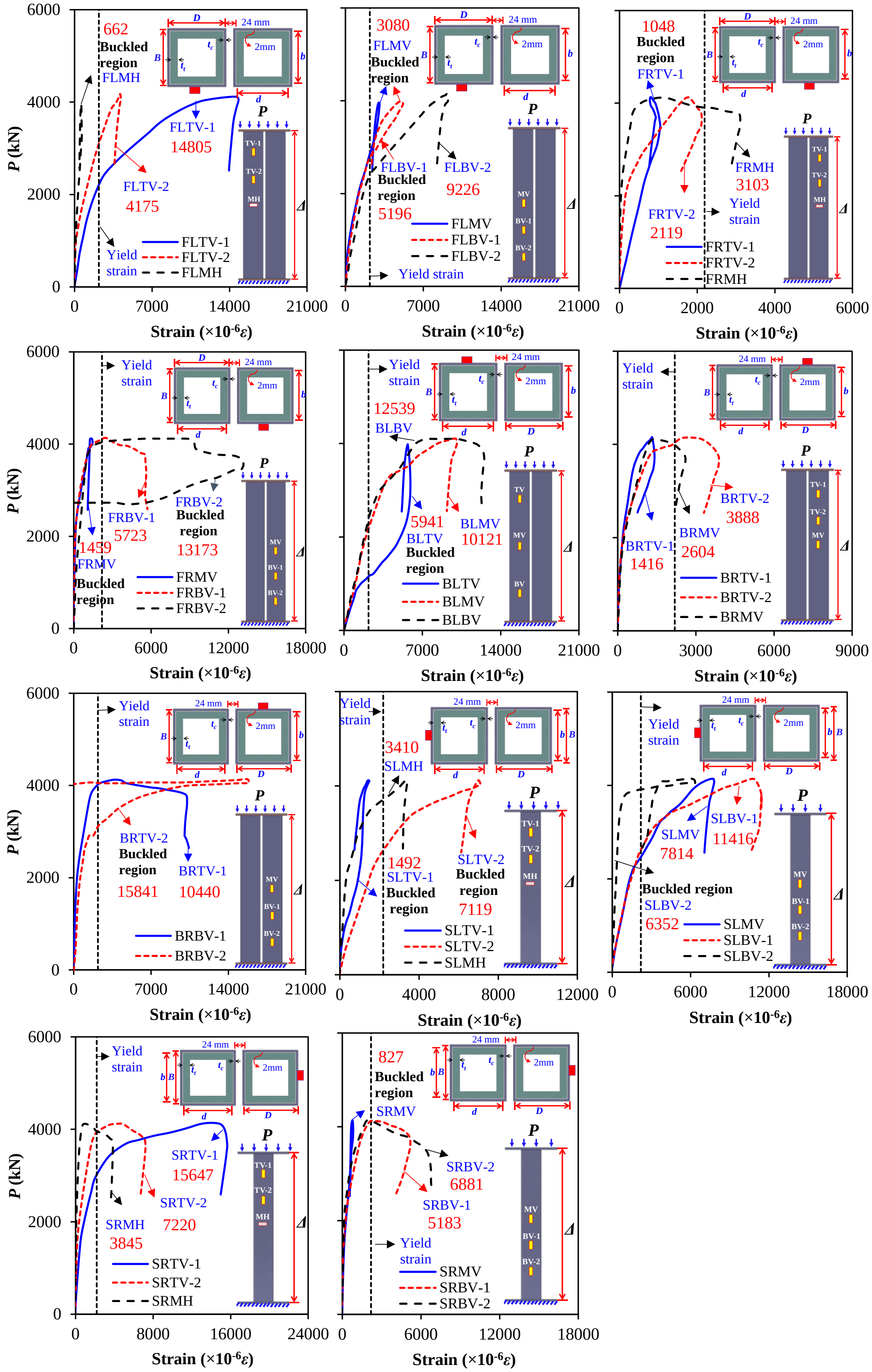

d) FD4 specimen

Fig. 9 Load versus strain curves of shear-keyed grouped tubes

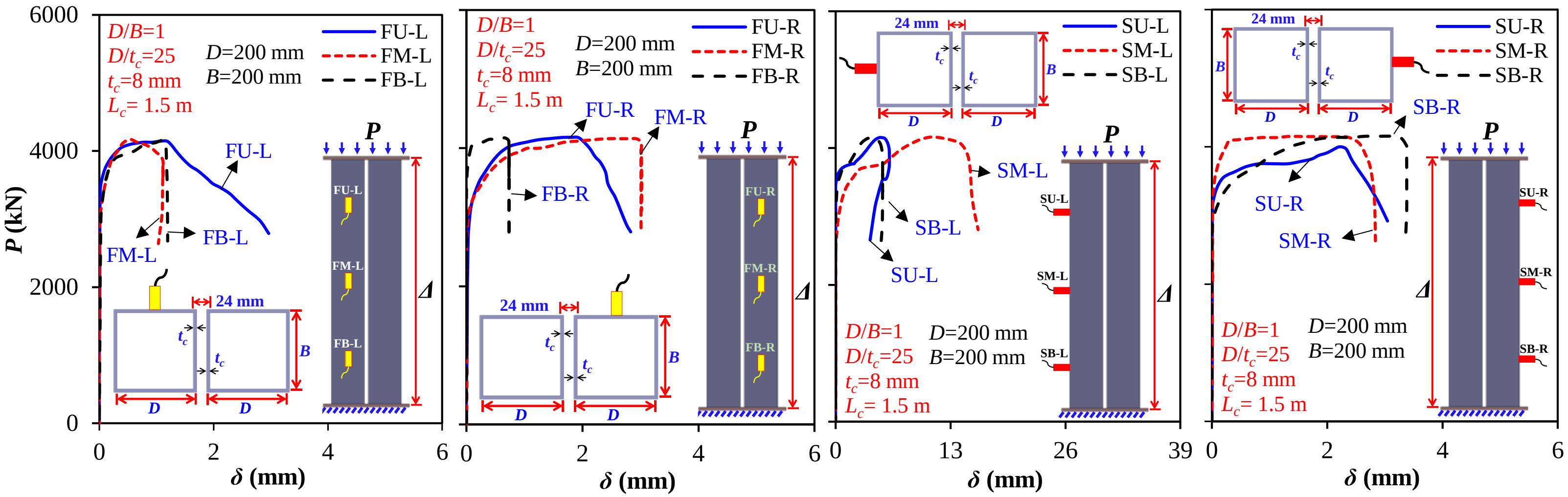

a) FD1 specimen

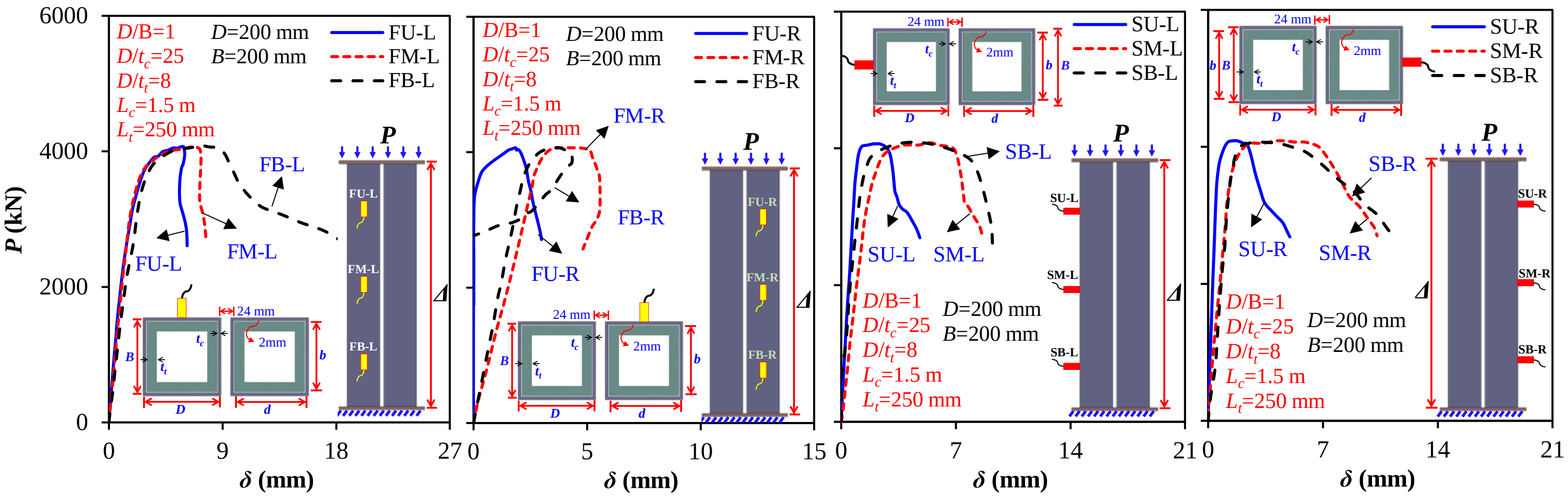

b) FD2 specimen

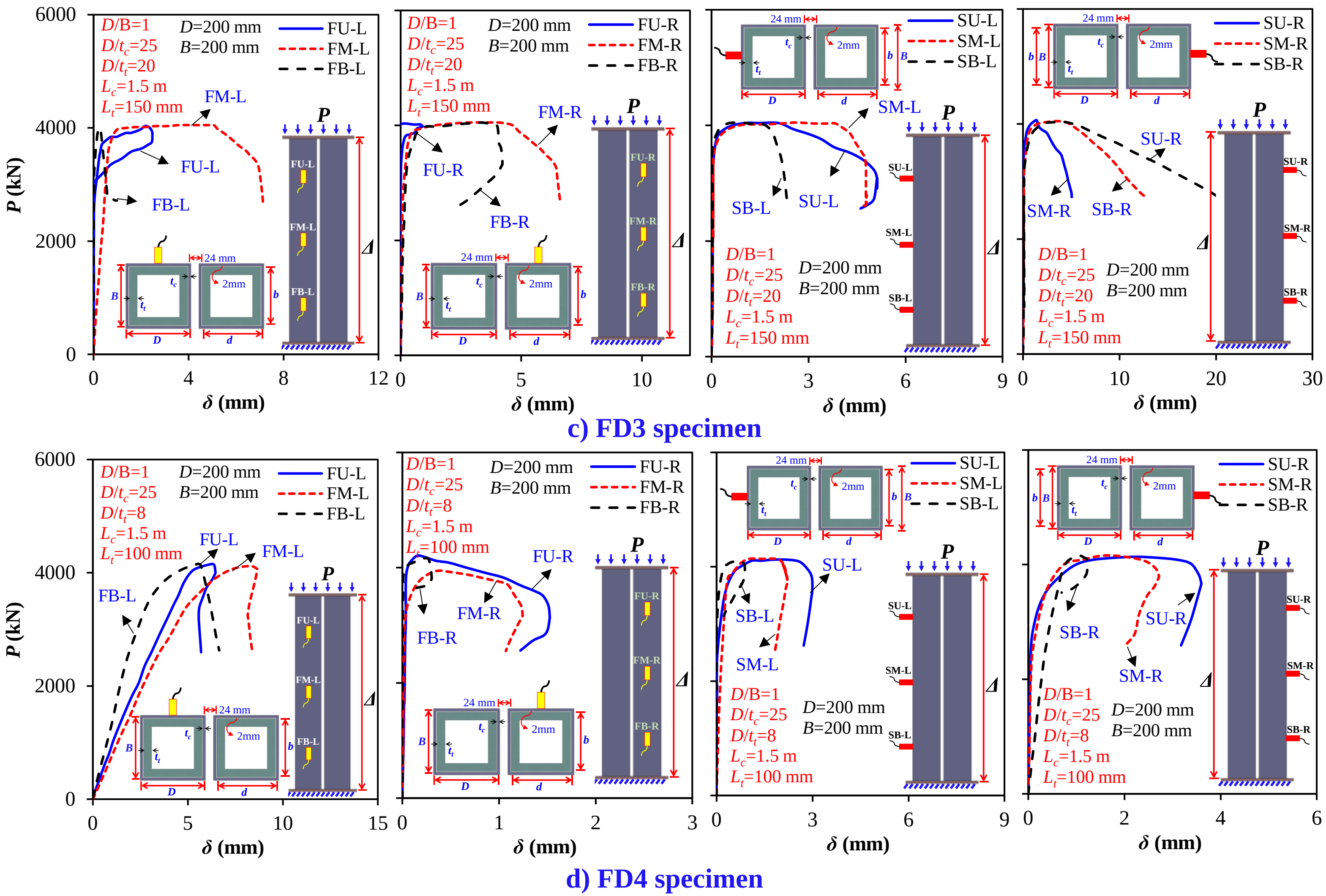

Fig. 10 Load versus deflection curves of shear-keyed grouped tubes

3.4 Lateral deflection curves of shear-keyed tubular columns

Figure 10(a-d) displays the load-deflection curve for each specimen in the front and side directions of the two neighboring tubes. These curves were used to determine whether or not buckling and lateral deflection were observed. The operating mechanism of the curves revealed linear and nonlinear stages but no recession phase. Due to the tubes' height, the columns' failure was limited to local buckling and not global buckling due to the more excellent compressive resistance. In contrast, the recession stage can only be prolonged if global buckling cause failure. As the load increases, the length and width deflection of the tube also increases. When the ultimate capacity is reached, this deflection remains steady, followed by a load and deflection increment stoppage. No noticeable in- or out-of-plane global buckling occurred, and specimens failed due to local buckling. Additionally, the degree of rotation variation due to non-welding or partial welding around shear keys can result in non-identical deflections displayed by adjacent columns on either side. Moreover, as the load grew, the stiffness of each curve of the two neighboring tubes dropped distinctly. The grouping effect and the non-welded shear keys revealed that square tubes behaved differently on each side and from adjacent columns. FD3 displayed a more remarkable resemblance between adjacent tubes' length and width deflections. This indicates that employing extremely rigid shear keys can enhance column uniformity, yet, column uniformity can suffer if shear-key stiffness is decreased. The curve's deflection and rigidity marginally validate the test failure modes. Notably, FD1 and FD2 failed near edges, as indicated by relatively greater FU-L, FU-R, and SB-R deflections. FD3 buckled near edges and at 1/4 to 1/2 column height, with the highest deflection indicated by FM-L, FM-R, SM-L, FB-R, SU-L, and SU-R. FD4 failed near edges, with FU-R, SU-R, and SU-L indicating maximum deflection.

3.5 Compressive resistance (P_u), axial shortening (Δ_u), initial stiffness (K_e), and ductility index (DI)

The load-shortening curves can calculate the ultimate load capacity (P_u) and axial shortening (Δ_u). Since shear-keyed grouped tube shortening curves exhibit linear behavior up to 80% of P_u, the initial stiffness (K_e) can be determined using Eqn. 1. Eqn. 2 can also be utilized to determine the ductility index (DI). The pre-and post-ultimate ductility is represented by the indices Δ_u and DI. The P_u, Δ_u, K_e, and DI values of the shear-keyed grouped tubes for the tested specimens are listed in Table 1[80,81].

$$K_e = {}^{P_{45\%}}/_{\Delta_{45\%}} \tag{1}$$

$$DI = {}^{\Delta_{85\%}}/_{\Delta_u} \tag{2}$$

where $P_{45\%}$, $\Delta_{45\%}$ and $\Delta_{85\%}$ denote the 45% load of P_u, axial shortening at $P_{45\%}$, and shortening at $P_{85\%}$, which can be determined using the method presented in **Fig. 8(f)** [82]. **Table 1** demonstrates that t_t and L_t have a considerable effect on the axial behavior of tubes, increasing P_u while decreasing Δ_u, K_e, and DI. FD2 and FD4 have a greater capacity than FD3 but less than FD1, which indicates that shear-key t_t and L_t improve tubes' compressive resistance. Still, their boundary conditions are weaker because they allow rotation. Columns without shear keys do not experience internal shear stresses or neighboring column weakening before buckling. This is because tube edge rigidity has risen.

4 Finite element analysis on shear-keyed grouped tubes compression behavior

Although the test provided valuable data, but not sufficient to support further research on shear-keyed grouped tubular columns. Using test failure modes, ultimate strength, strain, and LVDT data, a reliable FEM is generated to extend the study's range and evaluate parametric influence, which is difficult to discover from testing solely. The FEM is used to validate and support test conclusions.

4.1 General

The commercially available FE software ABAQUS was used for the finite element analysis (FEA) [83]. For modeling, ABAQUS/CAE was used. Linear elastic eigenvalue buckling analyses were conducted utilizing the subspace iteration approach to extract the buckling modes. Riks method was employed in the nonlinear analysis to discover the load-shortening behavior.

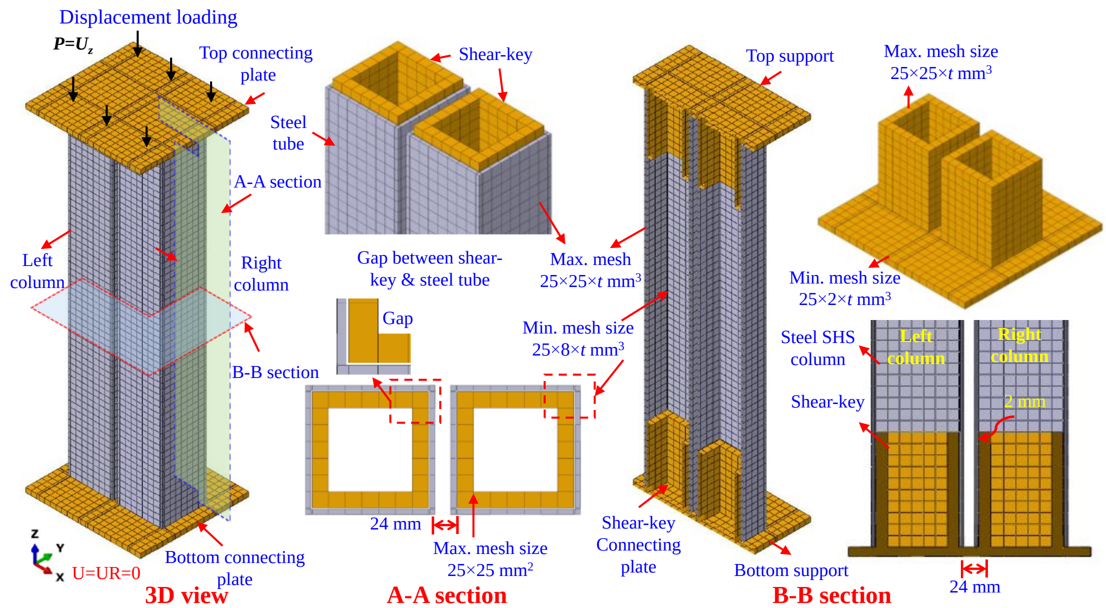

a) Details of experimentally validated FEMs

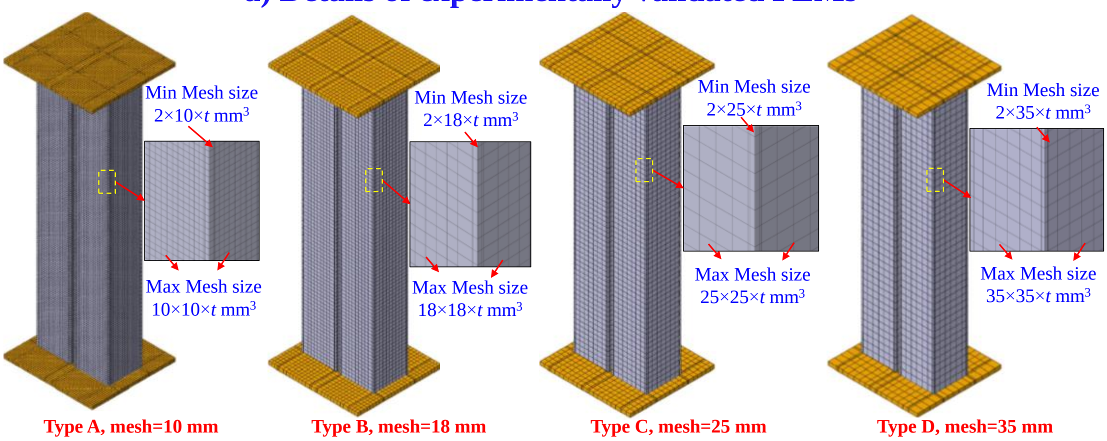

b) Parametric details of FEMs for mesh sizes

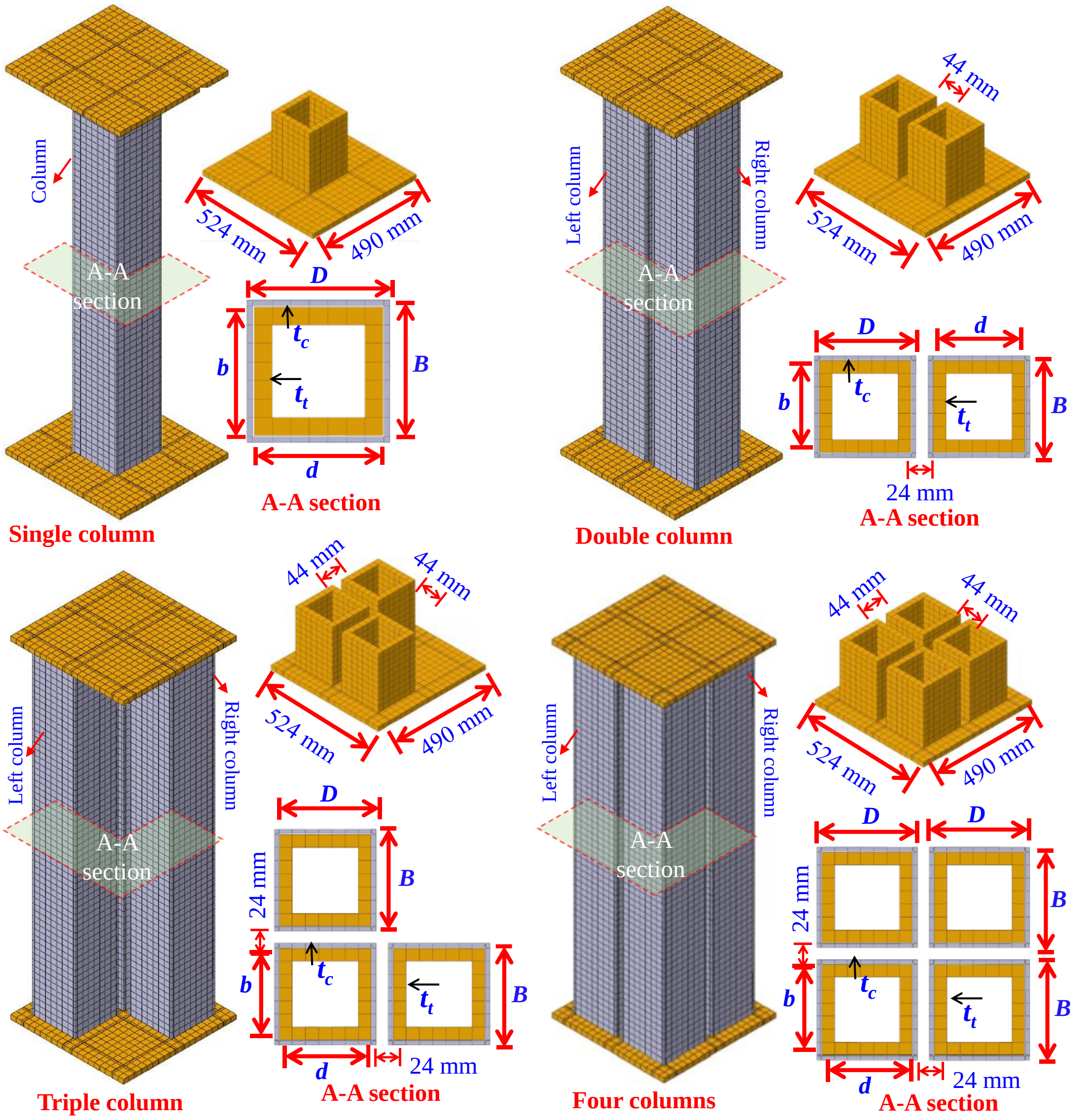

c) Details of varying columns numbers FEMs

Fig. 11 Shear-keyed grouped tubes developed FEM

4.2 Mesh sizes

Shear-keyed grouped tube mesh models comprised of steel tubes, connecting plates, and grouped shear keys welded to connecting plates, as shown in **Fig. 11**. **Figure 11(a)** exhibits specifics of the validated model, **Fig. 11(b)** depicts varying mesh types, and **Fig. 11(c)** shows details of column quantity. All components utilized deformable solid hexagonal structural mesh controls with an eight-node linear brick, reduced integration, and Hourglass Control Element Type (C3D8R), a recognized tool for simulating IMC and MSS structural components [35,36]. Because it affects FEA precision, the element size was carefully considered. As stated in the approach, different mesh sizes were employed [14–16]. A mesh study using types A, B, C, and D was undertaken with 100, 150, and 250 mm L_t to achieve precise mesh density. The P-Δ curves are depicted in **Fig. 12(a)**. **Figure 12(b)** presents the P_u, K_e, Δ_u, and DI ratios. The failure modes are shown in **Fig. 12(c)**. Four mesh type comparisons—A, B, C, and D—show that the P_u and K_e of FEA-generated curves drop and rise as mesh size decreases or increases. For example, as mesh size rises from 10 to 18, 25, and 35 mm for types A to B, C, and D, P_u (or K_e) increases by 87% to 143%, and 192% (80% to 147%, and 175%) with 100, 80% to 147%, and 175% (39% to 114%, and 92%) with 150, and 81% to 160%, and 201% (25% to 81%, and 88%) with 250 mm L_t. It also indicates Δ_u initially fluctuates between fine meshes; however, it reduces from 9% to 48%, 26% to 24%, and 24% to 27% as mesh size increases from 10 to 25 and 35 mm. Meanwhile, DI ratios scatter, indicating weaker agreement throughout the recession period. Additionally, the failure modes varied. It reveals that the failure modes of type A and B mesh models are located at the mid-height, but types C and D display local buckling on the column ends. Failure modes, P-Δ curves, P_u, K_e, Δ_u, and DI of type C mesh sizes yielded results similar to those of the tests in **Table 1**. Due to test validation accuracy and computational efficiency, FEM uses type C with a maximum size of 25×25×t and a minimum of 25×t×t for tubes. A non-calibrated FEM would provide inaccurate results, emphasizing the importance of shear-keyed grouped tube testing.

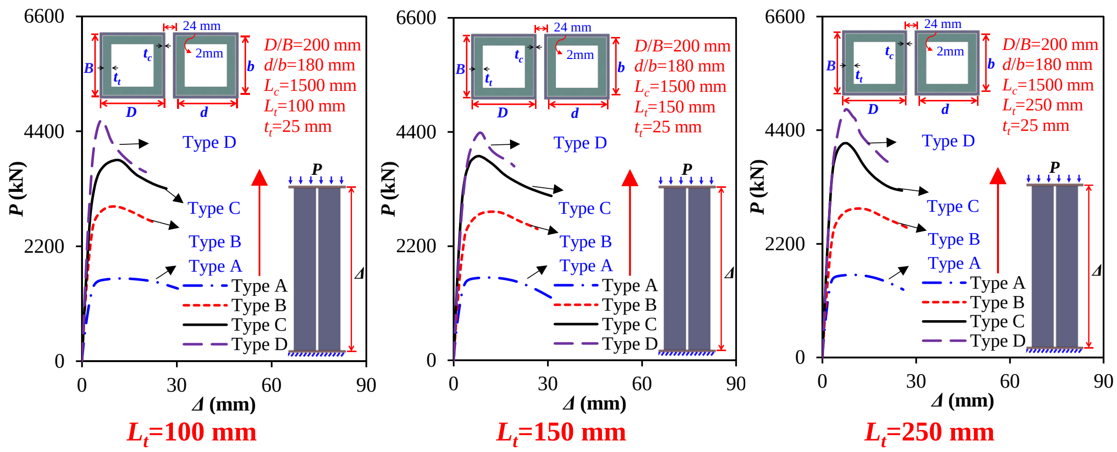

a) Effect of mesh on P-Δ curves

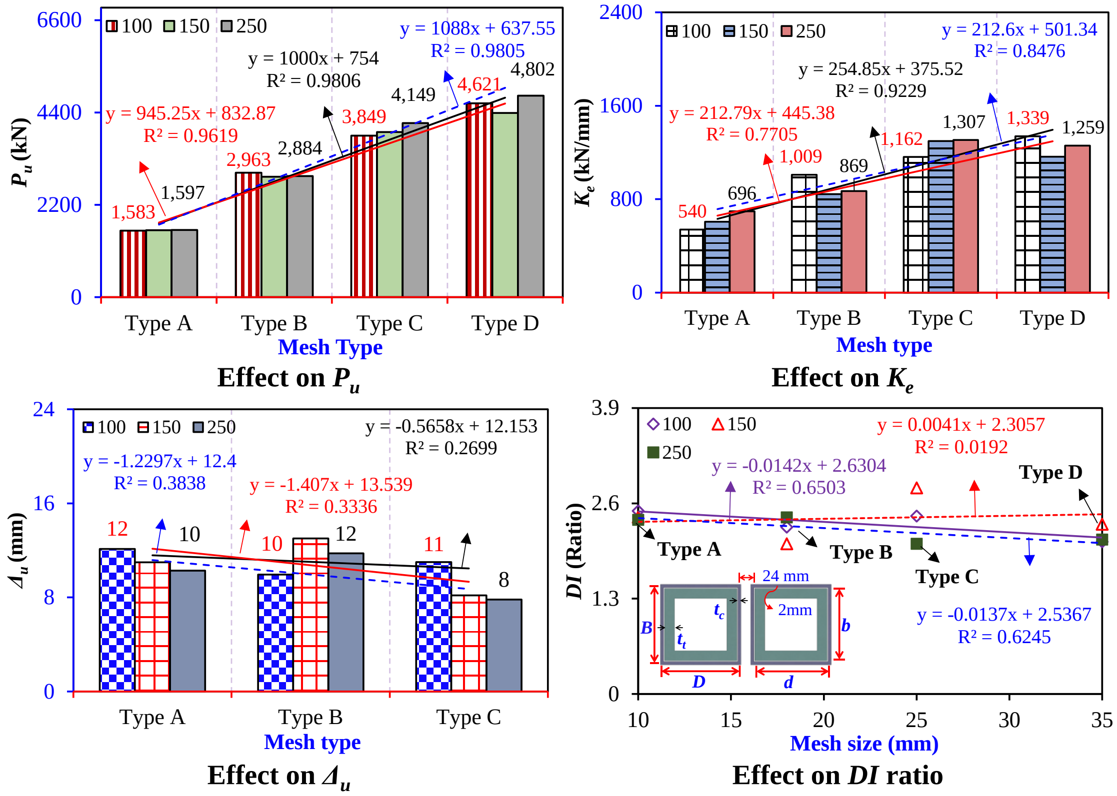

b) Effect of mesh on P_u, K_e, Δ_u, and DI

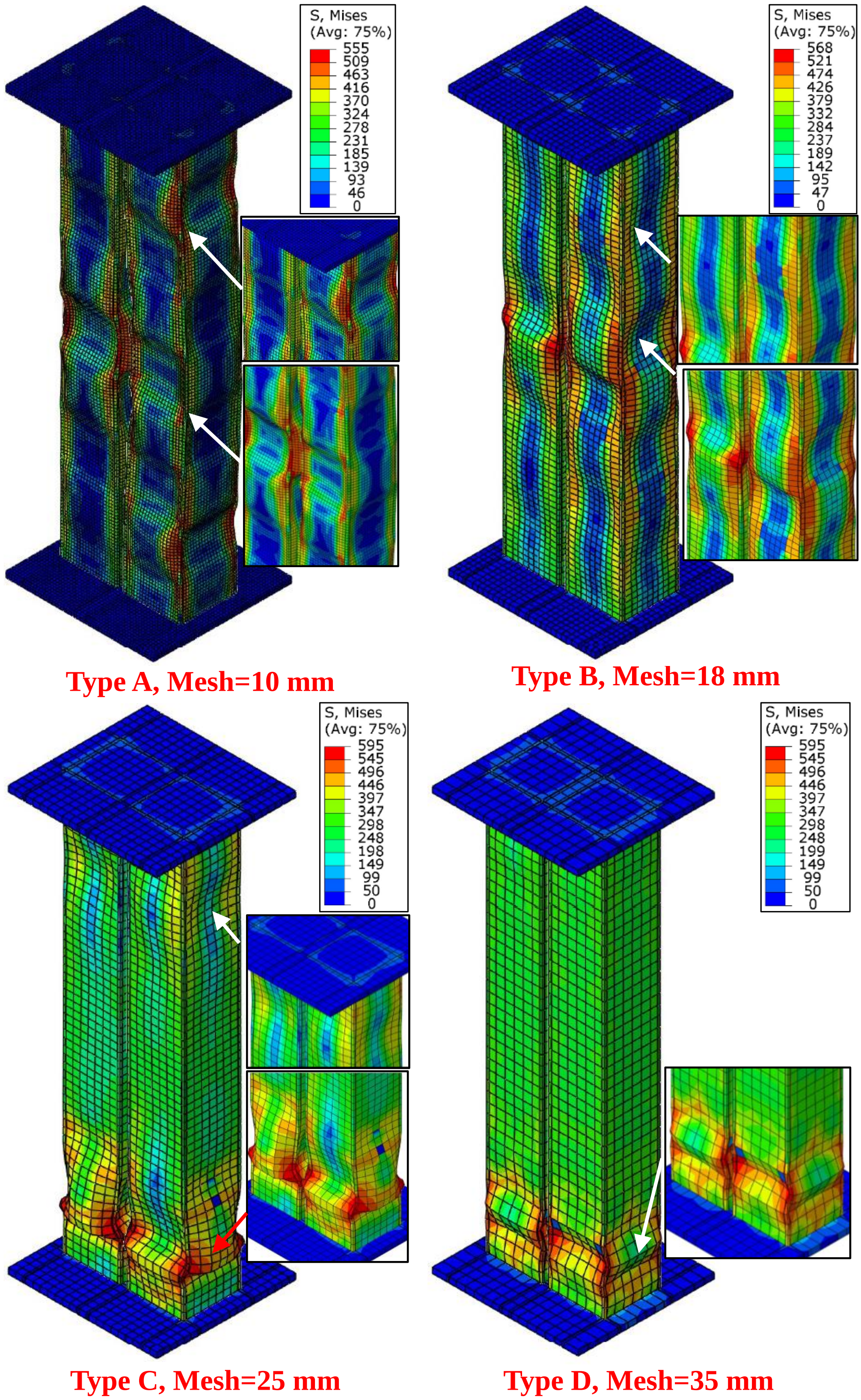

c) Mesh size effect on failure modes of similar tubes

Fig. 12 Influence of mesh size

4.3 Finite element model

The bottom region was allowed to move vertically, enabling shortening, while the top and bottom plates were restrained in all other directions. A column edge-coupling constraint reference point experienced displacement loading. Shear keys and connecting plates were welded in FD2, FD3, and FD4 specimens, whereas plates and tubes were welded in FD1. Therefore, surface-to-surface contact was used to create a "tie constraint" for fusing them. In the mentioned studies, the interaction of a column with connecting plates, a column with another column internally, and a column with shear keys were modeled as surface-to-surface with "hard contact" as the normal and "finite sliding" by "penalty friction formulation" as the tangential behavior [35,84]. This facilitates pressure transfer between different components. The *P*-*Δ* curves in **Fig. 13** indicate the effect of the friction coefficient between shear keys and tube surfaces at L_t of 100, 150, and 250 mm. As the friction coefficient rises from 0.1 to 0.2, 0.3, and 0.5, it displays a slight marginal improvement in P_u of less than 0.07%. For a L_t of 100 mm, the improvement in K_e and deterioration in *DI* reached 9% and 19%, respectively. In contrast, it resulted in an increase in Δ_u of 0% (2%, 1%), 9% (6%, 9%), and 6% (5%, 12%) for L_t of 100 (150, 250) mm. This is because the steel elastic modulus regulates the majority of internal friction and determines cross-sectional stiffness and ductility [82]. Thus, the exact friction coefficient was chosen to be 0.3.

Moreover, because the tubes and shear keys are made from hot-rolled steel sections, they have homogeneous material properties, are ductile and durable, have tight corner radii, and have minimal bending residual stresses [85]. The residual welding deformation did not influence member resistance; thus, the FEM capacity with and without residual effects did not differ more than 1% [86]. Therefore, the modeling ignored bending and residual stresses due to their minimal impact on validations [81], like the study on the MSB [11].

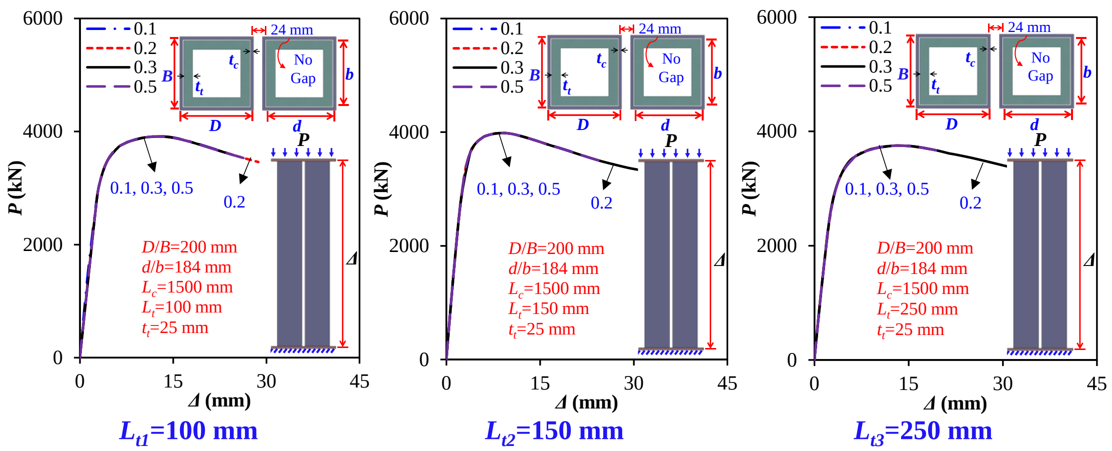

Fig. 13 Influence of friction and connecting plate

4.4 Material simulation

Shear-keyed grouped tube components using an elastic-plastic model with kinematic hardening based on the von Mises yield criterion, with material definition required the properties specified in **Table 1**. As shown in **Fig. 8(f)**, Eqns. 3 and 4 replace the engineering stress-strain values with a bi-linear true stress-strain. Poisson's ratio equals 0.3.

$$\sigma_T = \sigma_E(1+\varepsilon_E) \tag{3}$$

$$\varepsilon_T = \ln(1+\varepsilon_E) - \frac{\sigma_T}{E_s} \tag{4}$$

where σ_T and ε_T define true stress-strain while σ_E and ε_E indicate Engineering stress-strain.

4.5 Initial imperfection modeling

The test specimens were hot-rolled, non-welded tubes with shear keys inserted at both ends. Since both the tubes and the shear keys contribute to compression resistance and have a possibility of developing initial defects, it is challenging to evaluate imperfections by moving the LVDT along the uneven surface [81]. Moreover, due to the high-quality installation, severe defects are practically inevitable in MSS; consequently, it is essential to investigate the effect of excessive imperfection on shear-keyed grouped tube compression behavior. Design standards suggest various initial imperfections covering members out-of-straightness, varying between *1*/500 and *1*/200, with L/1000 recommended for global imperfections and L/1996 reported for hot-rolled members [87]. It is reported that an amplitude equal to L/1000 produces the most precise findings [88]. Thus, following these studies, initial imperfections were modeled and compared with the test results to obtain accurate amplitude. Therefore, tube imperfection in Ref. [12] dealing with hot-rolled tubes in MSB and cold-formed tubes in Ref. [53] were compared to obtain the accurate conservative imperfection amplitude shear-keyed grouped tubes. Theofanous and Gardner [53] suggested local and global imperfections attributed to cross-section thickness (t) or height (L) and eccentricity (e). The study selected tubes thickness (t_c) values of t/100, t/10, t/5, t/2, and t; tube height (L_c) values of L/2000, L/15000, L/1000, and L/500; and eccentricity (e) values of D/20, D/8, and D/4, and compared the test results. In the study, t was t_c, and L was L_c. **Figure 14(a-c)** depicts the impacts on P-Δ curves, whereas **Fig. 16(a-f)** displays P_u, K_e, Δ_u, and DI. It was discovered that increasing amplitude from t/100 to t/10, t/5, t/2, and t lowered P_u (or K_e) by 2% to 5%, 10%, and 17% (3% to 7%, 19%, and 33%). Whereas increasing from L/2000 to L/1500, L/1000, and L/500 dropped P_u (or K_e) by 1% to 2% and 6% (1% to 4% and 12%). Additionally, increasing from t/100 to t/10, t/5, t/2, and t, and L/2000 to L/1500, L/1000, and L/500 did not influence DI but raised Δ_u by 1% to 21%, 50%, and 111%, and 5%, 25%, and 53%. Compared to the test, the initial imperfection of 7/8t or 7L/1500 is optimal for predicting capacity.

Eigenmode analysis yielded initial buckling modes in **Fig. 15(a,b)** for welded and shear-keyed grouped tubes. They were used to compare with test failure modes, determine the failure mode closest to the test failure mode, and apply the imperfection amplitude to nonlinear analysis. Then, the nonlinear Riks analysis chose the closest buckling mode derived from the buckling analysis and compared it to the test failure modes in **Fig. 7(a-d)** for the imperfection amplitude input. Comparing the test failure modes with each load-shortening curve in **Fig. 8(a-d)** for each specimen yields geometric imperfections. Failure modes can vary, such as this study selected 1st buckling mode for FD1 and FD3 and 3rd for FD2 and FD4 depending on the position of buckling; the imperfection amplitude determined in **Fig. 14** was utilized for all specimens and models examined in Table A1 that estimated their *P-Δ* curves with reasonable accuracy. This approach has been applied in numerous studies, such as Arrayago et al. [87], Lyu et al. [11], Theofanous et al. [53], Lyu et al. [12], and Yan et al. [81], for applying and determining the initial imperfections.

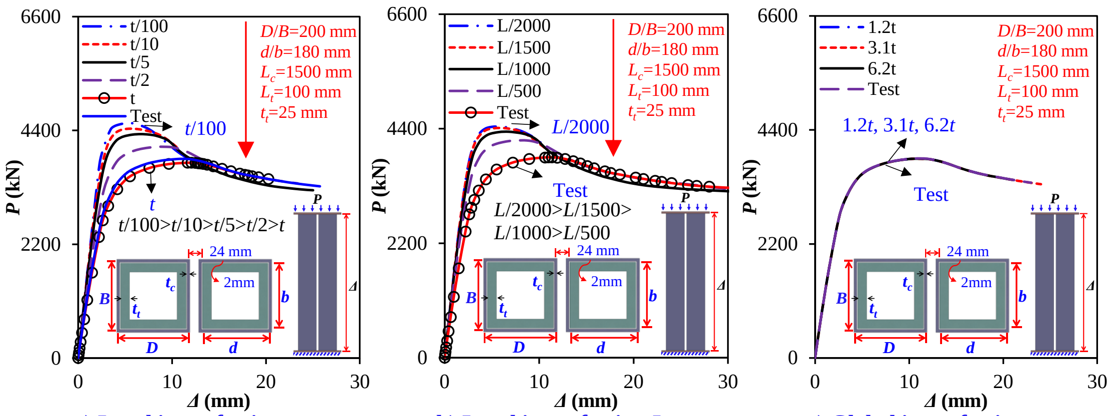

a) Local imperfection t_c b) Local imperfection L_c c) Global imperfection *e*

Fig. 14 Influence of initial imperfection

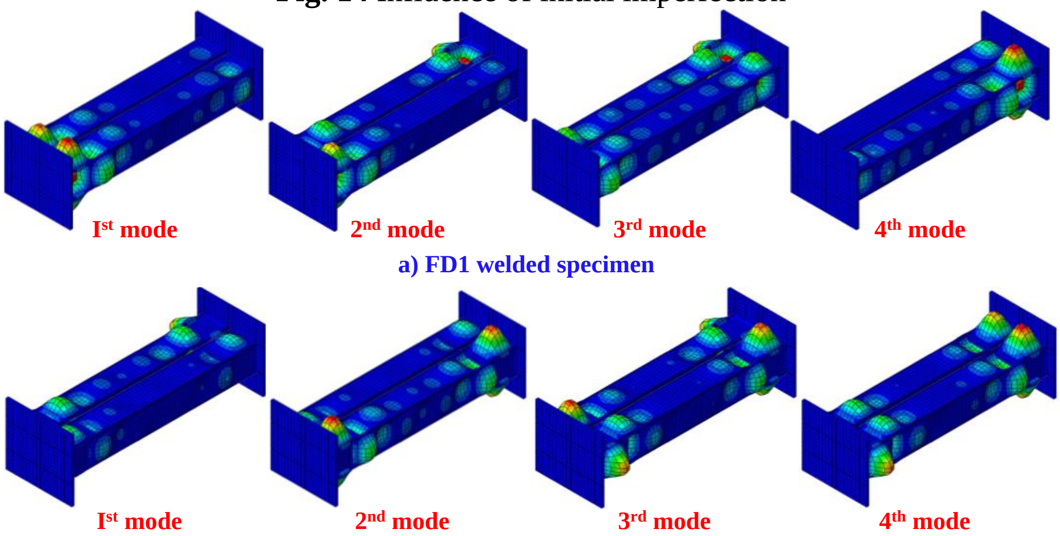

Fig. 15 First four buckling modes

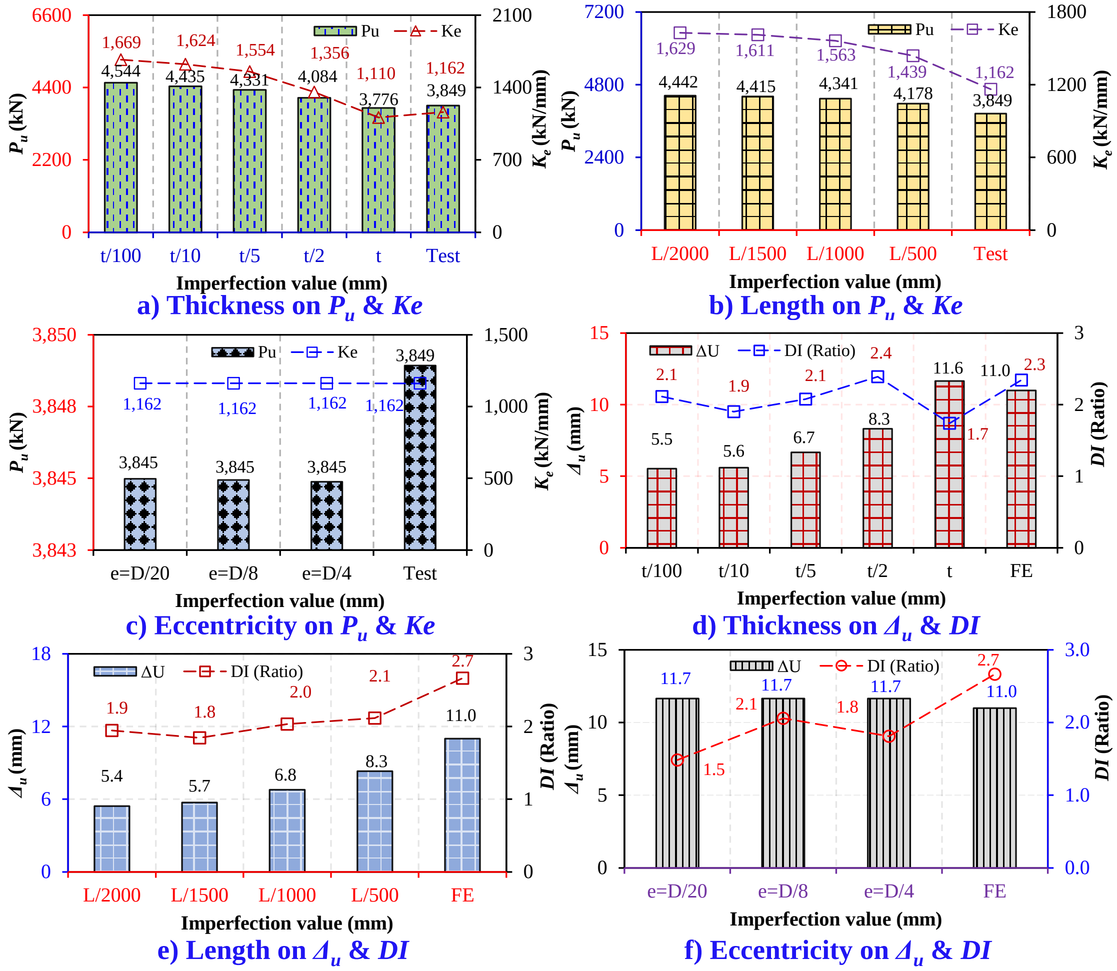

Fig. 16 Influence of initial imperfection

4.6 Validations

Four large-scale shear-keyed grouped tube axial compression tests failure mechanisms and shortening curves are used for validations. **Table 1** and **Figs. 8(a-d) and 17** illustrate the test-to-FEA load-shortening curves and dispersion ratios of P_u, K_e, Δ_u, and DI. It demonstrates the FE's average estimations for P_u, K_e, Δ_u, and DI during four testings, 1.02, 0.83, 1.13, and 0.84. Ratios greater than 1.0 show that FE is slightly overestimated, while ratios less than 1.0 reveal that the test has been overestimated. It indicates that the FE produced average minor prediction errors of 1.8% for P_u and 8.6% for Δ_u but substantial scatters and overestimates for K_e and DI with an average of 20.9% and 22.4%. This was primarily due to issues over soft support, material model and gap variance, geometric simplifications, and initial imperfections.

Figure 18(a-d) compares the FEA-obtained deformed shapes and von Mises stress distributions of shear-keyed grouped tubes to the experimental outcomes. It demonstrates that the developed FEM can accurately predict both neighboring tubes' symmetrical and unsymmetrical deformed shapes and failure locations. For instance, local inward and outward buckling at shear-key edges or mid, column mid-height, and 1/4 to 1/2 column height. It also accurately anticipated the S-shaped sinusoidal failure mode with sequential inward and outward buckling pairs. These validations reveal that the proposed FEM accurately predicts the compression behaviors of shear-keyed grouped tubes.

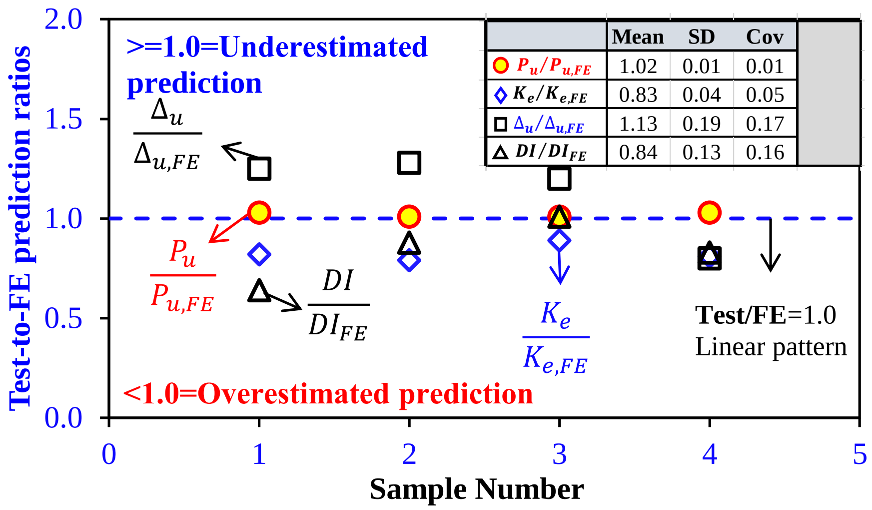

Fig. 17 Comparisons of test to FE-predicted scatters

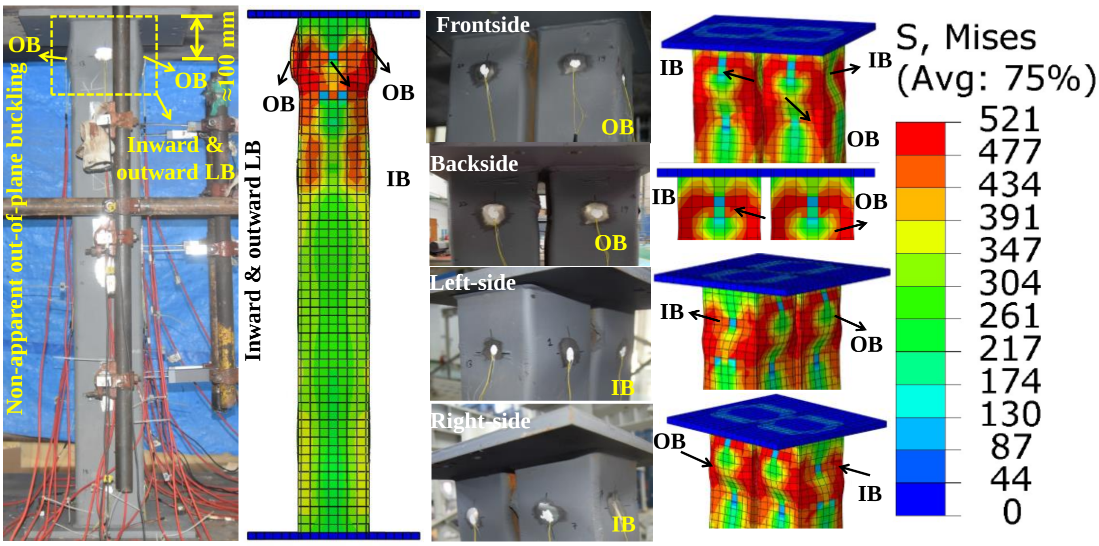

a) FD1 specimen

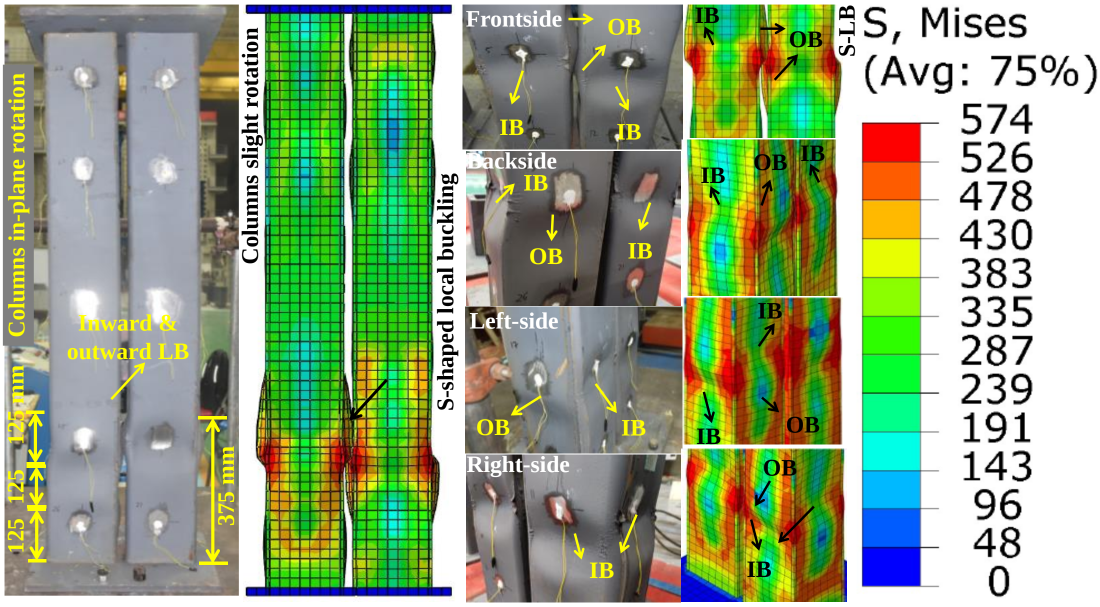

b) FD2 specimen

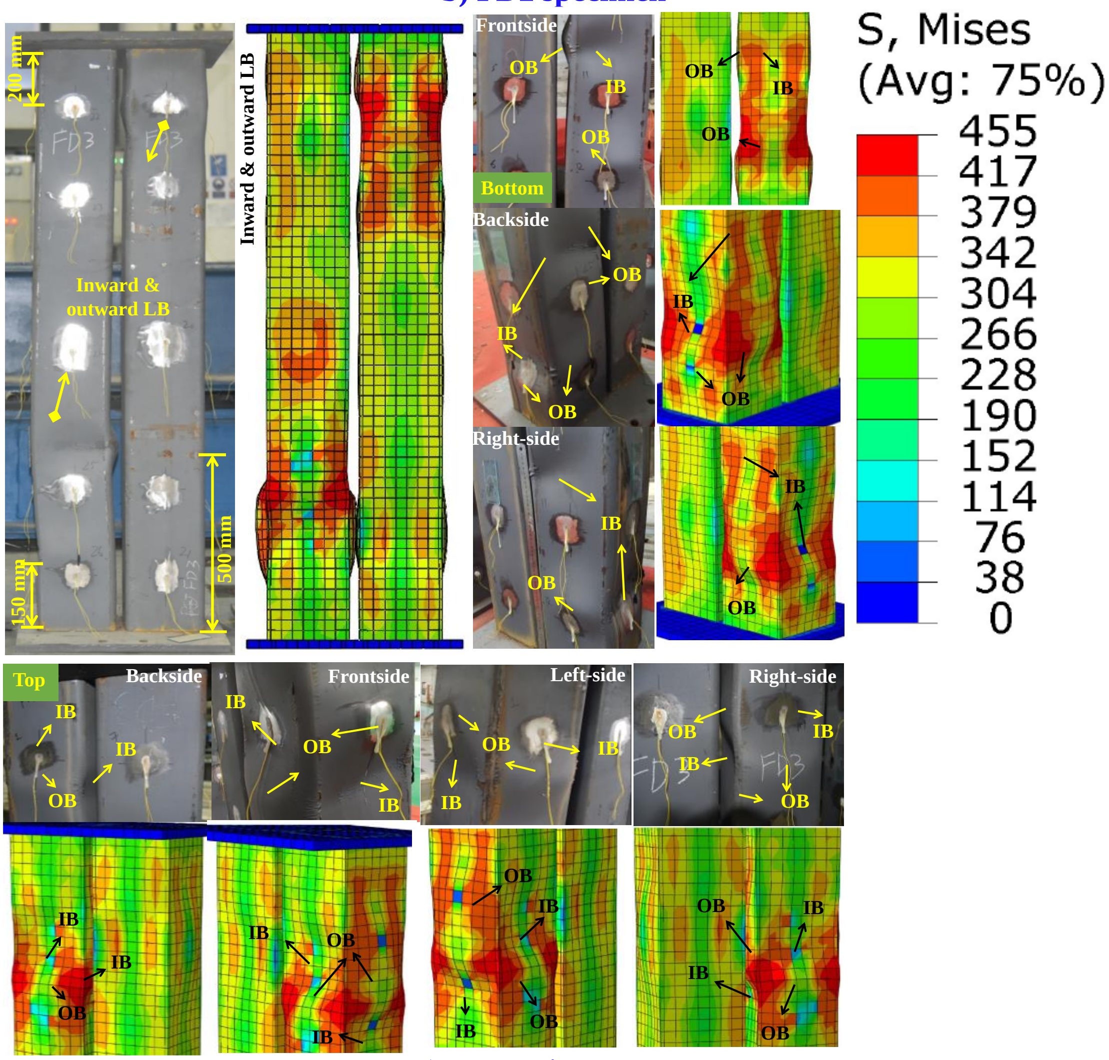

c) FD3 specimen

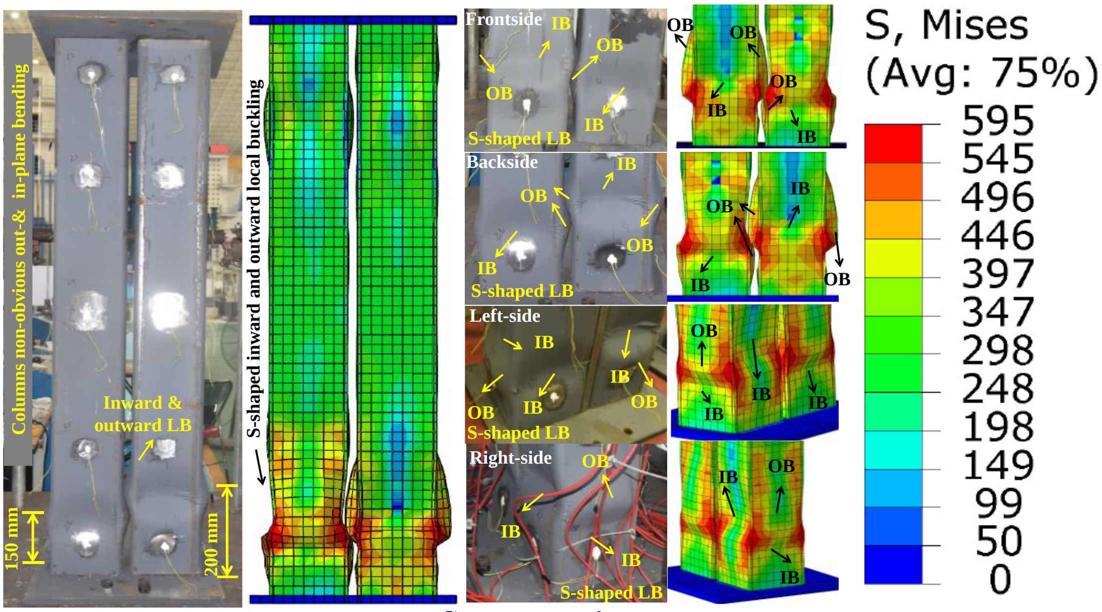

d) FD4 specimen

Fig. 18 Comparisons of test to FE-predicted failure modes

5 Discussions using parametric analysis

5.1 Investigated parameters and behaviors

The effects of shear-key thickness and height, length-to-width ratios, tubes-key gap, steel tube thickness, height, and length-to-width ratios, columns spacing, number, and connecting plate thickness on the compressive behavior of shear-keyed grouped tubes were studied using validated FEMs. These FEMs are categorized into nine groups by varying t_t (5, 10, 35, and 180 mm with 100, 150, and 250 mm L_t), varying L_t (50, 100, 200, and 400 mm with 5, 10, 35, and 180 mm t_t), varying L_c (1.0, 1.5, 2.0, and 3.6 m with 50, 100, 200, and 400 mm L_t), varying t_c (5, 7, 8, and 9 mm with 1.5 m L_c, and 100, 150, and 250 mm L_t), varying D/B (150/150, 180/180, 250/250 mm with 100, 150, and 250 mm L_t), varying d/b (184/184, 180/180, 176/176, and 172/172 mm with 100, 150, and 250 mm L_t), varying connecting plate thickness (15, 20, 30 mm with 100, 150, and 250 mm L_t), varying spacing (0, 6, 24, and 36 mm with 100, 150, and 250 mm L_t), and varying column numbers (1, 2, 3, and 4 with 100, 150, and 250 mm L_t). As columns showed varying relationships on P_u, K_e, Δ_u, and DI, the influence of each parameter on these indexes would be the emphasis. **Supplementary Table A1** lists further information about parameters and P_u, K_e, Δ_u, and DI for these models.

5.2 Typical failure behavior

The failure modes of stubs, intermediate, and long shear-keyed grouped tubes are summarized in **supplementary Fig. B1**. It demonstrates that there was no noticeable global buckling detected. Because of nonrigid constraints, the tubes rotated slightly around shear keys. Neighboring tubes exhibited symmetrical or asymmetrical local inward and outward buckling, confined at shear-key edges or 1/4 to 1/2 column height in both tubes' top or bottom locations. Furthermore, all tubular columns with 1, 2, 3, and 4 shear-keyed tubes demonstrated visible S-shaped local inward and outward buckling, identical on opposing tube sides while opposite on nearby faces. In short and intermediate columns, the S-shaped failure was more obvious than in long tubes. Furthermore, tubes on two, six, and eight surfaces in two, three, and four columns contact each other without penetration, exhibiting a coupled S-shaped failure. Long or large cross-section tubes have stress localization at the shear keys end, causing local buckling. While the column's or shear-key height is reduced or increased considerably, the behavior becomes uniform, extending the failure away from the edges to mid or between 1/4 and 1/2 height.

5.3 Influence of shear-key

5.3.1 Shear-key thickness (Δt_t)

Figures 19(a-c) illustrate the influence of the t_t (5, 10, 35, 180 mm) on the P-Δ curves. **Figure 20(a-d)** shows its effect on the P_u, K_e, Δ_u, and DI ratios with varied L_t. Raising t_t positively impacts P_u and K_e but negatively influences Δ_u and DI. These findings are entirely compatible with test findings. As the t_t increases from 5 to 35 and 180 mm, the P_u (K_e) increases by 4% and 4% (10% and 3%), 29% and 13% (13% and 6%), and 34% and 24% (67% and 59%) with 100, 150, and 250 mm L_t. This is because increasing the

t_t value increases steel content, reduces slenderness and improves overall compressive resistance. However, the impact on Δ_u (and DI) was negative, with falls of 38% and 9% (60% and 53%), 43% and 3% (31% and 11%), and 52% and 50% (21% and 10%) for 100, 150, and 250 mm L_t. Increasing shear-key rigidity results in plastic buckling rather than elastic. This increases tube yield strength while decreasing buckling strain and recession, reducing Δ_u and DI.

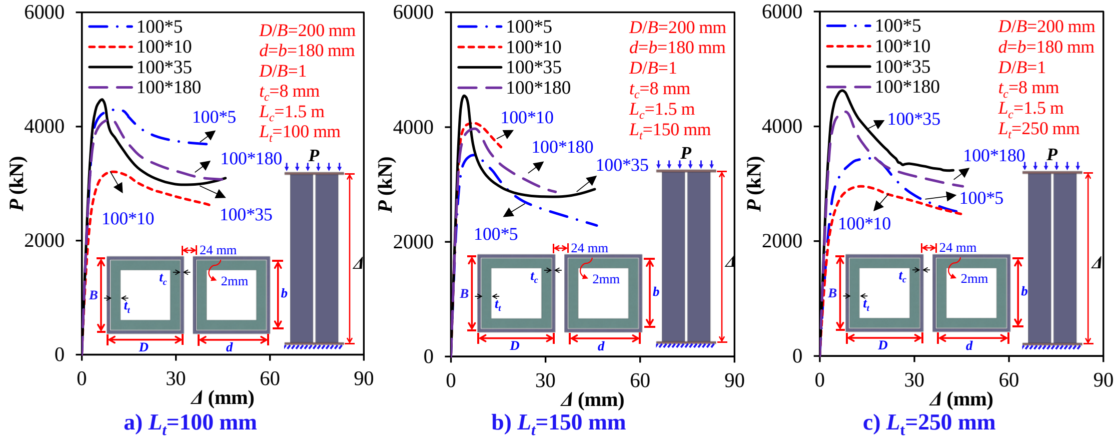

Fig. 19 Effect of Δt_t

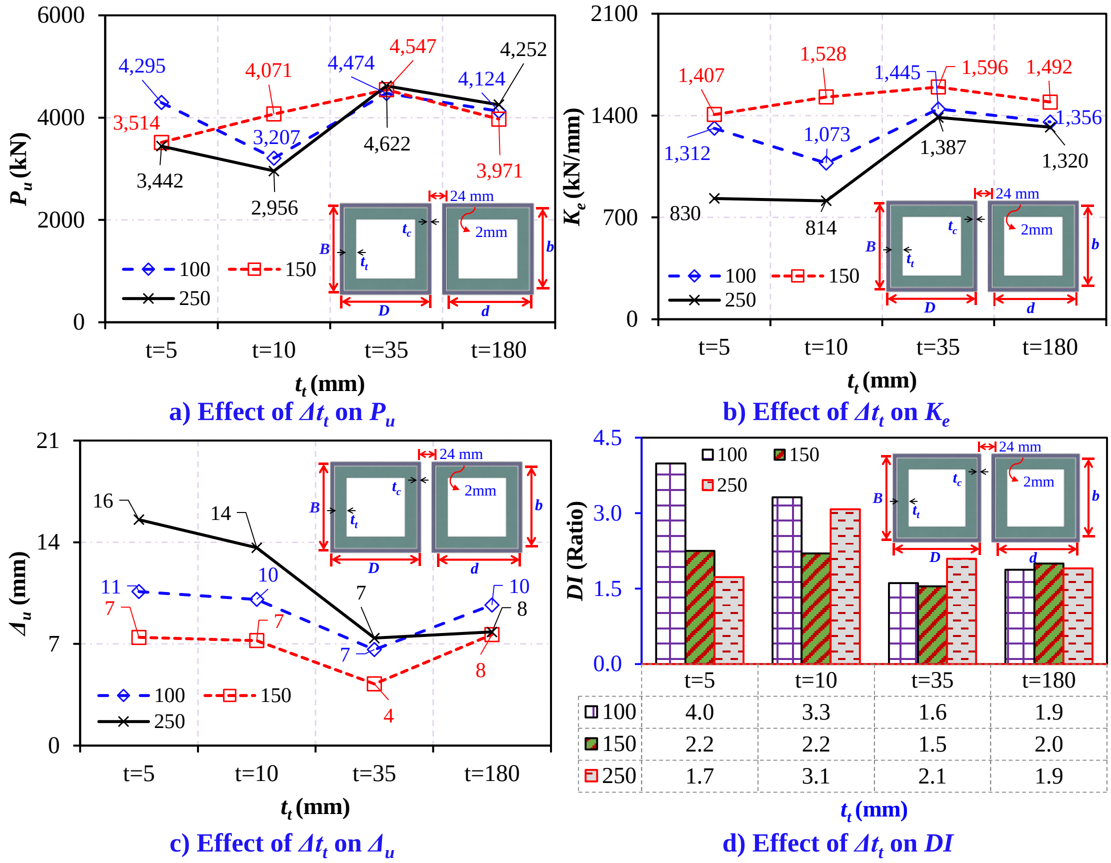

Fig. 20 Effect of Δt_t

5.3.2 Shear-key length (ΔL_t)

Figures 21(a-d) demonstrate the L_t contribution to the *P-Δ* curves. **Figure 22(a-d)** shows its influence on the P_u, K_e, Δ_u, and *DI* ratios with various t_t. It indicates that increasing L_t has a large positive impact on P_u and K_e but a weaker relationship on Δ_u and *DI*. These are completely compatible with test findings indicating as the L_t grows from 50 to 100, 200, and 400 mm, the P_u (K_e) increases by 1% (2%), 3% (7%), 3% (7%) and 13% (48%), with 5 mm t_t, and 1% (2%), 2% (1%), 2% (1%) and 13% (8%), with 180 mm t_t. Increasing the L_t value promotes overall buckling resistance due to shear keys' enlargement, making a connecting plate to the tube joint more rigid. Furthermore, modifying L_t had a minimal effect on the Δ_u and *DI*, yet, the impact on Δ_u of the 5 mm t_t was noteworthy by dropping to 1 %, 12%, 12 %, and 53% because the shear key tube offered lesser contact length, reducing buckling strain, which reduces ductility, as demonstrated in **Figs. 9 and 22**.

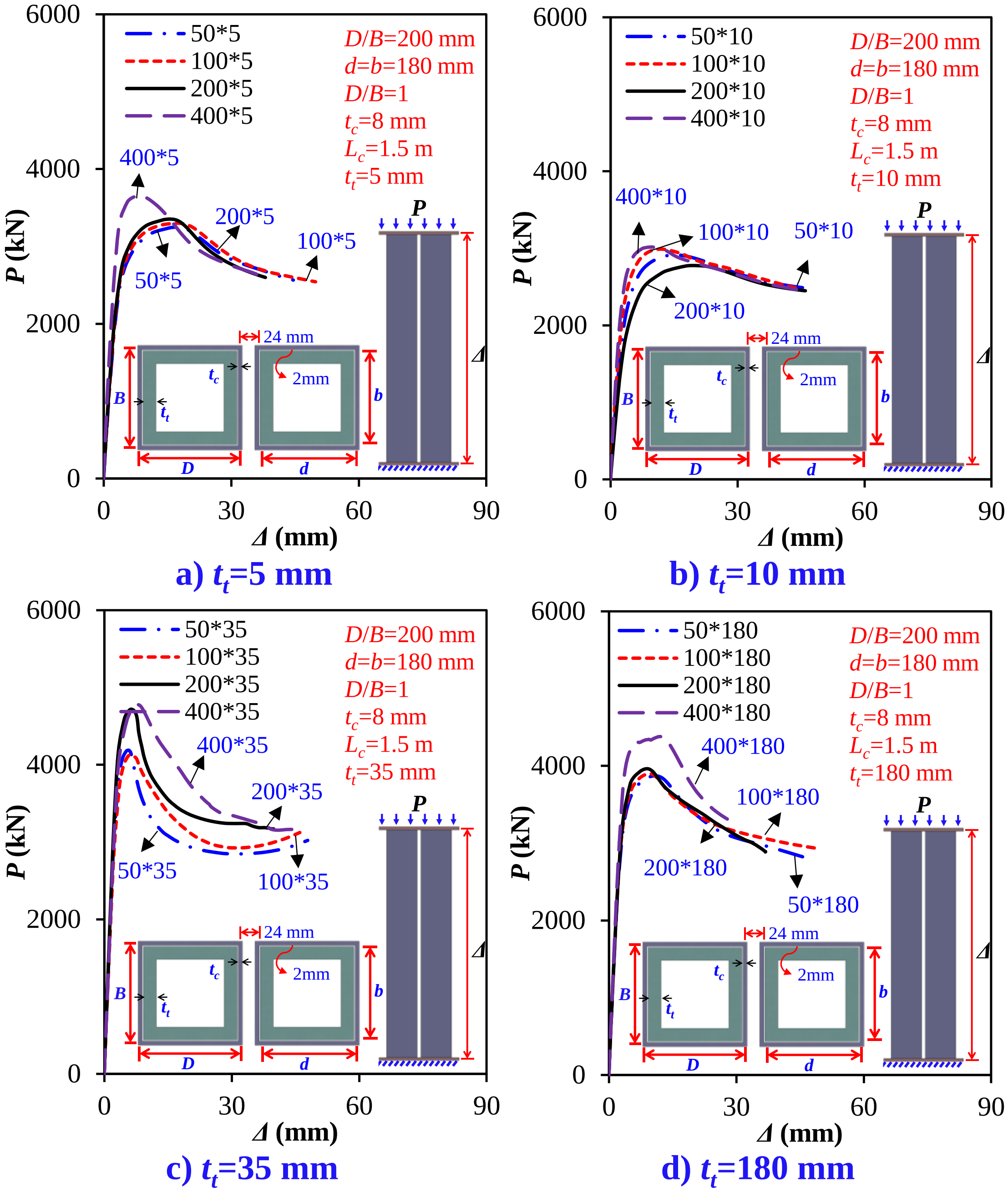

Fig. 21 Influence of ΔL_t

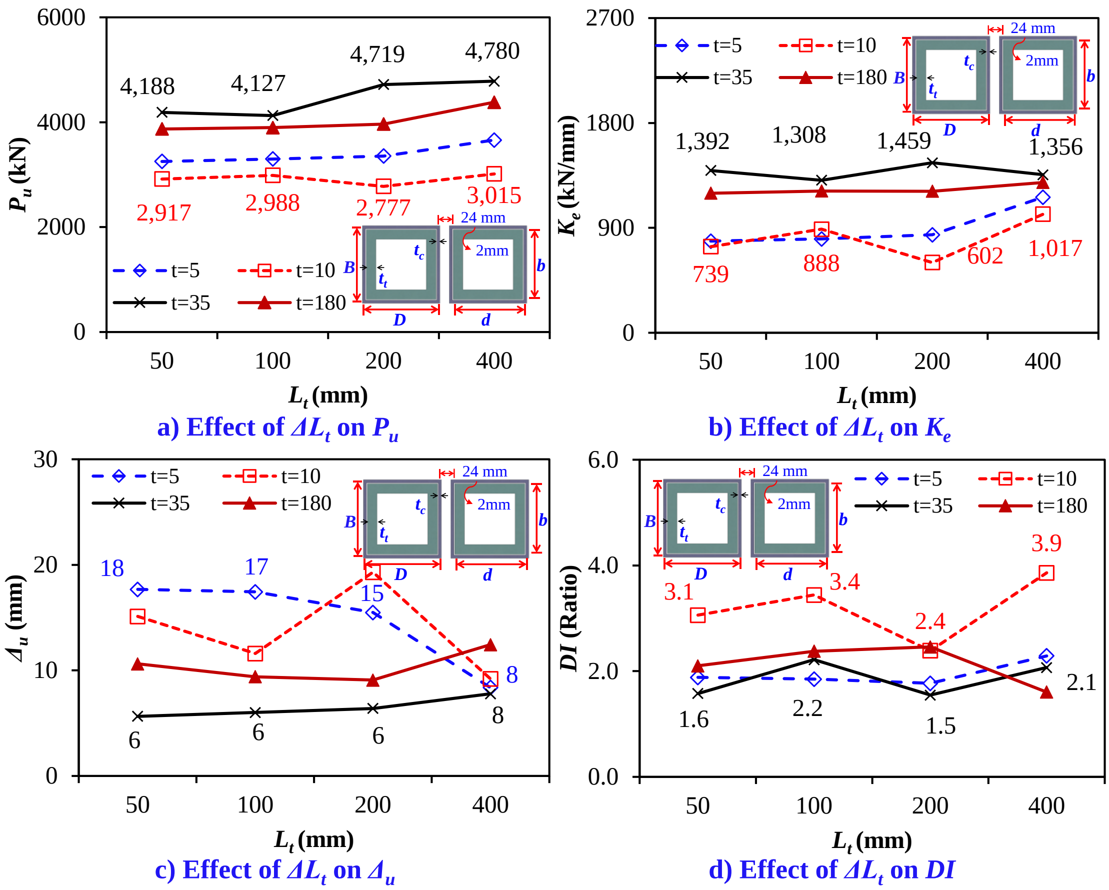

Fig. 22 Influence of ΔL_t

5.3.3 Shear keys length to width (d×b)

Figure 23(a-e) shows the impacts of d and b for L_t of 100, 150, and 250 mm. It reveals that P_u and K_e decrease linearly as the d and b values decrease since the spacing between the shear-key and tube expands from 0 to 4 and 6 mm, respectively. For L_t of 100, 150, and 250 mm, as d and b reduced from 184 to 176 and 172 mm, the P_u (or K_e) declined by 23% to 35% (36% to 39%), 26% to 34% (51% to 45%), and 22% to 30% (41% to 28%). Because decreasing d and b decreases the cross-section area and raises tube-key spacing; thus, the tube buckles elastically due to the weakening of composite action by tubes and shear keys. Furthermore, Δ_u rises by 84% to 71%, 170% to 113%, and 49% to 25% due to possible elastic buckling, which raises buckling strain and Δ_u. However, declines in d and b had a weaker relationship with DI. This is due to the varying amounts of shear stresses experienced by tubes during severe buckling.

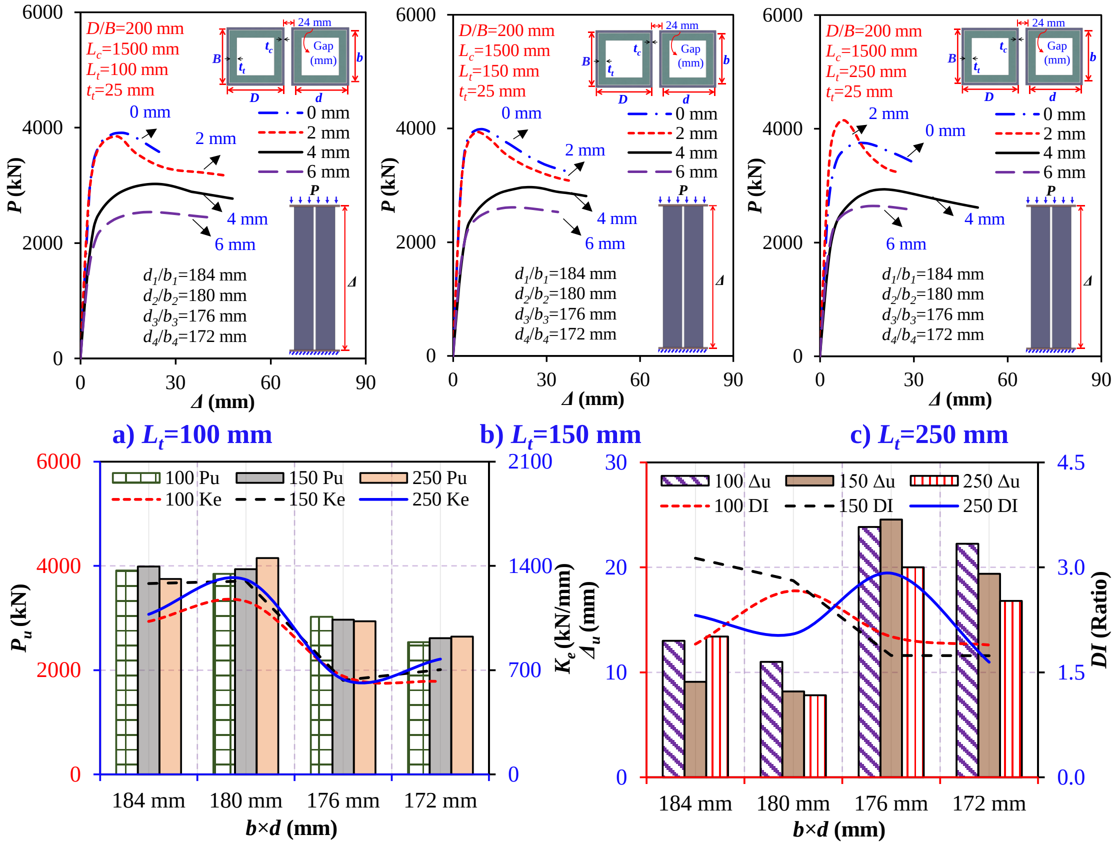

a) L_t=100 mm b) L_t=150 mm c) L_t=250 mm

d) Effect of $d \times b$ on P_u & K_e e) Effect of $d \times b$ on $\varDelta_u$ & DI

Fig. 23 Influence of $d \times b$

5.4 Influence of column

5.4.1 Column's height ($\varDelta L_c$)

Figure 24(a-d) shows the contribution of L_c to the P-$\varDelta$ curves. **Figure 25(a-d)** depicts its effect on the P_u, K_e, $\varDelta_u$, and DI ratios with varying L_t. It shows that increasing L_c has no significant effect on strength and ductility, i.e., P_u, $\varDelta_u$, and DI, while significantly reducing K_e in a linear declined pattern. With an increase in L_c from 1.0 to 1.5, 2.0, and 3.6 m, the K_e at 50 mm L_t decreases by 15%, 40%, and 58%, at 100 mm L_t by 27%, 31%, and 60%, at 200 mm L_t by 24%, 37%, and 60%, and at 400 mm L_t by 19%, 35%, and 57%. Reduced stiffness is because increasing L_c increase the slenderness ratio, making the column more prone to global buckling, crookedness, and P-δ or shearing effect. Moreover, boundary constraints become weaker with increased L_c.

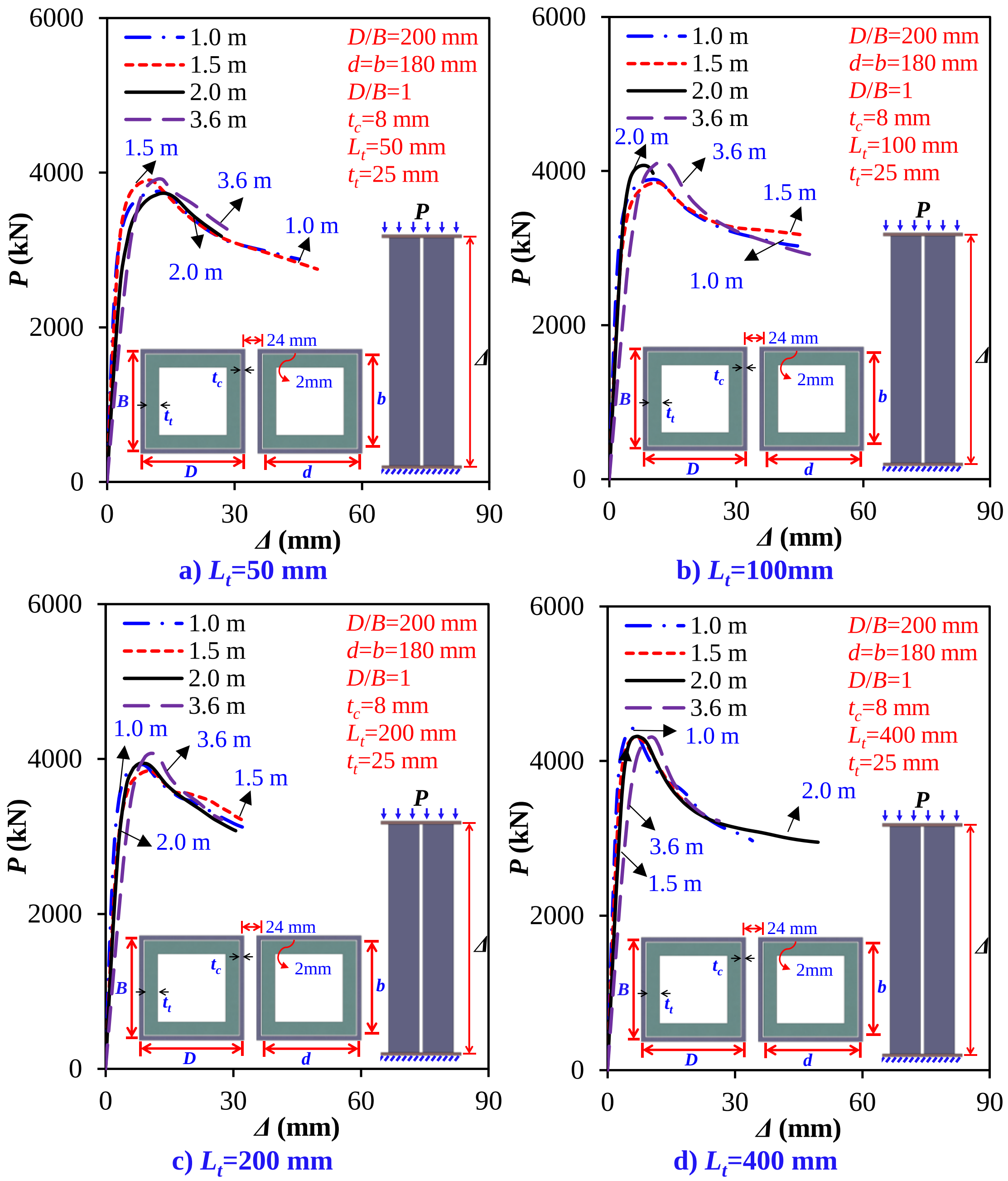

Fig. 24 Influence of the ΔL_c

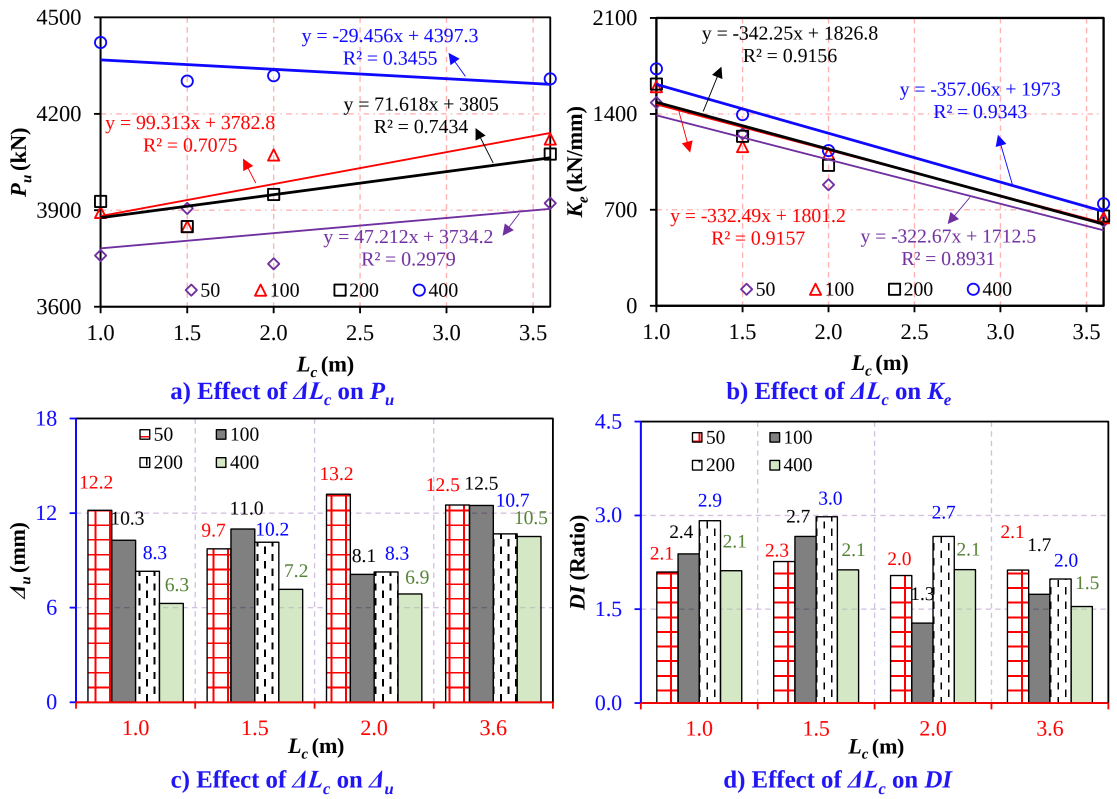

Fig. 25 Influence of the ΔL_c

5.4.2 Column's thickness (Δt_c)

The effects of t_c (5, 7, 8, and 9 mm) on the P-Δ curves are illustrated in **Fig. 26(a-c)**. **Figure 27(a-d)** plots t_c impact on the P_u, K_e, Δ_u, and DI ratios for L_t of 100, 150, and 250 mm. It demonstrates that P_u and K_e increased linearly as the t_c value increased. With an increase in t_c from 5 to 7, 8, and 9 mm, the P_u (or K_e) increased by 116%, 179%, and 209% (223%, 378%, and 374%) for L_t 100 mm, 102%, 162%, and 185% (92%, 217%, and 187%) for L_t 150 mm, 110%, 174%, and 198% (114%, 234%, and 223%) for L_t 250 mm. Simultaneously, Δ_u is fallen by 40%, 43%, and 26% for L_t 100 mm, and 22%, 44%, and 0% for L_t 250 mm. In comparison, DI is risen by 35%, 71%, and 57% for L_t 100 mm, and 30%, 7%, and 22% for L_t 250 mm. Increasing t_c decreases D/t_c, or L_c/r, improving buckling resistance and enhancing the tubes' strength, stiffness, and post-buckling ductility. Furthermore, as t_c increases from 5 to 9 mm, D/t_c decreases from 40 to 22, resulting in a change from Class 4 to Class 1 cross-section.

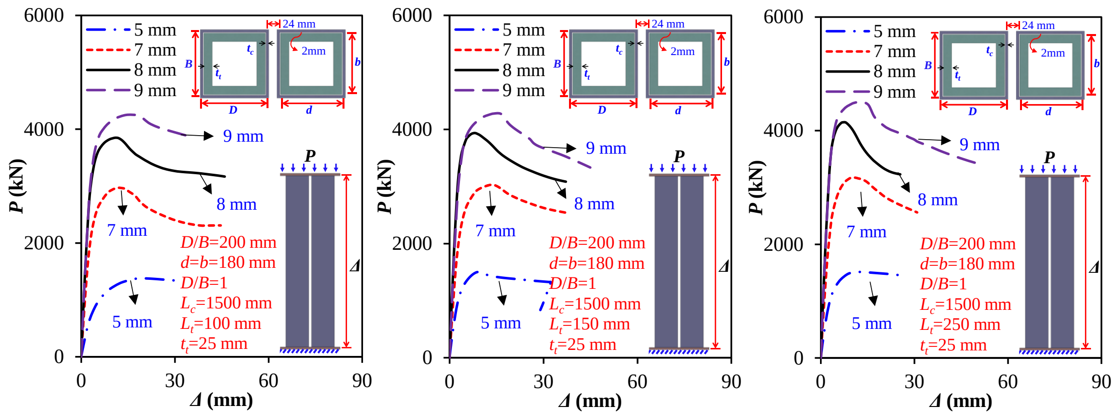

a) L_t=100 mm b) L_t=150 mm c) L_t=250 mm

Fig. 26 Influence of Δt_c

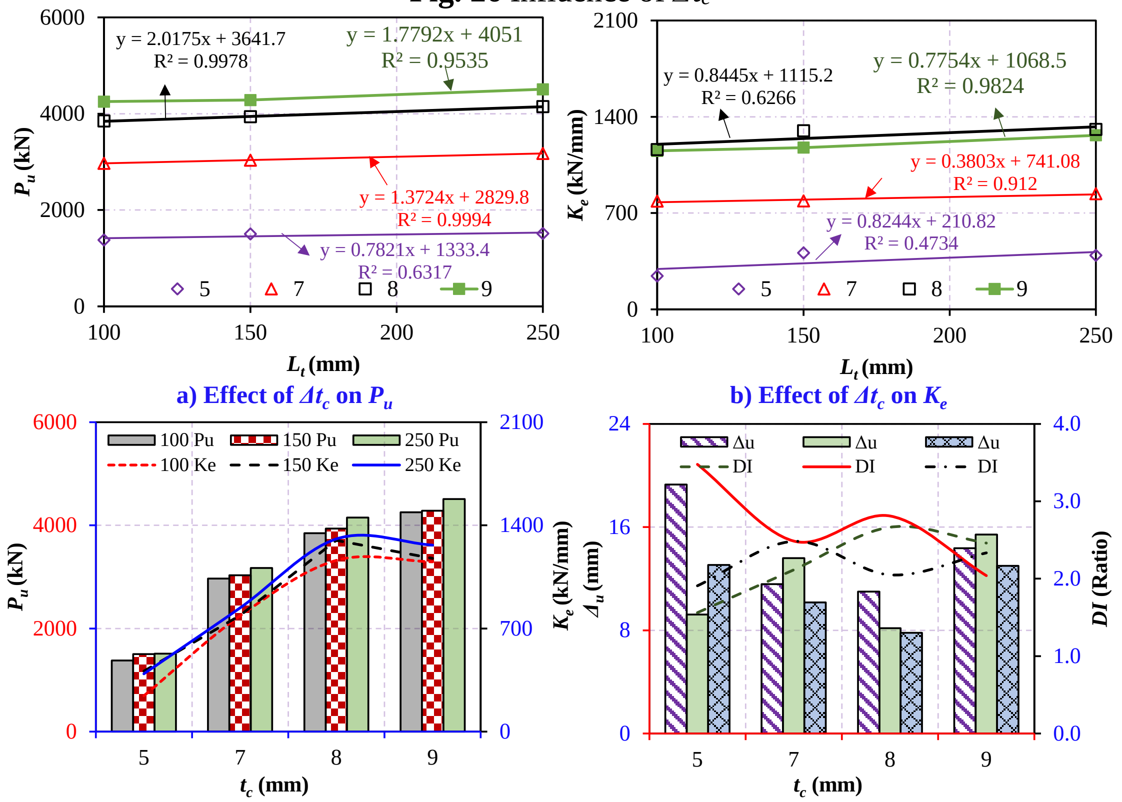

a) Effect of Δt_c on P_u b) Effect of Δt_c on K_e

c) Effect of Δt_c on Δ_u d) Effect of Δt_c on DI

Fig. 27 Influence of Δt_c

5.4.3 Column length to width (D×B)

The effect of changing tubes *D* and *B* (150, 180, and 250 mm) with L_t of 100, 150, and 250 mm is shown in **Fig. 28(a-e)**. It illustrates that P_u and K_e increased linearly as the *D* and *B* values increased. The P_u (or K_e) increased by 4% to 10% (9% to 27%), 8% to 12% (23% to 27%), and 2% to 5% (10% to 27%) for L_t 100, 150, and 250 mm as *D* and *B* increased from 150 to 180 and 250 mm. Simultaneously, Δ_u showed a decrement of 20% to 42%, and 10% as *D* and *B* increased from 150 to 250 mm for L_t 100, 150, and

250 mm due to the enhancement of yield strain and leading to the plastic buckling as per test findings. However, *D* and *B* showed a weak impact on *DI*, increasing by 6% to 86% and reducing by 9% to 1%, as *D* and *B* increased from 150 to 180 and 250 mm for L_t 100 and 250 mm. This is because increasing *D* and *B* increases cross-section area, improving compression behavior. It is worth noting that increasing *D/B* from 150 to 180 and 250 mm with a t_c of 8 mm causes D/t_c to increase from 18 to 22 and 31, resulting in a change in cross-section class.

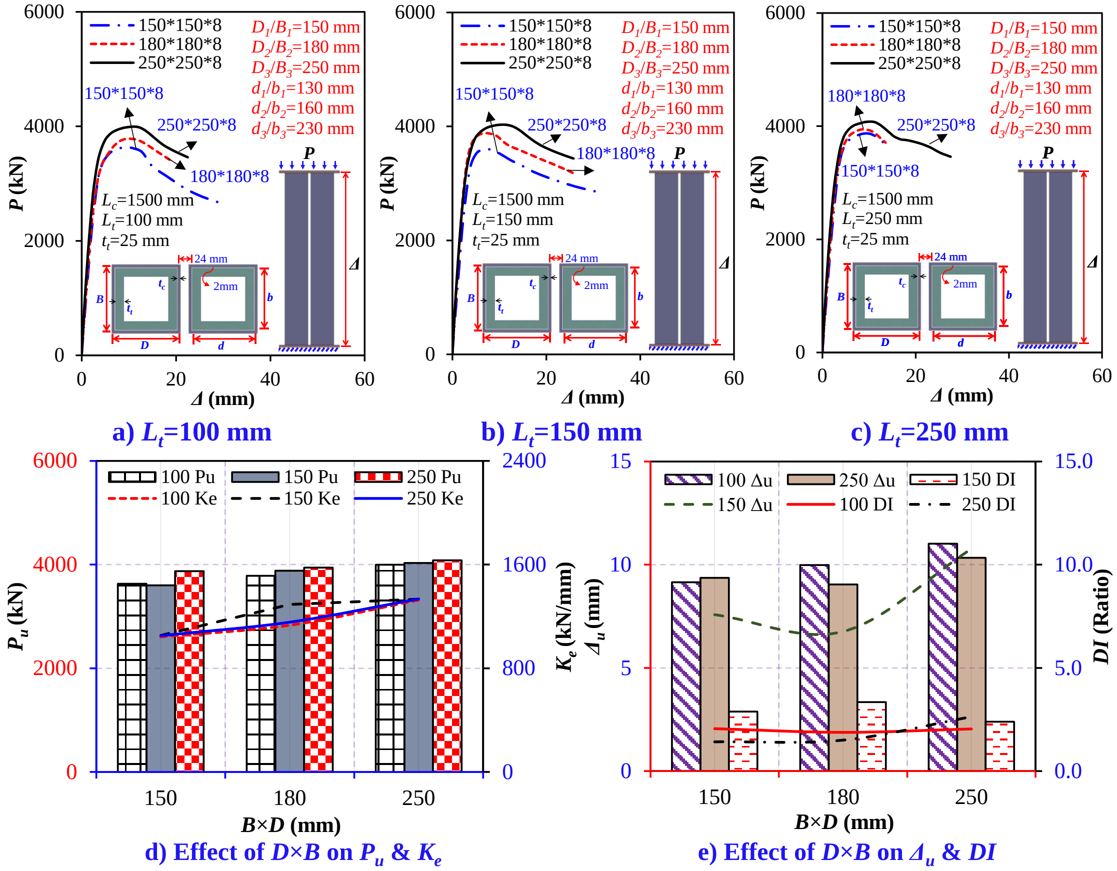

Fig. 28 Influence of $D \times B$

5.4.4 Columns spacing

Figure 29(a-c) shows the *P-Δ* curves, highlighting the column spacing effect between adjacent tubes with L_t of 100, 150, and 250 mm. The impact of increasing spacing on the P_u, K_e, $Δ_u$, and *DI* ratios is depicted in **Fig. 30(a-d)**. It shows that as the spacing raised from 0 to 6, 24, and 36 mm, P_u, K_e, and *DI* improved linearly. P_u (K_e and *DI*) grows by 4% (24% and 52%) to 3% (18% and 84%), and 8% (41% and 3%), 4% (23% and 5%) to 4% (31% and 83%), and 3% (29% and 64%), and 8% (26% and 46%) to 7% (26% and 36%), and 6% (19% and 17%) as spacing raises from 0 to 6, 24, and 36 mm. Simultaneously, for L_t of 100 (150 and 250) mm, Δ_u falls by 38% (28% and 42%), 34% (44% and 40%), and 55% (44% and 31%). Increasing column spacings minimizes the mutual weakening of adjacent tubes and shifts failure behavior from symmetrical to unsymmetrical, boosting buckling resistance, strength, stiffness, and post-buckling ductility. However, when stiffness increases, ductility falls due to bending stresses and a reduction in buckling strain since each tube works independently.

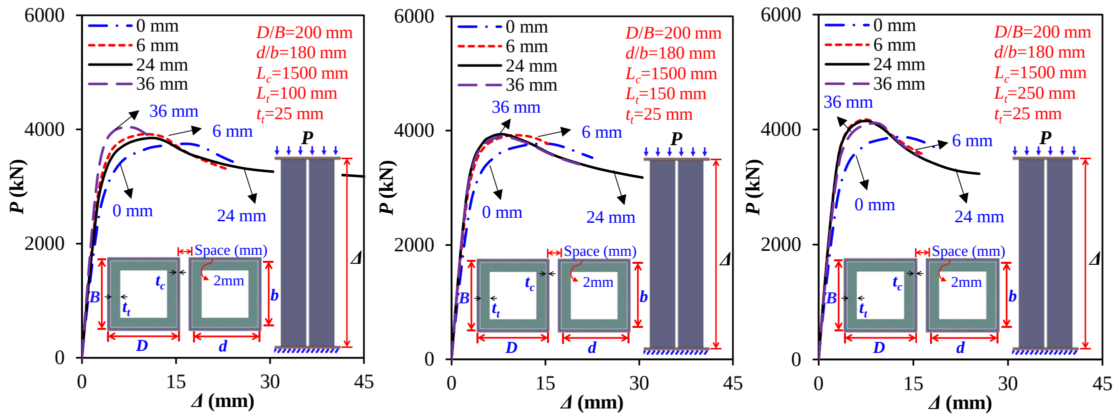

a) L_t=100 mm b) L_t=150 mm c) L_t=250 mm

Fig. 29 Influence of neighboring columns spacing

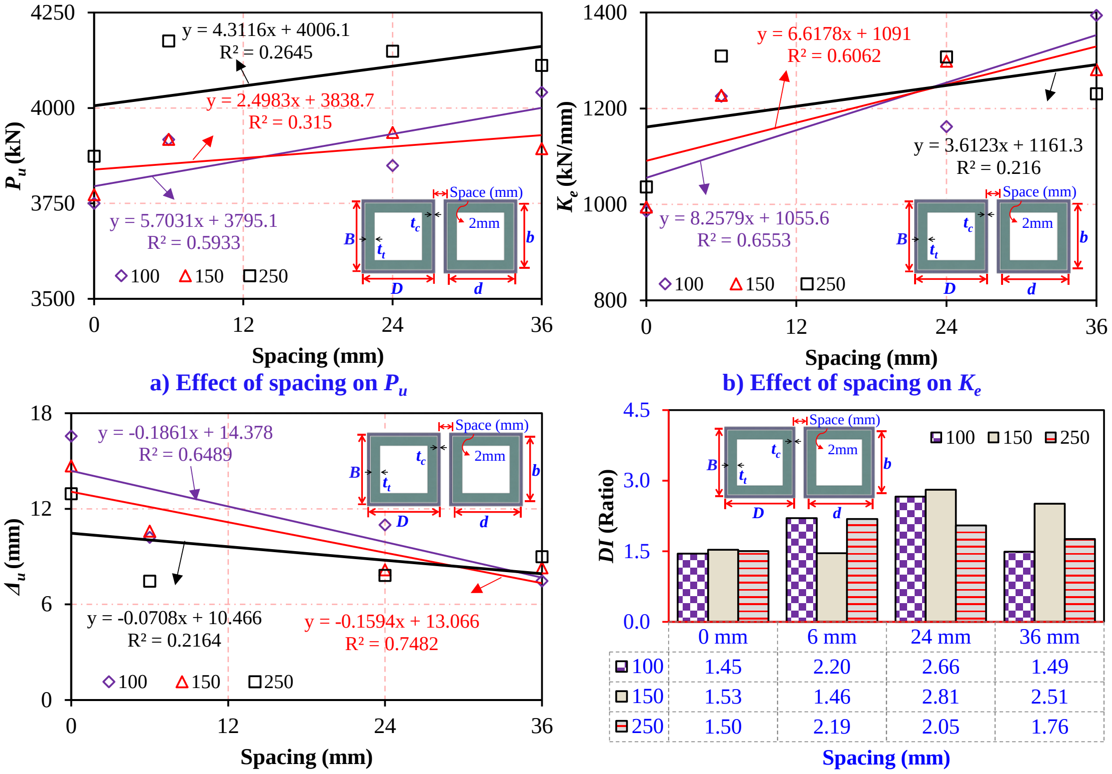

	0 mm	6 mm	24 mm	36 mm
100	1.45	2.20	2.66	1.49
150	1.53	1.46	2.81	2.51
250	1.50	2.19	2.05	1.76

a) Effect of spacing on P_u b) Effect of spacing on K_e

c) Effect of spacing on Δ_u d) Effect of spacing on *DI* ratio

Fig. 30 Influence of columns spacing

5.4.5 Columns quantity

Figure 31(a-e) depicts the *P-Δ* curves and scatters of the P_u, K_e, Δ_u, and *DI* ratios, emphasizing the columns number effect with L_t of 100, 150, and 250 mm. **Figure 32(a-c)** demonstrates the impact on the failure modes. P_u and K_e improved linearly as the column number increased from 1 to 2, 3, and 4. P_u (K_e) increases by 113% (59%) to 236% (179%), and 342% (261%), 118% (77%) to 243% (197%), and 347% (286%), and 117% (66%) to 241% (208%), and 357% (292%). Simultaneously, the relationship between Δ_u and *DI* is weaker. Furthermore, the rise of the P_u by 2.1, 3.4, and 4.4 times, and the K_e by 1.6, 2.8, and 3.6 times confirms that increasing the number of columns increases the cumulative cross-section area, which improves compression behavior. A rise of more than 2, 3, and 4 times from individual to grouped columns confirms the favorable influence of grouped tubes. Besides, increasing the column number transfers failure from the tube's mid-height to the shear-key edges, supporting the controlling function of shear keys.

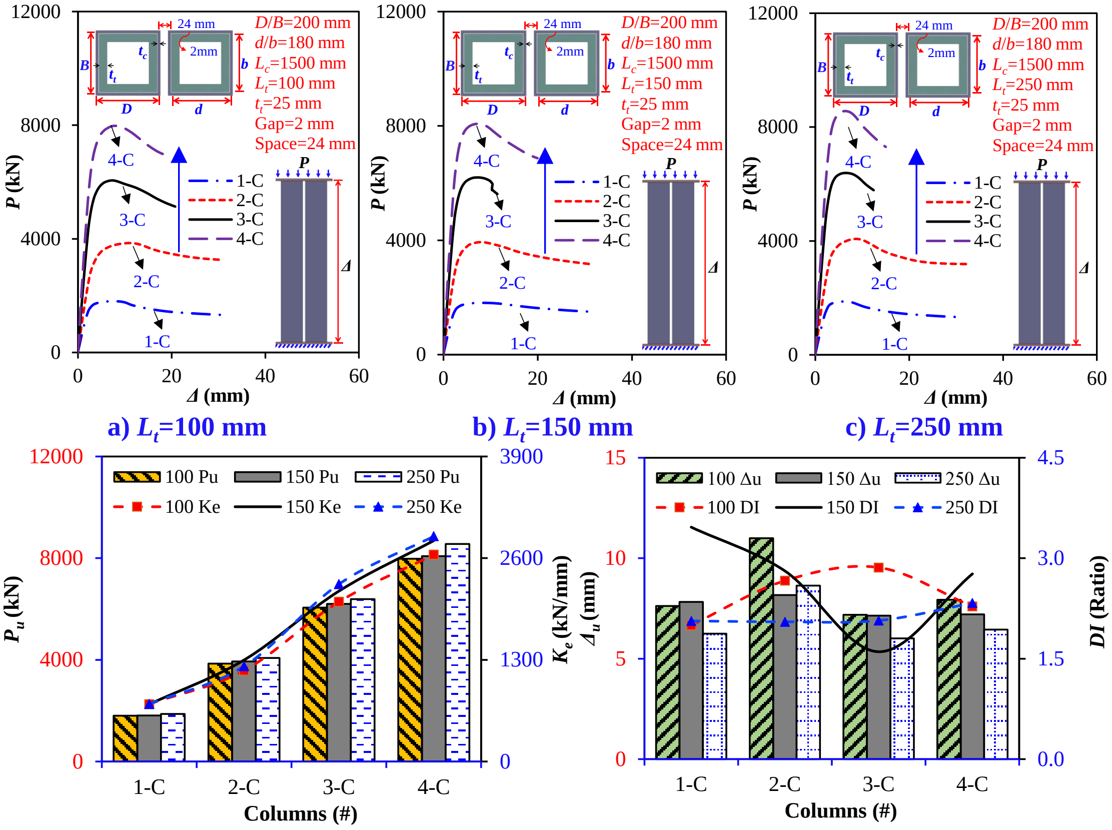

a) L_t=100 mm b) L_t=150 mm c) L_t=250 mm

d) Effect on P_u & K_e e) Effect on Δ_u & DI

Fig. 31 Influence of columns number

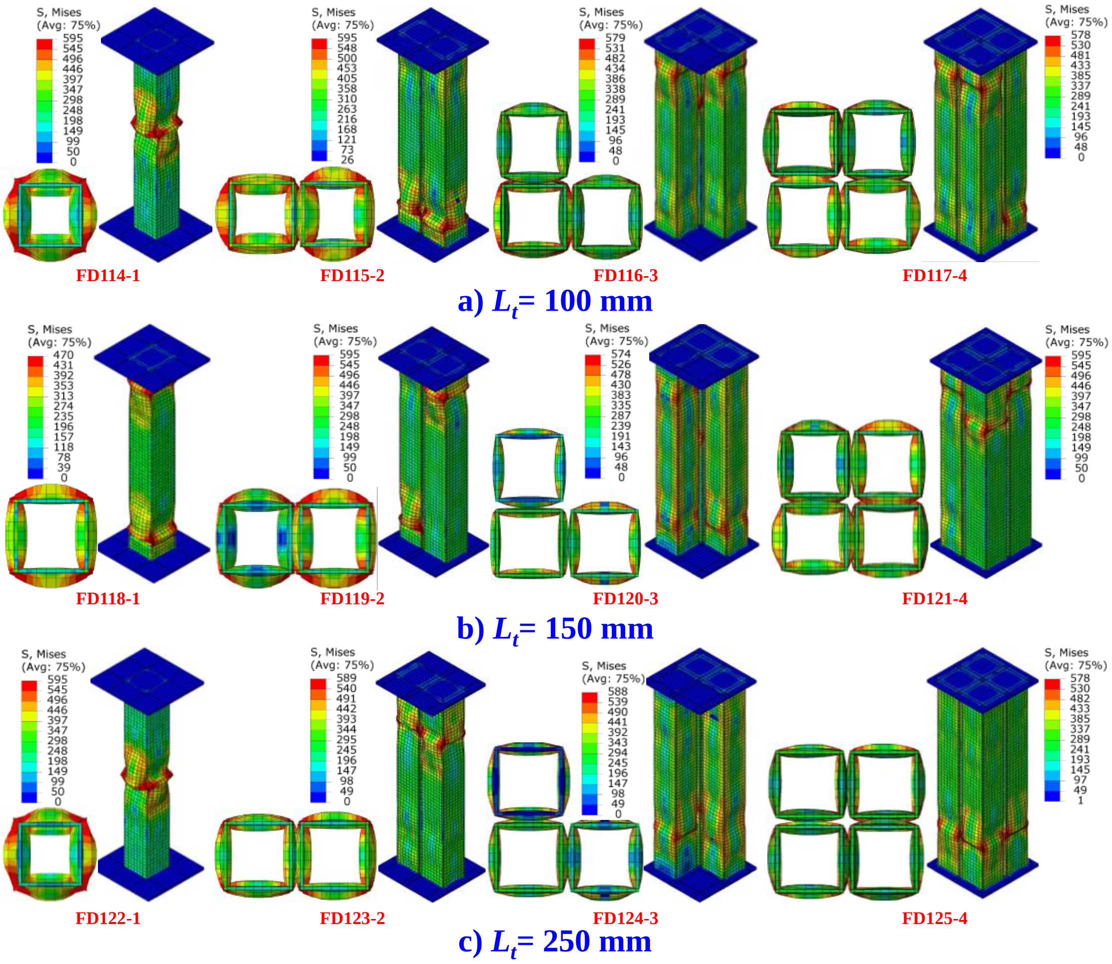

Fig. 32 Influence of columns number

5.5 Influence of connecting plate thickness

The impact of connecting plate thickness is depicted in **Fig. 33**, revealing increases in connecting plate thickness from 15 to 20 and 30 mm had a minor impact on P_u (K_e), with a 1% (3%) to 3% (7%) increase observed for L_t of 150 mm. Simultaneously, there is a lesser association with Δ_u, but there is an increase in DI, such as 21% to 7%, 44% to 1%, and 8% to 6% for L_t of 100, 150, and 250 mm. Because Class 1 members suffer local buckling, connecting plates play a smaller influence in the tube's compression behavior in pure axial compression. However, the recession stage is accelerated because plates provide some resistance after severe buckling.

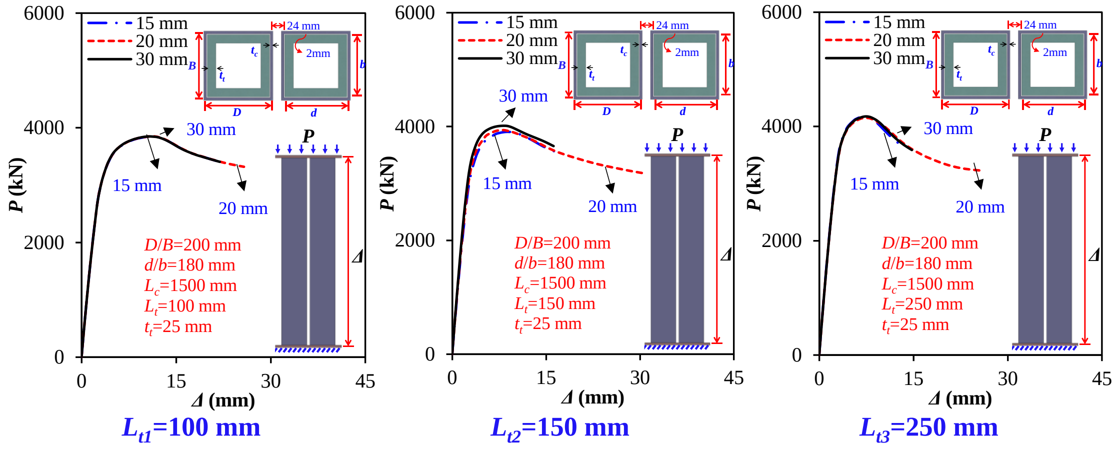

Fig. 33 Influence of friction and connecting plate

6 Analytical studies on shear-keyed grouped columns

The shear-keyed tube failure mechanism discovered an S-shaped pattern with local inward and outward buckling demonstrating elastic and plastic failure. It implies that elastic buckling causes normalized cross-sectional and member strength of tubes to decline. Moreover, whether inelastic or elastic, local buckling influences the cross-sectional and member capacity [62]. Additionally, the non-conservativeness of the EC3 cross-sectional resistance is more than the member resistance design with stability coefficients. Therefore, conservative designs take the stability coefficients, radius of gyration, and elastic buckling stress into account [62]. Likewise, member global strength rather than cross-sectional strength produces more conservative results in such situations [14]. Similarly, as in Refs. [80,81], yield strength failure with local buckling of tubes adopted members' global strength equations for design. Moreover, fixed-ended stubs used local buckling reduction factors [89]. Furthermore, the member buckling strength was the primary design strength criterion used in Ref. [90]. Simply-supported concentrically compressed steel members also used the global strength model [88]. This indicates that the global strength prediction methodology with tube stability coefficients is a well-known elastic and plastic design method. In order to obtain a buckling resistance more conservatively than a cross-section strength design, the design approaches used the column's global strength stability coefficient to account for local elastic and plastic buckling of shear-keyed grouped tubes.

6.1 Yielding strength

Figure 34(a,b) shows the normalized scatter P_u/f_yA and $P_u/\chi f_yA$ to determine the compression yielding or elastic buckling [91]. The term P_u represents the compression resistance listed in **supplementary Table A1**. EC3:1-1 classifies cross-sections, recommending plastic buckling beyond yield for Class 3, and elastic buckling before yield for Class 4. Therefore, P_u/f_yA *or* $P_u/\chi f_yA$<1 for $D/t\varepsilon \leq 42$ of Class 3 limit was considered non-conservative due to the yielding incapability, while P_u/f_yA *or* $P_u/\chi f_yA$>1 was deemed as conservative due to the full-yielding. Moreover, P_u/f_yA *or* $P_u/\chi f_yA$<1 for $D/t\varepsilon > 42$ of the Class 4 limit was considered conservative, not able to achieve yielding, while P_u/f_yA *or* $P_u/\chi f_yA$ >1 as non-conservative, implying to undergo yielding. It demonstrates that P_u/f_yA *or* $P_u/\chi f_yA$<1.0, indicating the EC3:1-1 Class 3 limit is non-conservative except for two samples. For the Class 4 section, the results were conservative, validating the existence of elastic buckling. This is infinitesimally consistent with the test findings. Shear-keyed tubes have a lower nominal capacity, making full-yielding harder. This necessitates updating classification limits for non-slender sections in EC3 to ensure a safer design.

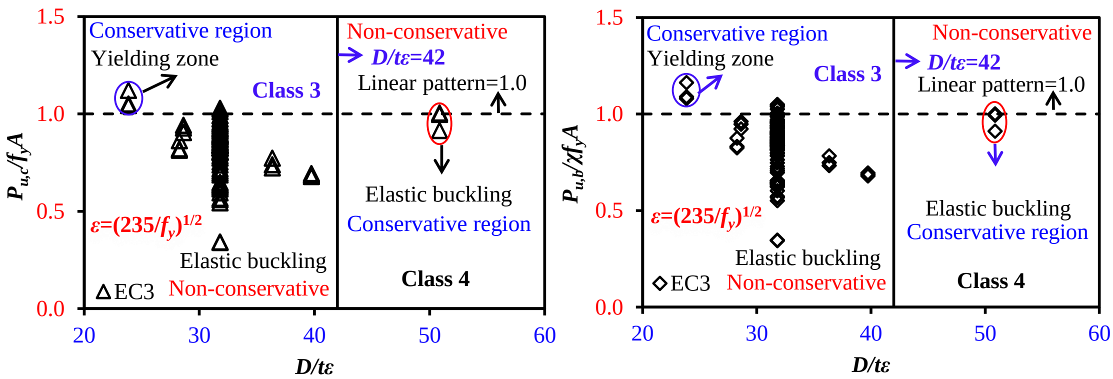

a) Normalized compressive resistance   b) Normalized buckling resistance

Fig. 34 Normalized resistances of shear-keyed grouped tubes

6.2 Code equations on ultimate strength

In EC3:1-1 [91], shear-keyed grouped tubes are designed as follows:

$$P_{u,c} = f_y A_s(\text{or}A_{eff})\,/\gamma_{M0}\ ;\ P_{u,b} = \chi f_y A_s(\text{or}A_{eff})\,/\gamma_{M0} \tag{5}$$

$$A_{eff} = A_s - 2t\rho_f d - 2t\rho_w b \tag{6}$$

where γ_{M0} represent modified safety factors. The code [92,93], standards [94], statistical studies [95], and research [14–16] recommended it 1.0. Since the study reveals overestimations of 127 and 124 outcomes for $P_{u,c}$ and $P_{u,b}$ with γ_{M0} as 1.0, it recommends 2.0 for shear-keyed grouped columns to achieve conservativeness of 100%. The factor χ is obtained as:

$$\chi = 1/[\phi + (\phi^2 - \bar{\lambda}^2)^{0.5}] \le 1 \tag{7}$$

$$\phi = 0.5\left[1 + \alpha\left(\bar{\lambda} - 0.2\right) + \bar{\lambda}^2\right];\ \bar{\lambda} = \sqrt{f_y A_s/P_{cr}} \tag{8}$$

$$\rho_f(\rho_w) = \begin{cases} 1.0, & \lambda_f(\lambda_w) \le 0.673 \\ \dfrac{\lambda_f(\lambda_w) - 0.055(3+\psi)}{{\lambda_f}^2({\lambda_w}^2)} \le 1.0, & \lambda_f(\lambda_w) > 0.673 \end{cases} \tag{9}$$

$$\lambda_f(\lambda_w) = \sqrt{\frac{f_y}{\sigma_{cr}}} = \frac{d/t(b/t)}{28.4\varepsilon\sqrt{k_\sigma}} \tag{10}$$

where ϕ, ρ_f, ρ_w, $\psi = \frac{\sigma_{min}}{\sigma_{max}}$, and k_σ represent the imperfection, reduction, stress, and buckling factors in code Tables 4.1, 4.2, 6.1, and 6.2.

CSA S16-19 [96] calculates the member's capacity as follows:

$$C_r = \varphi A F_y(1 + \lambda^{2n})^{-\frac{1}{n}}\,;\lambda = \sqrt{\frac{F_y}{F_e}}\ ;F_e = \pi^2 E/\left({}^{KL}/_{r}\right)^2 \tag{11}$$

where n is 1.34 for hot-rolled. The code suggests safety factors φ of 0.9 overestimates 86 outcomes; the study recommends $\varphi = 0.5$, improving prediction underestimations by 100%.

AISC360-16 [97] predicts the strength as follows:

$$P_u = f_c A_s(A_{eff}) \tag{12}$$

$$f_c = \begin{cases} Q\left[0.658^{Qf_y/f_e}\right]f_y\,, & if\ \ Qf_y/f_e \le 2.25 \\ 0.877 f_e, & if\ \ Qf_y/f_e > 2.25 \end{cases}\ ;\ f_e = \pi^2 E_s/({}^{KL}/_{r})^2 \tag{13}$$

where f_e and Q represent the buckling stress and net reduction factor [98]:

$$Q = \{1.0 \quad \text{if} \ \ d/t \le 1.40\sqrt{E_s/f_y} \ \ \text{(NS)} \tag{14}$$

$$Q = \{Q_a Q_s \text{ if } d/t > 1.40\sqrt{E_s/f_y} \text{ (S)}; A_{eff} = A_s - 2t(b-b_e) - 2t(d-d_e) \tag{15}$$

$$Q = Q_a(Q_S = 1);\text{ and } Q_a = A_{eff}/A_s \text{ (AISC Eqn-7)} \tag{16}$$

$$b_e = 1.92t\sqrt{E_s/f_y}\left[1 - \frac{0.34}{(b/t)}\sqrt{Es/f_y}\right] \le b, if\ {}^{b}/_{t} \ge 1.49\sqrt{\frac{E_s}{f_y}}, otheriwse = b \tag{17}$$

$$d_e = 1.92t\sqrt{E_s/f_y}\left[1 - \frac{0.38}{(d/t)}\sqrt{E_s/f_y}\right] \le d, if\ {}^{d}/_{t} \ge 1.40\sqrt{\frac{E_s}{f_y}}, otherwise = d \tag{18}$$

where b or d can be taken as *B*/*D*-2*t*, and Q_s and Q_a denote the reduction factors for slender unstiffened, and stiffened elements [98]; b_e and d_e denote the effective length and width. Since reduction factors $Q = 1.0$ or $Q = Q_a Q_s$ overestimates 122 outcomes, the study recommends $Q = 0.5$ for both slender and non-slender shear-keyed columns to achieve conservativeness of 100%.

GB 50017-2017 [69] specifies member compressive resistance as follows:

$$P_u = \varphi f_y A_s;\ \varphi = \begin{cases} 1 - \alpha_1 {\lambda_n}^2, & if\ \lambda_n \le 0.215 \\ \frac{1}{2{\lambda_n}^2}[K - \sqrt{K^2 - 4{\lambda_n}^2}, & if\ \lambda_n > 0.215 \end{cases} \tag{19}$$

$$K = \left(\alpha_2 + \alpha_3\lambda_n + {\lambda_n}^2\right);\ \lambda_n = \frac{\lambda}{\pi}\sqrt{f_y/E_s} \tag{20}$$

$$\text{Type } B = \begin{cases} \alpha_1 = 0.650 \\ \alpha_2 = 0.965 \\ \alpha_3 = 0.300 \end{cases};\ \text{Type } C = \begin{cases} \alpha_1 = 0.730, & \lambda_n \le 1.05 \\ \alpha_2 = 0.906, & \lambda_n \le 1.05 \\ \alpha_3 = 0.595, & \lambda_n \le 1.05 \\ & \text{or} \\ \alpha_1 = 0.730, & \lambda_n > 1.05 \\ \alpha_2 = 1.216, & \lambda_n > 1.05 \\ \alpha_3 = 0.302, & \lambda_n > 1.05 \end{cases} \tag{21}$$

where φ is the safety factor. Since safety factors values $\alpha_1 = 0.650;\ \alpha_2 = 0.965;\ \alpha_3 = 0.300$ overestimate 120 outcomes; the study recommends $\alpha_1 = 15.965;\ \alpha_2 = 1.80;\ \alpha_3 = 1.65$ for shear-keyed grouped members, improving prediction underestimations by 100%.

6.2.1 Reliability analysis

The reliability of modified predictions was validated by examining P_u of 133 shear-keyed grouped tubes listed in **supplementary Table A1**. **Figure 35** compares the findings with non-modified equations. It reveals that the average (Covs) analysis-to-prediction ratios provided by EC3-C, EC3-B, CSA S16, AISC360-16, and GB50017-2017 are 0.84(0.12), 0.85(0.13), 0.95(0.15), 0.86(0.13), and 0.87(0.15), respectively. It demonstrates that codes provide non-conservative estimates with 127/124 over- and 6/9 under-estimations for EC3-C/EC-B, 86 over- and 47 under-estimations for CSA S16, 122 over- and 11 under-estimations for AISC360-16, and 120 over- and 13 under-estimations for GB50017. Few slender or tube-shear keys large gap FEM produced conservative outcomes due to strength underestimation. Furthermore, CSA S16 was the most conservative, whereas EC3:1-1 had the most non-conservative outcomes. The outcomes of modified prediction equations are compared in **Fig. 36**. EC3-C, EC3-B, CSA S16, AISC360-16, and GB50017-2017 have average (Covs) analysis-to-prediction ratios of 1.61(0.14), 1.63(0.14), 1.73(0.12), 1.69(0.13), and 1.88(0.16), respectively. The average>1.0 confirms that modified equations generated conservative estimates, with 133 underestimations and 0 overestimations for EC3-C, EC-B, CSA S16, AISC360-16, and GB50017, respectively.

As previously stated, the cross-sectional slenderness limits for accumulating shear-keyed grouped tubular columns should be revised. The modified code equations enhanced the conservativism for EC3-C, EC3-B, CSA S16, AISC360-16, and GB50017-2017 of P_u from 5%, 7%, 35%, 8%, and 10% to 100% for 133 models of shear-keyed grouped tube columns.

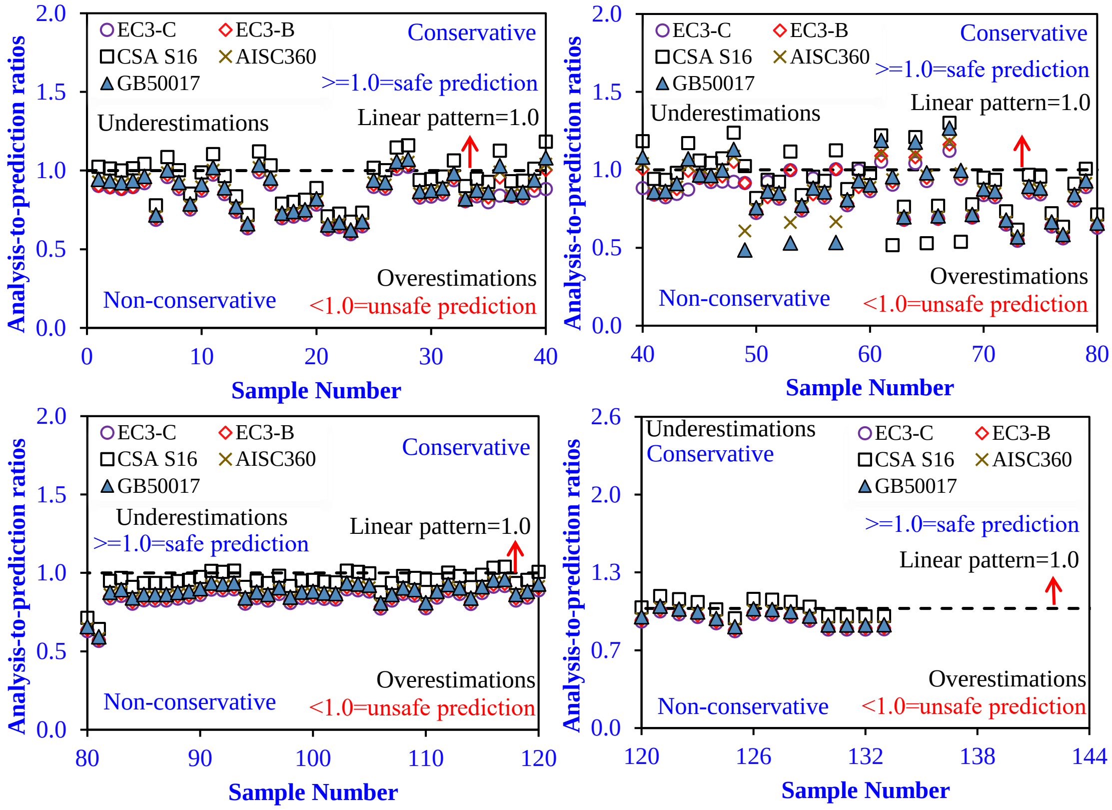

Specimen	1-40		40-80		80-120		120-133		Total	
	Mean	Cov	Mean	Cov	Mean	Cov	Mean	Cov	Mean	Cov
○ EC3-C	0.83	0.13	0.84	0.16	0.84	0.08	0.89	0.07	0.84	0.12
◇ EC3-B	0.84	0.14	0.86	0.17	0.85	0.08	0.90	0.07	0.85	0.13
□ CSA S16	0.95	0.14	0.93	0.21	0.95	0.08	1.01	0.07	0.95	0.15
✖ AISC360	0.86	0.14	0.85	0.18	0.86	0.08	0.91	0.07	0.86	0.13
△ GB50017	0.87	0.14	0.86	0.22	0.87	0.08	0.93	0.07	0.87	0.15

Fig. 35 Non-modified equations outcomes

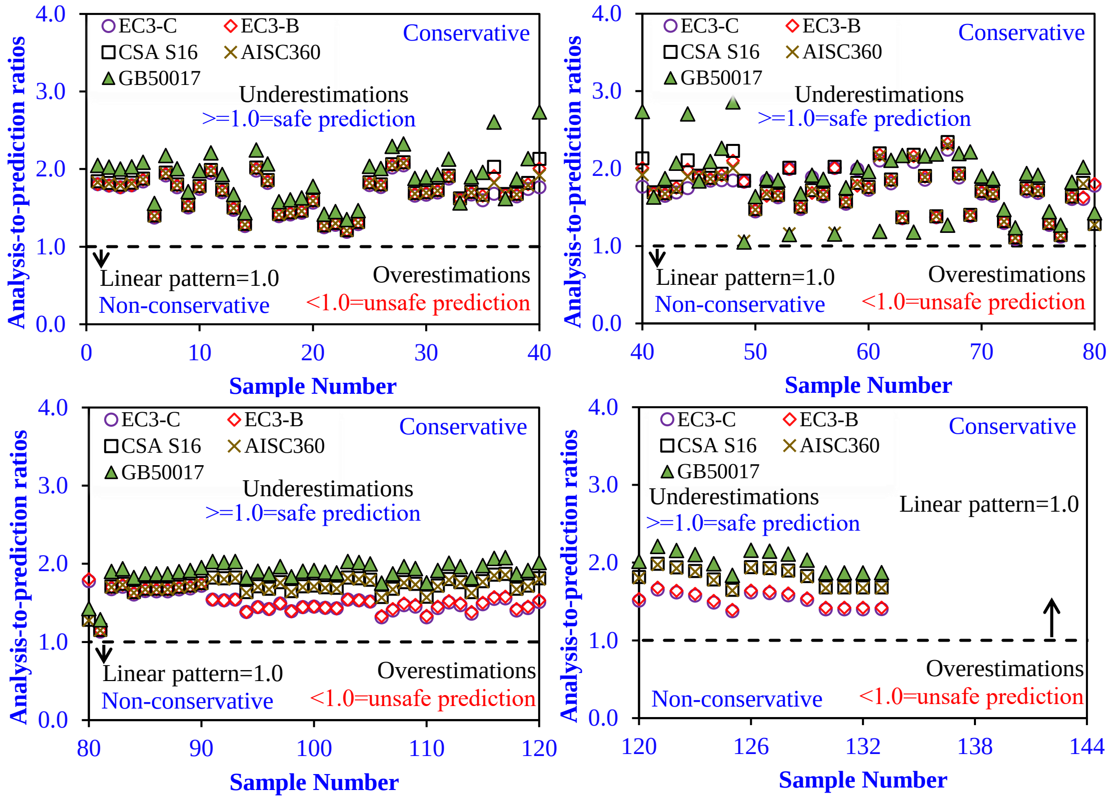

Specimen	1-40		40-80		80-120		120-133		Total	
	Mean	Cov	Mean	Cov	Mean	Cov	Mean	Cov	Mean	Cov
○ EC3-C	1.66	0.13	1.70	0.15	1.50	0.09	1.51	0.07	1.61	0.14
◇ EC3-B	1.69	0.14	1.72	0.16	1.52	0.09	1.53	0.07	1.63	0.14
□ CSA S16	1.71	0.14	1.73	0.17	1.71	0.08	1.81	0.07	1.73	0.12
✖ AISC360	1.69	0.14	1.65	0.18	1.70	0.08	1.80	0.07	1.69	0.13
△ GB50017	1.91	0.17	1.83	0.24	1.90	0.08	2.02	0.07	1.88	0.16

Fig. 36 Modified equations outcomes

The primary application of the design approaches is to evaluate the axial compression resistance of MSB's non-welded steel shear-keyed grouped tubular columns with fixed-fixed boundary conditions with and without the key-to-tube gap in an averagely conservative manner. Class 1 to 4 steel hot-rolled cross-sectioned columns may be designed with the hot-rolled hollow box or solid-shaped non-welded shear keys without threads, grouting, and concrete composite infill. Shear-keyed tubes with welded [99] or bolted [100] shear keys on the ends may affect uplift, failure, and compressive response; hence, design procedures cannot be applied directly to them and would need further investigation.

7 Conclusions

This study evaluated the axial compression behavior of shear-keyed grouped tubular columns. Four large-scale tests were conducted to assess their structural and failure response. Meanwhile, FEA was created for parametric investigations. Using four code prediction equations, modified predictions were developed for evaluating compression resistances. The following are the outcomes of these studies:

1. Shear-keyed grouped tubes *P-Δ* curves displayed linear elastic, nonlinear, and recession zones. With less ductility and a shorter recession zone, tubes with thicker but shorter shear keys exhibited lower yield strength and initial stiffness but greater ultimate resistance. Thin shear keys were associated with longer elastic and recession zones, better yield, and poorer ultimate strength with improved pre- and post-ultimate ductility. Conversely, the welded grouped column had the highest stiffness, yield, ultimate strength, and the greatest ductility and recession. Local inward or outward buckling occurs when tubes attain their maximum compressive strength. A recession eventually leads to a loss in capacity and an increase in local buckling.
2. Shear-keyed grouped tubes failed differently from directly welded tubes, with inward buckling followed by outward buckling, producing an S-shaped pattern. Buckling can be symmetrical or asymmetrical, with bulged-out regions on adjacent columns' interior sides, resulting in tube contact and double S-shaped buckling. All specimens failed to owe local inward and outward buckling at shear keys, column mid-height, or between 1/4 and 1/2 tube height. Contrarily, fully welded columns exhibited one type of symmetrical local buckling on all sides of the columns on loading ends. On the interior faces, inward buckling

prevents tubes from touching. However, tube failures were identical on opposing sides but opposite on the adjacent faces of tubes.

3. Shear-keyed and fully-welded grouped tube strain curves showed linear, nonlinear, and recession phases. Numerous tube regions did not yield and buckled elastically. The S-shaped sinusoidal local buckling failure mode exhibited identical elastic and plastic local buckling on opposite sides and opposite on neighboring sides. Increasing the shear key's thickness and length shifted elastic buckling to plastic. However, all sections in fully-welded tubes yielded and displayed local plastic buckling.
4. Increasing t_t, L_t, t_c, D, B, d, b, columns spacing, and number increases grouped tubes P_u and K_e in a linear pattern; however, their effect on Δ_u and DI seemed significantly variable. Moreover, increasing L_c or L_c/r did not influence P_u but considerably decreased K_e and Δ_u in a linearly declining pattern. Reducing d and b increases the tube-key gap and decreases P_u, K_e, and DI while increasing Δ_u. Contrary, increases in connecting plate thickness have minor effects on P_u and K_e of 1%. Furthermore, increasing the column from 1 to 4 increases the P_u by 2.1, 3.4, and 4.4 times and the K_e by 1.6, 2.8, and 3.6 times, confirming the beneficial influence of shear-keyed grouped tubes.
5. Because the EC3 Class 3 limit prevents elastic buckling, the predicted nominal capacity of shear-keyed grouped tubes with and without buckling length decreases dramatically, making it difficult for similar non-slender cross-sections to yield fully and rendering the EC3 Class 3 slenderness limit non-conservative. Because the Class 4 limit prevents yielding before elastic buckling, a conservative design requires an update to Class 3.

6. The FEM accurately simulated shear-keyed grouped tube compression behavior by producing average minor prediction errors of 1.8% for P_u and 8.6% for Δ_u and a slight substantial scatter of 20.9% and 22.4% for K_e and DI. P_u and K_e increased linearly as the mesh size increased from 10 to 18, 25, and 35 mm, while Δ_u or DI decreased significantly. P_u and K_e decreased when initial imperfection increased from t/100 to t/10, t/5, t/2, and t and L/2000 to L/15000, L/1000, and L/500. Furthermore, raising t/100 to t and L/2000 to L/500 increased Δ_u, respectively. Failure modes of various mesh densities were inconsistent and varied in location, but initial imperfection did not affect failure modes. As determined by FE and testing, type C mesh and the design value of 7/8t or 7L/1500 imperfection amplitude adequately anticipated shear-keyed grouped tube compression behavior.
7. The predicted P_u values of 133 shear-keyed tube models using the EC3-C, EC-B, CSA S16, AISC360-16, and GB50017 equations were non-conservative, with around 127 overestimations for EC3-C, 124 for EC-B, 86 for CSA S16, 122 for AISC360-16, and 120 for GB50017. The modified code equations increased the number of conservative and safe estimates for EC3-C, EC3-B, CSA S16, AISC360-16, and GB50017-2017 to 133, attaining 100% conservatism.

Acknowledgment

The authors thank the National Natural Science Foundation of China (Grant No. 51978457 and 52008292) for their research grants.

References

[1] M. Alembagheri, P. Sharafi, R. Hajirezaei, B. Samali, Collapse capacity of modular steel buildings subject to module loss scenarios: The role of inter-module connections, Eng. Struct. 210 (2020). https://doi.org/10.1016/j.engstruct.2020.110373.

[2] Z. Chen, K. Khan, A. Khan, K. Javed, J. Liu, Exploration of the multidirectional stability and response of prefabricated volumetric modular steel structures, J. Constr. Steel Res. 184 (2021) 106826. https://doi.org/10.1016/j.jcsr.2021.106826.

[3] R.M. Lawson, Building design using modules, Steel Constr. Inst. (2007) 1–16.

[4] Y. Shahtaheri, C. Rausch, J. West, C. Haas, M. Nahangi, Managing risk in modular construction using dimensional and geometric tolerance strategies, Autom. Constr. 83 (2017) 303–315. https://doi.org/10.1016/j.autcon.2017.03.011.

[5] P.F. Court, C.L. Pasquire, G.F. Gibb, D. Bower, Modular Assembly with Postponement to Improve Health, Safety, and Productivity in Construction, Pract. Period. Struct. Des. Constr. 14 (2009) 81–89. https://doi.org/10.1061/(asce)1084-0680(2009)14:2(81).

[6] L. Jaillon, C.S. Poon, Y.H. Chiang, Quantifying the waste reduction potential of using prefabrication in building construction in Hong Kong, Waste Manag. 29 (2009) 309–320. https://doi.org/10.1016/j.wasman.2008.02.015.

[7] J.F. Zhang, J.J. Zhao, D.Y. Yang, E.F. Deng, H. Wang, S.Y. Pang, L.M. Cai, S.C. Gao, Mechanical-property tests on assembled-type light steel modular house, J. Constr. Steel Res. 168 (2020) 105981. https://doi.org/10.1016/j.jcsr.2020.105981.

[8] S. English, B. Brwon, An Introduction to Steel and Concrete Modular Construction, 1st Resid. Build. Des. Constr. Conf. (2013) 326–333.

[9] R.M. Lawson, J. Prewer, P.J. Trebilcock, Modular Construction using Light Steel Framing : An Architect ' s Guide, The Steel Construction Institute, 1999.

[10] S.Y. Zhai, Y.F. Lyu, K. Cao, G.Q. Li, W.Y. Wang, C. Chen, Experimental study on bolted-cover plate corner connections for column-supported modular steel buildings, J. Constr. Steel Res. 189 (2022) 107060. https://doi.org/10.1016/j.jcsr.2021.107060.

[11] Y.F. Lyu, G.Q. Li, K. Cao, S.Y. Zhai, Y.B. Wang, L. Mao, M. ming Ran, Bending behavior of splice connection for corner-supported steel modular buildings, Eng. Struct. 250 (2022) 113460. https://doi.org/10.1016/j.engstruct.2021.113460.

[12] Y.F. Lyu, G.Q. Li, K. Cao, S.Y. Zhai, H. Li, C. Chen, Y.Z. Wang, Behavior of splice connection during transfer of vertical load in full-scale corner-supported modular building, Eng. Struct. 230 (2021) 111698. https://doi.org/10.1016/j.engstruct.2020.111698.

[13] P. Barnes, Off-site fabrication, BIM Princ. Pract. (2019) 109–112. https://doi.org/10.1680/bimpp.63693.109.

[14] K. Khan, Z. Chen, J. Liu, A. Khan, K. Javed, Axial compression behaviours of tubular sectioned C-shape continuous-supported steel walls in MSB, J. Constr. Steel Res. 188 (2022) 107009. https://doi.org/10.1016/j.jcsr.2021.107009.

[15] K. Khan, Z. Chen, J. Liu, A. Khan, Experimental and numerical study on planar multi-column walls behaviours with boundary supports, J. Constr. Steel Res. 186 (2021) 106880. https://doi.org/10.1016/j.jcsr.2021.106880.

[16] K. Khan, Z. Chen, J. Liu, A. Khan, Numerical and parametric analysis on compressive behaviours of continuous-supported wall systems in MSB, Structures. 33 (2021) 4053–4079. https://doi.org/10.1016/j.istruc.2021.07.001.

[17] R.M. Lawson, R.G. Ogden, R. Bergin, Application of Modular Construction in High-Rise Buildings, J. Archit. Eng. 18 (2012) 148–154. https://doi.org/10.1061/(asce)ae.1943-5568.0000057.

[18] A.W. Lacey, W. Chen, H. Hao, K. Bi, Review of bolted inter-module connections in modular steel buildings, J. Build. Eng. 23 (2019) 207–219. https://doi.org/10.1016/j.jobe.2019.01.035.

[19] C.D. Annan, M.A. Youssef, M.H. El Naggar, Seismic overstrength in braced frames of modular steel buildings, J. Earthq. Eng. 13 (2009) 1–21. https://doi.org/10.1080/13632460802212576.

[20] Z. Chen, H. Li, A. Chen, Y. Yu, H. Wang, Research on pretensioned modular frame test and simulations, Eng. Struct. 151 (2017) 774–787. https://doi.org/10.1016/j.engstruct.2017.08.019.

[21] Y. Yu, Z. Chen, A. Chen, Experimental study of a pretensioned connection for modular buildings, Steel Compos. Struct. 31 (2019) 217–232. https://doi.org/10.12989/scs.2019.31.3.217.

[22] C. Kyung-Suk, K. Hyung-Joon, Analytical Models of Beam-Column joints in a Unit Modular Frame (in Korean), J. Comput. Struct. Eng. Inst. Korea. 27 (2014) 663–672. https://doi.org/10.7734/coseik.2014.27.6.663.

[23] M. Lawson, R. Ogden, C. Goodier, Design in Modular Construction, 2014. https://doi.org/10.1201/b16607.

[24] C. Dan-Adrian, K.D. Tsavdaridis, A comprehensive review and classification of inter-module connections for hot-rolled steel modular building systems, J. Build. Eng. 50 (2022) 104006. https://doi.org/10.1016/j.jobe.2022.104006.

[25] A.W. Lacey, W. Chen, H. Hao, Experimental methods for inter-module joints in modular building structures – A state-of-the-art review, J. Build. Eng. 46 (2022) 103792. https://doi.org/10.1016/j.jobe.2021.103792.

[26] E.F. Deng, L. Zong, Y. Ding, Z. Zhang, J.F. Zhang, F.W. Shi, L.M. Cai, S.C. Gao, Seismic performance of mid-to-high rise modular steel construction - A critical review, Thin-Walled Struct. 155 (2020) 106924. https://doi.org/10.1016/j.tws.2020.106924.

[27] H.T. Thai, T. Ngo, B. Uy, A review on modular construction for high-rise buildings, Structures. 28 (2020) 1265–1290. https://doi.org/10.1016/j.istruc.2020.09.070.

[28] Z. Ye, K. Giriunas, H. Sezen, G. Wu, D.C. Feng, State-of-the-art review and investigation of structural stability in multi-story modular buildings, J. Build. Eng. 33 (2021) 101844. https://doi.org/10.1016/j.jobe.2020.101844.

[29] S. Srisangeerthanan, M.J. Hashemi, P. Rajeev, E. Gad, S. Fernando, Review of performance requirements for inter-module connections in multi-story modular buildings, J. Build. Eng. 28 (2020) 101087. https://doi.org/10.1016/j.jobe.2019.101087.

[30] A.W. Lacey, W. Chen, H. Hao, K. Bi, Structural response of modular buildings – An overview, J. Build. Eng. 16 (2018) 45–56. https://doi.org/10.1016/j.jobe.2017.12.008.

[31] Z. Chen, J. Liu, Y. Yu, Experimental study on interior connections in modular steel buildings, Eng. Struct. 147 (2017) 625–638. https://doi.org/10.1016/j.engstruct.2017.06.002.

[32] Z. Chen, J. Liu, Y. Yu, C. Zhou, R. Yan, Experimental study of an innovative modular steel building connection, J. Constr. Steel Res. 139 (2017) 69–82. https://doi.org/10.1016/j.jcsr.2017.09.008.

[33] B. Hajimohammadi, S. Das, H. Ghaednia, J. Dhanapal, Structural performance of registration pin connection in VectorBloc modular construction system, J. Constr. Steel Res. 197 (2022) 107464. https://doi.org/10.1016/j.jcsr.2022.107464.

[34] K. Khan, Z. Chen, J. Liu, J. Yan, Simplified modelling of novel non-welded joints for modular steel buildings, Adv. Steel Constr. (2021).

[35] K. Khan, J.B. Yan, Finite Element Analysis on Seismic Behaviour of Novel Joint in Prefabricated Modular Steel Building, Int. J. Steel Struct. (2020). https://doi.org/10.1007/s13296-020-00320-w.

[36] K. Khan, J.-B. Yan, Numerical studies on seismic behaviour of a prefabricated multi storey modular steel building with new type bolted joints, Adv. Steel Constr. 17(1) (2021) 1–9. https://doi.org/10.18057/IJASC.2021.17.1.1.

[37] J. Bowron, Locating pin assembly for a modular frame, WO2020010463A1, 2020.

[38] S.D. Pang, J.Y.R.L. Liew, Z. Dai, Y. Wang, Prefabricated Prefinished Volumetric Construction Joining Tech-niques Review, Modul. Offsite Constr. Summit Proc. (2016). https://doi.org/10.29173/mocs31.

[39] Z. Dai, T.Y.C. Cheong, S.D. Pang, J.Y.R. Liew, Experimental study of grouted sleeve connections under bending for steel modular buildings, Eng. Struct. 243 (2021) 112614. https://doi.org/10.1016/j.engstruct.2021.112614.

[40] Z. Dai, S.D. Pang, J.R. Liew, Axial load resistance of grouted sleeve connection for modular construction, Thin-Walled Struct. 154 (2020) 106883. https://doi.org/10.1016/j.tws.2020.106883.

[41] G. Zhang, L. Xu, Z. Li, Development and seismic retrofit of an innovative modular steel structure connection using symmetrical self-centering haunch braces, Eng. Struct. 229 (2021) 111671. https://doi.org/10.1016/j.engstruct.2020.111671.

[42] E.F. Deng, J.B. Yan, Y. Ding, L. Zong, Z.X. Li, X.M. Dai, Analytical and numerical studies on

steel columns with novel connections in modular construction, Int. J. Steel Struct. 17 (2017) 1613–1626. https://doi.org/10.1007/s13296-017-1226-5.

[43] R. Ma, J. Xia, H. Chang, B. Xu, L. Zhang, Experimental and numerical investigation of mechanical properties on novel modular connections with superimposed beams, 232 (2021). https://doi.org/10.1016/j.engstruct.2021.111858.

[44] G. Nadeem, N.A. Safiee, N. Abu Bakar, I. Abd Karim, N.A. Mohd Nasir, Finite element analysis of proposed self-locking joint for modular steel structures, Appl. Sci. 11 (2021). https://doi.org/10.3390/app11199277.

[45] H. Chen, C. Ke, C. Chen, G. Li, Study on the shear behavior of inter-module connection with a bolt and shear key fi tting for modular steel buildings, 0 (2022) 1–16. https://doi.org/10.1177/13694332221122547.

[46] R.J. Liew, Z. Dai, Y.S. Chau, Steel Concrete Composite Systems for Modular Construction of High-rise Buildings, (2018). https://doi.org/10.4995/asccs2018.2018.7220.

[47] J.Y.R. Liew, Y.S. Chua, Z. Dai, Steel concrete composite systems for modular construction of high-rise buildings, Structures. 21 (2019) 135–149. https://doi.org/10.1016/j.istruc.2019.02.010.

[48] R. Sanches, O. Mercan, B. Roberts, Experimental investigations of vertical post-tensioned connection for modular steel structures, Eng. Struct. 175 (2018) 776–789. https://doi.org/10.1016/j.engstruct.2018.08.049.

[49] R. Sanches, O. Mercan, Vertical post-tensioned connection for modular steel buildings, (2019) 1–8.

[50] A.W. Lacey, W. Chen, H. Hao, K. Bi, New interlocking inter-module connection for modular steel buildings: Experimental and numerical studies, Eng. Struct. 198 (2019). https://doi.org/10.1016/j.engstruct.2019.109465.

[51] A.W. Lacey, W. Chen, H. Hao, K. Bi, F.J. Tallowin, Shear behaviour of post-tensioned inter-module connection for modular steel buildings, J. Constr. Steel Res. 162 (2019) 105707. https://doi.org/10.1016/j.jcsr.2019.105707.

[52] E.F. Deng, L. Zong, Y. Ding, Z. Zhang, J.F. Zhang, F.W. Shi, L.M. Cai, S.C. Gao, Seismic performance of mid-to-high rise modular steel construction - A critical review, Thin-Walled Struct. 155 (2020) 106924. https://doi.org/10.1016/j.tws.2020.106924.

[53] M. Theofanous, L. Gardner, Testing and numerical modelling of lean duplex stainless steel hollow section columns, Eng. Struct. 31 (2009) 3047–3058. https://doi.org/10.1016/j.engstruct.2009.08.004.

[54] K. Tayyebi, M. Sun, Design of direct-formed square and rectangular hollow section stub columns, J. Constr. Steel Res. 178 (2021) 106499. https://doi.org/10.1016/j.jcsr.2020.106499.

[55] H. Liu, H. Jiang, Y. Hu, T. Chan, K. Chung, Structural behaviour of Q355 and Q460 press-braked rectangular hollow section stub columns, J. Constr. Steel Res. 197 (2022) 107497. https://doi.org/10.1016/j.jcsr.2022.107497.

[56] R. Rahnavard, H.D. Craveiro, L. Laím, R.A. Simões, R. Napolitano, Numerical investigation on the composite action of cold-formed steel built-up battened columns, Thin-Walled Struct. 162 (2021) 107553. https://doi.org/10.1016/j.tws.2021.107553.

[57] Y. Liu, B. Young, Buckling of stainless steel square hollow section compression members, J. Constr. Steel Res. 59 (2003) 165–177. https://doi.org/10.1016/S0143-974X(02)00031-7.

[58] J. Yan, B. Zhang, X. Yu, J. Xie, Thin-Walled Structures Mechanical properties of stainless steel QN1906Mo at sub-zero temperatures : Tests and stress – strain models, Thin-Walled Struct. 179 (2022) 109727. https://doi.org/10.1016/j.tws.2022.109727.

[59] J.B. Yan, Y. Geng, P. Xie, J. Xie, Low-temperature mechanical properties of stainless steel 316L: Tests and constitutive models, Constr. Build. Mater. 343 (2022) 128122. https://doi.org/10.1016/j.conbuildmat.2022.128122.

[60] Y. Huang, J. Chen, Y. He, B. Young, Design of cold-formed stainless steel RHS and SHS beam–columns at elevated temperatures, Thin-Walled Struct. 165 (2021) 107960. https://doi.org/10.1016/j.tws.2021.107960.

[61] B. Li, C. Cheng, Z. Song, X. Cao, Z. Kong, Local buckling behaviour of high strength steel welded box-section columns under axial compression, Thin-Walled Struct. 171 (2022). https://doi.org/10.1016/j.tws.2021.108677.

[62] J. Wang, S. Afshan, N. Schillo, M. Theofanous, M. Feldmann, L. Gardner, Material properties and compressive local buckling response of high strength steel square and rectangular hollow sections, Eng. Struct. 130 (2017) 297–315. https://doi.org/10.1016/j.engstruct.2016.10.023.

[63] L. Huan, Y. Yong, Y. Deng, Study on influence of width-to-thickness ratios on static performance of the thin-wall square steel tube columns to axial loads, Build. Sci. 29 (2013).

[64] L. Guo, S. Zhang, W.J. Kim, G. Ranzi, Behavior of square hollow steel tubes and steel tubes filled with concrete, Thin-Walled Struct. 45 (2007) 961–973. https://doi.org/10.1016/j.tws.2007.07.009.

[65] W.. Key, S.. Hassan, G.. Hancock, Column behavior of cold-formed hollow sections, 1998. 114 (2006) 390–407.

[66] E.F. Deng, J.Y. Lian, Z. Liu, G.C. Zhang, S.B. Wang, D. Bin Cao, Compressive Behavior of a Fully Prefabricated Liftable Connection for Modular Steel Construction, Buildings. 12 (2022). https://doi.org/10.3390/buildings12050649.

[67] Monash University-modular construction codes board, Handbook for the Design of modular structures, Monash University, 2017.

[68] R. Lawson, Light Steel Modular Construction High-rise modular building, London Three storey modular office building Modular residential building Four Sided Modules Form of construction, SCI Steel Knowl. (2016) 1–8. https://www.steel-sci.com/assets/downloads/LSF/ED014 Download.pdf.

[69] GB50017-2017, Standard for design of steel structures (in Chinese), (2017).

[70] Z. Chen, J. Liu, Y. Yu, C. Zhou, R. Yan, Experimental study of an innovative modular steel building connection, J. Constr. Steel Res. 139 (2017) 69–82. https://doi.org/10.1016/j.jcsr.2017.09.008.

[71] C.D. Annan, M.A. Youssef, Analytical Investigation of Semi-Rigid Floor Beams Connection in Modular Steel Structures, (2005) 1–9. https://doi.org/10.13140/2.1.2010.3687.

[72] C.D. Annan, M.A. Youssef, M.H. El Naggar, Seismic vulnerability assessment of modular steel buildings, J. Earthq. Eng. 13 (2009) 1065–1088. https://doi.org/10.1080/13632460902933881.

[73] C.D. Annan, M.A. Youssef, M.H. El-Naggar, Effect of Directly Welded Stringer-To-Beam Connections on the Analysis and Design of Modular Steel Building Floors, Adv. Struct. Eng. 12 (2009) 373–383. https://doi.org/10.1260/136943309788708400.

[74] Z. Chen, J. Wang, J. Liu, K. Khan, Seismic behavior and moment transfer capacity of an innovative self-locking inter-module connection for modular steel building, Eng. Struct. 245 (2021) 112978. https://doi.org/10.1016/j.engstruct.2021.112978.

[75] M.X. Xiong, J.B. Yan, Buckling length determination of concrete filled steel tubular column under axial compression in standard fire test, Mater. Struct. Constr. 49 (2016) 1201–1212. https://doi.org/10.1617/s11527-015-0570-1.

[76] GB/T 228.1-2010, Metallic materials-Tensile testing-Part 1: Method of test at room temperature (in Chinese), (2010).

[77] GBT50344-2019, Technical standards for building structure inspection (in Chinese), (2019).

[78] S.B. Kang, B. Yang, X. Zhou, S.D. Nie, Global buckling behaviour of welded Q460GJ steel box columns under axial compression, J. Constr. Steel Res. 140 (2018) 153–162. https://doi.org/10.1016/j.jcsr.2017.10.013.

[79] S. Kazemzadeh Azad, D. Li, B. Uy, Axial slenderness limits for duplex and lean duplex stainless steel-concrete composite columns, J. Constr. Steel Res. 172 (2020) 106175. https://doi.org/10.1016/j.jcsr.2020.106175.

[80] J.B. Yan, X. Dong, J.S. Zhu, Behaviours of stub steel tubular columns subjected to axial compression at low temperatures, Constr. Build. Mater. 228 (2019). https://doi.org/10.1016/j.conbuildmat.2019.116788.

[81] J.B. Yan, J. Feng, Y.B. Luo, Y. Du, Compression behaviour of stainless-steel stub square tubular columns at cold-region low temperatures, J. Constr. Steel Res. 187 (2021) 106984. https://doi.org/10.1016/j.jcsr.2021.106984.

[82] Y. Du, M. Fu, Z. Chen, J.B. Yan, Z. Zheng, Axial compressive behavior of CFRP confined rectangular CFT columns using high-strength materials: Numerical analysis and carrying capacity model, Structures. 36 (2022) 997–1020. https://doi.org/10.1016/j.istruc.2021.12.061.

[83] ABAQUS (2013), User manual Version 6.13., DS SIMULIA Corp, Provid. RI, USA. (2013) 1–847.

[84] K. Khan, Z. Chen, J. Liu, J. Yan, Simplified modelling of novel non-welded joints for modular steel buildings, Adv. Steel Constr. 17 (2021) 412–424. https://doi.org/10.18057/IJASC.2021.17.4.10.

[85] L. Gardner, N. Saari, F. Wang, Comparative experimental study of hot-rolled and cold-formed rectangular hollow sections, Thin-Walled Struct. 48 (2010) 495–507. https://doi.org/10.1016/j.tws.2010.02.003.

[86] L. Jia, Y. Zhao, H. Liu, Z. Chen, K. Kashan, Flexural performance of weld-strengthened steel beam-square column joints subjected to axial column loading, J. Constr. Steel Res. 199 (2022) 107599. https://doi.org/10.1016/j.jcsr.2022.107599.

[87] I. Arrayago, K.J.R. Rasmussen, Influence of the imperfection direction on the ultimate response of steel frames in advanced analysis, J. Constr. Steel Res. 190 (2022) 107137. https://doi.org/10.1016/j.jcsr.2022.107137.

[88] J.B. Yan, Y. Geng, Y. Luo, B. Zhao, T. Wang, Double skin composite beams at Arctic low temperatures: Numerical and analytical studies, J. Constr. Steel Res. 193 (2022) 107286. https://doi.org/10.1016/j.jcsr.2022.107286.

[89] J.-H. Zhu, B. Young, Cold-Formed-Steel Oval Hollow Sections under Axial Compression, J. Struct. Eng. 137 (2011) 719–727. https://doi.org/10.1061/(asce)st.1943-541x.0000337.

[90] M.A. Dabaon, M.H. El-Boghdadi, M.F. Hassanein, A comparative experimental study between stiffened and unstiffened stainless steel hollow tubular stub columns, Thin-Walled Struct. 47 (2009) 73–81. https://doi.org/10.1016/j.tws.2008.05.008.

[91] EN 1993-1-1, Eurocode 3: Design of steel structures - Part 1-1: General rules and rules for buildings, 2005.

[92] UK steel construction information, Member design - SteelConstruction.info, (n.d.). https://www.steelconstruction.info/Member_design#cite_note-NAtoBSEN1993-1-1-2 (accessed June 11, 2021).

[93] NA to CYS EN 1993-1-1:2005, Eurocode 3: Design of steel structures Part 1-1: General rules and rules for buildings, 2005 (2014).

[94] B. Charbrolin, Technical steel research-Partial safety factors for resistance of steel elements to EC3 and EC4 — Calibration for various steel products and failure criteria, 2002.

[95] Publications Office of the EU, Partial safety factors for resistance of steel elements to EC3 and EC4 - Calibration for various steel products and failure criteria, (n.d.). https://op.europa.eu/en/publication-detail/-/publication/1602ab5d-3994-4464-8c44-664016689b1e (accessed June 19, 2021).

[96] CSA-S16-09, CSA standard-Design of steel structures, 2009.

[97] ANSI/AISC 360-16, AISC360/16 Specification for Structural Steel Buildings-An American National Standard, 2016.

[98] Steel Frame Design Manual AISC 360-10, Computers & Structures, INC. SAP2000-Structural and Earthquake Engineering Software, 2015.

[99] M. Liu, Y. Wang, S. Jia, Research on the mechanical properties of new plate-inner sleeve joint of steel modular frame (in Chinese), Steel Constr. (2018).

[100] F. Shi, Y. Li, Innovative inner sleeve composite bolted connections for modular steel constructions: Experimental and numerical studies, J. Build. Eng. (2022) 105624. https://doi.org/10.1016/j.jobe.2022.105624.